

REYNOLDS STRESSES FROM ADCPs AND MODELLING OF
INTERNAL TIDES

by

STEVEN STRINGER

B.Sc, Memorial University of Newfoundland, 1999

A Dissertation Submitted in Partial Fulfillment of the
Requirements for the Degree of

MASTER OF SCIENCE

in the School of Earth and Ocean Sciences

We accept this dissertation as conforming
to the required standard



Dr. Chris Garrett, Supervisor (School of Earth and Ocean Sciences)



Dr. Richard Dewey, Supervisor (School of Earth and Ocean Sciences)



Dr. Rolf Lueck, Member (School of Earth and Ocean Sciences)



Dr. William Crawford, External Examiner
(Institute of Ocean Sciences)

© Steven Stringer, 2003

University of Victoria

*All rights reserved. This dissertation may not be reproduced in whole or in part by
photocopy or other means, without the permission of the author.*

Supervisor: Dr. Chris Garrett, Dr. Richard Dewey

Abstract

Two separate studies are presented. In the first, Reynolds stresses from both a standard four-beam ADCP (Janus) and a modified four-beam ADCP with one vertical and three oblique beams (Cyclops) are analysed algebraically and observationally. Mathematically, the stresses are expressed in terms of the variances of the beam velocities and other unknown components of the stress tensor. It is noted that a deployment condition with zero tilt significantly improves the stress estimates of both instruments. In the presence of tilt, the Janus ADCP provides better estimates of the Reynolds stress than does the Cyclops using the beam variance technique, though the Cyclops ADCP is able to resolve other quantities which the Janus cannot; namely the turbulent kinetic energy and the anisotropy ratio, both of which require a vertical beam for measurement. Further comparisons are made to the data products which can be resolved from a three-beam and a five-beam ADCP which show that a three-beam system cannot recover Reynolds stresses without significant bias from unknown stress tensor components and that a five-beam system can resolve both Reynolds stresses as well as the turbulent kinetic energy. Data from both four-beam ADCPs were gathered during an August 2000 cruise, where both instruments were deployed in Sansum Narrows, off Vancouver Island. The data support the analytic results, which find that unknown stress tensor components (e.g. $\overline{u'^2}$, $\overline{v'^2}$, etc.) that are not multiplied by a tilt angle significantly contaminate the Reynolds stress estimates.

Next, the generation of internal tides by abrupt topography is considered. The tidal generation at a step is examined numerically and compared to an earlier shelf study. The assumption made in the former work of negligible shelf-side internal waves is confirmed for shallow shelves, but is shown to be increasingly unrealistic with decreasing step height. The energy flux generated by the step is compared with the estimate from linear theory for the energy flux from an arctan function and they are found to be equal for vanishing step heights, but the energy flux from the step increasingly exceeds that based on linear theory as the step height increases. Also, the energy flux generated from a knife-edge ridge is calculated and compared to the linear theory prediction for a “Witch of Agnesi” ridge. For vanishing step heights, the knife-edge ridge produces twice the energy flux of the witch, and the ratio increases with step height. Realistic parameter values which are representative of the Hawaiian Ridge are applied to the knife-edge ridge, resulting in reasonable estimates of

energy flux (20GW) as compared to those made in observational studies (Egbert and Ray 2000), despite the simplicity of the knife-edge model.

Examiners:

[REDACTED]
Dr. Chris Garrett, Supervisor (School of Earth and Ocean Sciences)

[REDACTED]
Dr. Richard Dewey, Supervisor (School of Earth and Ocean Sciences)

[REDACTED]
Dr. Rolf Lueck, Member (School of Earth and Ocean Sciences)

[REDACTED]
Dr. William Crawford, External Examiner
(Institute of Ocean Sciences)

Table of Contents

Abstract	ii
Table of Contents	iv
List of Tables	vi
List of Figures	vii
1 Introduction	1
1.1 ADCPs	1
1.1.1 Principles of operation	2
1.1.2 Reynolds stress	3
1.2 Internal Tides	5
2 ADCPs	8
2.1 Janus	8
2.1.1 Janus: zero pitch and roll	8
2.1.2 Janus: full pitch and roll	10
2.2 Cyclops	18
2.2.1 Cyclops: zero pitch and roll	19
2.2.2 Cyclops: full pitch and roll	20
2.3 Three Beam Doppler	30
2.3.1 Three beam: zero pitch and roll	30
2.3.2 Three beam: full pitch and roll	31
2.4 Five Beam Doppler	33
2.4.1 Five beam: zero pitch and roll	33
2.4.2 Five beam: full pitch and roll	34
2.5 Data Analysis	37
2.5.1 Sansum Narrows	38
2.5.2 Velocity comparison	41
2.5.3 Stress comparison	42

3	Internal Tides	65
3.1	Step Topography	65
3.1.1	Stigebrandt formulation	65
3.1.2	Complete formulation	66
3.1.3	Energy flux	74
3.1.4	Comparison with linear theory	77
3.2	Knife Edge Ridge	81
3.2.1	Energy flux	85
3.2.2	Comparison with linear theory	87
3.2.3	Comparison with modeled energy fluxes for realistic sills	89
4	Discussion	90
	Bibliography	93
A	Coordinate Transformations	96

List of Tables

2.1	ADCP deployment details for Sansum Narrows cruise, August 2000	38
-----	--	----

List of Figures

2.1	Ratio of Janus:Cyclops coefficients for undetermined terms in $\overline{u'w'}$ stress, as a function of the pitch and roll	26
2.2	Ratio of Janus:Cyclops coefficients for undetermined terms in $\overline{v'w'}$ stress, as a function of the pitch and roll	26
2.3	Left: Sansum Narrows chart. Right: Southern end of Sansum Narrows. Dots represent ADCP deployment locations, Cyclops (left) and Janus (right). . .	39
2.4	Janus tilt angles (in degrees): heading (upper), pitch (middle), roll (lower). Red denotes portion of record used for stress calculation.	40
2.5	Cyclops tilt angles (in degrees): heading (upper), pitch (middle), roll (lower). Red denotes portion of record used for stress calculation.	40
2.6	Janus “earth” velocities. Along-channel (upper) and cross-channel (upper-middle) horizontal velocities, w (lower-middle), and “ e ” (lower). All velocities are in m/s	45
2.7	Cyclops “earth” velocities. Along-channel (upper) and cross-channel (upper-middle) horizontal velocities, w (lower-middle), and “ e ” (lower). All velocities are in m/s	45
2.8	u velocity in Reynolds decomposition. u (upper), \bar{u} (middle), u' (lower) . .	46
2.9	Cospectrum of $u'w'$. $f_N = 1/20Hz$	46
2.10	Cospectra of $u'w'$ with different FFT lengths. $f_N = 1/20Hz$	46
2.11	$-\overline{u'w'}$ from Cyclops using the averaged coproducts method with 20 minute averaging.	47
2.12	$-\overline{v'w'}$ from Cyclops using the averaged coproducts method with 20 minute averaging.	48
2.13	$-\overline{u'w'}$ from Janus using equation (2.24). The dotted line is the stress excluding bias terms, while the red, green, and magenta lines are the contributions from the $\overline{u'^2}$, $\overline{w'^2}$, and $\overline{u'v'}$ terms, respectively.	54
2.14	$-\overline{v'w'}$ from Janus using equation (2.25). The dotted line is the stress excluding bias terms, while the red, green, and magenta lines are the contributions from the $\overline{v'^2}$, $\overline{w'^2}$, and $\overline{u'v'}$ terms, respectively.	55

of mean flow, the average of equation (1.3) shows that the fluctuations have zero mean. Furthermore, if the continuity equation is averaged, it can be shown that the turbulent fluctuations are non-divergent, as are the total velocity and hence the mean velocity. Now the separated variables are substituted into equation (1.1) and the result is averaged, leaving only

$$\frac{\partial \bar{u}_i}{\partial t} + \bar{u}_j \frac{\partial \bar{u}_i}{\partial x_j} + \frac{\partial}{\partial x_j} \overline{(u'_i u'_j)} = -\frac{1}{\rho_o} \frac{\partial P}{\partial x_i} + \nu \frac{\partial^2 \bar{u}_i}{\partial x_j \partial x_j} - g \delta_{i3}, \quad (1.4)$$

where the continuity equation has been used to obtain the third term. Using the material derivative and combining the three gradient terms, the equation can be re-written as

$$\frac{D \bar{u}_i}{Dt} = -\frac{1}{\rho_o} \frac{\partial \tau_{ij}}{\partial x_j} - g \delta_{i3}, \quad (1.5)$$

where

$$\tau_{ij} = -P \delta_{ij} + \mu \left(\frac{\partial \bar{u}_i}{\partial x_j} + \frac{\partial \bar{u}_j}{\partial x_i} \right) - \rho_o \overline{u'_i u'_j}. \quad (1.6)$$

The second term in parentheses can be introduced since its derivative is zero with respect to x_j . The term $-\rho_o \overline{u'_i u'_j}$ is an additional stress to the viscous stress (the second term) and is called the Reynolds stress tensor. It has nine Cartesian components which are given by

$$-\rho_o \overline{u'_i u'_j} = \begin{bmatrix} -\rho_o \overline{u'^2} & -\rho_o \overline{u'v'} & -\rho_o \overline{u'w'} \\ -\rho_o \overline{u'v'} & -\rho_o \overline{v'^2} & -\rho_o \overline{v'w'} \\ -\rho_o \overline{u'w'} & -\rho_o \overline{v'w'} & -\rho_o \overline{w'^2}. \end{bmatrix} \quad (1.7)$$

The tensor is symmetric; the diagonal terms are normal stresses and the off-diagonal terms are shear stresses. If the turbulence is isotropic, then the shear stresses vanish and $\overline{u'^2} = \overline{v'^2} = \overline{w'^2}$. Their relationship to the mean flow is evident from equation (1.5); they are the mechanism by which momentum is exchanged between the mean flow and the turbulence. Physically, the shear stresses represent the transfer of momentum by turbulent velocity fluctuations. The vertical Reynolds stresses $-\overline{u'w'}$ and $-\overline{v'w'}$, where ρ_o has been dropped for brevity, are agents which re-distribute horizontal momentum vertically. As such, accurate measurements in the ocean are desired.

One technique used during ADCP studies of turbulent variables is the so-called ‘‘variance’’ technique, where the difference of the variances of opposing beams can be used to resolve Reynolds stresses. The variance technique is used in flows where coproducts such as the Reynolds stress cannot be resolved using the standard assumption of horizontal

2.15	$-\overline{u'w'}$ from Janus using equation (2.34). The dotted line is the stress excluding bias terms, while the red and green lines are the contributions from the $\overline{w'^2}$ and $\overline{u'v'}$ terms, respectively.	56
2.16	$-\overline{v'w'}$ from Janus using equation (2.35). The dotted line is the stress excluding bias terms, while the red and green lines are the contributions from the $\overline{w'^2}$ and $\overline{u'v'}$ terms, respectively.	57
2.17	Along-channel Reynolds stress from Janus	58
2.18	Cross-channel Reynolds stress from Janus	59
2.19	$-\overline{u'w'}$ from Cyclops using equation (2.72). The dotted line is the stress excluding bias terms, while the red, green, magenta, and cyan lines are the contributions from the $\overline{u'^2}$, $\overline{v'^2}$, $\overline{w'^2}$, and $\overline{u'v'}$ terms, respectively.	60
2.20	$-\overline{v'w'}$ from Cyclops using equation (2.73). The dotted line is the stress excluding bias terms, while the red, green, and magenta lines are the contributions from the $\overline{v'^2}$, $\overline{w'^2}$, and $\overline{u'v'}$ terms, respectively.	61
2.21	Along-channel Reynolds stress from Janus and Cyclops. The blue line is the rotated Janus stress using equation (2.34) while the red line is the Cyclops stress using equation (2.72).	62
2.22	Cross-channel Reynolds stress from Janus and Cyclops. The blue line is the rotated Janus stress using equation and (2.35) while the red line is the Cyclops stress using equation (2.73).	63
2.23	Histogram of $ u' $	64
3.1	The Stigebrandt (1980) shelf problem	66
3.2	u at sill on the deep-side (blue), shelf-side (red) and in S80 (black). $\delta = 0.5$	73
3.3	w at sill on the deep-side (blue) and the shelf-side (red). $\delta = 0.5$	73
3.4	Values of a_n (blue), b_n (red) and Stigebrandt's a_n (black).	75
3.5	Upper: Horizontal energy fluxes F_1 (blue) and F_2 (red). Lower: Energy flux ratio of F_2 to F_1	78
3.6	Upper: Horizontal energy flux associated with a_n (blue), b_n (red) and Stigebrandt's a_n (black). Lower: energy flux ratios of F_1 to F_{S80} (blue), F_2 to F_{S80} (red), and $F_1 + F_2$ to F_{S80} (black)	79
3.7	$h(x) = \pi^{-1}h_o \tan^{-1}(x/b)$, where $b = 1, 0.1$, and 10^{-6} , respectively	80
3.8	Ratio of total energy flux from step to energy flux from arctan slope ($\epsilon = 1$)	81
3.9	The knife-edge topographic ridge	82
3.10	Coefficient a_n values for $n = 1$ through 200. $\delta = 0.75$	85
3.11	Total horizontal flow $u = u_o + \sum_{n=1}^{1200} a_n u_o \cos \frac{n\pi z}{H}$, $u_o = 1$ m/s, $\delta = 0.75$	86

3.12	Total vertical flow $w = \sum_{n=1}^{1200} a_n u_o \frac{\omega}{N} \sin \frac{n\pi z}{H}$, $u_o = 1$ m/s, $\delta = 0.75$	86
3.13	Depth-averaged normalized horizontal energy flux.	87
3.14	The “Witch of Agnesi” profile. $b = 2$, $b = 0.5$, and $b = 0.01$ from the outer to inner curves, respectively.	88
3.15	Ratio of energy flux from a knife-edge ridge to that from a “Witch of Agnesi” ridge with $\epsilon = 1$	89
A.1	Janus ADCP configuration (redrawn from Lu and Lueck (1999a))	96
A.2	Cyclops ADCP configuration	99

Acknowledgements

I would first like to thank my family for their love and support throughout my academic career and beyond. I wish to thank my supervisors, Chris Garrett and Richard Dewey, for their assistance, encouragement, and patience during the completion of this thesis. Many thanks to Mike Roth and Lou St. Laurent for endless technical support. Finally, thanks to my graduate peers, including Paul, Dáithí, and so many others for making the other side of the country feel like home.

This thesis was completed in part with financial support from an NSERC PGS A scholarship.

To Jacintha... last one, I promise!?

Chapter 1

Introduction

Describing is key to understanding and predicting the structure of flow patterns in the ocean, which is the goal of many endeavours in physical oceanography. Unfortunately, analytical descriptions of a flow field are often unattainable, so approximations are often used to derive the desired quantities. When making direct observations, certain variables may be difficult to measure. When using a physical or numerical model, some processes may be challenging to parameterize. In each instance, approximations may be useful in obtaining the desired results. Obtaining accurate records of vertical velocity in either open ocean or coastal environments is challenging even under ideal conditions. However, it is essential for the study of many oceanic processes ranging from internal waves to turbulence. In many coastal waters, flows are turbulent and measuring vertical velocity is hampered by spatial inhomogeneities. While currents are more homogeneous in ocean basins which are far from boundaries, the logistics of observational oceanography in such regions are daunting. Technology has aided the pursuit of better measurements of the ocean, and instruments such as the acoustic Doppler current profiler (ADCP) have provided investigators with vertical profiles of all three components of the velocity field. Still, with all the advances in instrumentation, simple physical models with reasonable approximations can often yield equally important insights into the characteristics of a flow field. This thesis will focus on two separate approaches to two different physical problems; the first being the determination of Reynolds stresses in a turbulent tidal channel through direct observation and algebraic approximation, and the second being the investigation of internal tides which have been generated by flow over abrupt topography using simple physical models.

1.1 ADCPs

The advent of ADCPs has provided researchers the ability to effectively measure the profile of the current over many depth ranges, something previously impossible when using a limited number of in-line mechanical current meters. In addition, they have afforded the

advantage of remote sensing to the measurement of mean flow variables without the flow obstructions of previous in-line meters. By making the assumption of spatial homogeneity of the flow over scales comparable to the width of the beam field, the ADCP has been able to reproduce large-scale characteristics of the velocity field. Before proceeding, the operation of the ADCP is reviewed.

1.1.1 Principles of operation

Doppler systems of all configurations operate on the basic premise that acoustic pulses which are partially reflected by particles have their frequencies shifted by an amount which is proportional to the velocity of the particles, a concept known as the Doppler effect. If the particle is moving away from the transducer, the acoustic pulse will be rarefied, or stretched, upon its return to the transducer relative to the original pulse. If the particle, on the other hand, is moving towards the transducer, the returned signal will be compressed relative to the original. A key assumption is that the particles are stationary relative to the water so that the inferred velocity can be attributed to the background current rather than the active motion of the scatterer. It should also be noted that Doppler systems can only measure radial velocities, or the velocities in the direction of the beams. If Cartesian velocities are desired, then a transformation matrix is applied to multiple radial velocities. The number of beams on the instrument, regardless of their configuration, must always be greater than or equal to the number of velocity components that are required; if one wishes to extract Earth-referenced u , v , and w velocities, then the Doppler system in question must be composed of a minimum of three beams.

Doppler transducers act as both transmitters and receivers of acoustic energy. After a pulse of energy, which may consist of a single frequency (known as narrowband) or of a combination of signals with a wider range of frequencies (known as broadband) has been emitted, the transducer begins to listen for reflected sound energy to return as it is scattered by particles at all ranges along the path of the beam. Using the speed of sound in water, the received signal can be subdivided into range “bins” based on the expected total travel time to a specific range and back again. The water velocities at each range bin can be computed in two slightly different ways. The first is to compare the frequency of returned signal to that of the original pulse to determine the Doppler shift, and hence the velocity of the scatterers. This method was used by early ADCPs, and is often termed “incoherent”. It has since been replaced by a technique which involves the emission of a minimum of two closely spaced identical pulses. The second of the returning signals will have a slightly different phase relative to the first received echo because of the slight movement of the scatterers

during the time which passed between the scattering of each pulse. It is the relative phase difference between the two pulses which is proportional to the velocity of the scatterers. Due to the fact that the pulses have to be emitted with the same phase, the technique is said to be “coherent” and such systems are often called “pulse-to-pulse coherent” Dopplers. The theory and signal processing techniques of pulse-to-pulse coherent Doppler systems are reviewed in Lhermitte (1983) and Lhermitte and Serafin (1984). The broadband ADCPs in this study record velocities using the pulse-to-pulse coherent technique (Gordon 1996).

1.1.2 Reynolds stress

In addition to recording variables associated with the mean flow, it would be helpful if the ADCP could measure turbulent processes associated with small scale velocity fluctuations. Turbulent flows contain structure at fine scales which defy not only homogeneity on large scales such as the horizontal beam field, but which also escape many “high-resolution” numerical models. Since the range of scales needed to fully resolve a turbulent flow is large, it is more practical to attempt to relate the small scale turbulent mixing processes to characteristics of the large scale flow. To accomplish this, the so-called “Reynolds decomposition” is applied to the flow variables to separate them into a mean flow and a residual turbulent variation. The method is documented in standard texts (see Kundu 1990) and is reviewed here.

First we consider both the Navier-Stokes equation for an incompressible, non-rotating, viscous fluid under the effect of gravity and the continuity equation,

$$\frac{\partial u_i}{\partial t} + u_j \frac{\partial u_i}{\partial x_j} = -\frac{1}{\rho_o} \frac{\partial p}{\partial x_i} + \nu \frac{\partial^2 u_i}{\partial x_j \partial x_j} - g \delta_{i3} \quad (1.1)$$

$$\frac{\partial u_i}{\partial x_i} = 0. \quad (1.2)$$

The flow variable u_i , which is the i^{th} component of the velocity vector using tensor notation, is now separated into a mean flow and turbulent fluctuation by

$$u_i = \bar{u}_i + u'_i, \quad (1.3)$$

where \bar{u}_i is the mean flow averaged over suitably large spatial and temporal scales (to be determined) and u'_i is the turbulent fluctuation. A similar decomposition is applied to the pressure $p = P + p'$, where the mean of the pressure fluctuation is also zero. By definition

homogeneity. It was first used by Lohrmann et al. (1990), who used a high resolution pulse-to-pulse coherent sonar to measure turbulent velocities and stresses. The technique has also been applied to measurements by a 1.2 MHz narrowband ADCP on the Scotian Shelf (van Haren et al. 1994), a 600 kHz broadband ADCP in Cordova Channel near Vancouver Island (Lu and Lueck 1999b), and a 1.2 MHz broadband ADCP in San Francisco Bay (Stacey et al. 1999a,b) and Menai Strait (Rippeth et al. 2002). In this study, the variance technique will be applied to multiple ADCP beam configurations to attempt to determine an optimal configuration for Reynolds stress observations. Among them are a standard four-beam “Janus” 300 kHz broadband ADCP and also a 300 kHz broadband ADCP with a new transducer configuration where one transducer is aligned vertically along the axis of the instrument and the remaining three are placed around the head with equal azimuthal spacing of 120° , henceforth referred to as the “Cyclops” configuration. In Chapter 2 the analytical differences between beam configurations will be investigated and data collected by two ADCPs deployed in close proximity will be examined.

1.2 *Internal Tides*

The generation of internal waves of tidal frequency, or internal tides, in the deep ocean is strongly influenced by local topography. Barotropic tidal currents, which can be an order of magnitude higher than the local mean flow (St. Laurent and Garrett 2002), flowing over topography will generate baroclinic waves. These radiate internal-tide energy away from the generation site (if they satisfy the criteria for free propagation, which requires both horizontal wavenumber $k < N/U$, where N is the buoyancy frequency and U is the barotropic tidal current speed, and wave frequency $\omega > f$, where f is the Coriolis frequency) or dissipate that energy locally. These waves may propagate both upstream and downstream (the “internal tide” regime) or upstream only (the “lee wave” regime), depending on the barotropic tidal speed being smaller or larger, respectively, than the wave speed (St. Laurent and Garrett 2002). This thesis will address the internal tide regime only.

For simple sinusoidal topography, the energy flux, or the baroclinic-wave energy, which has been extracted from the barotropic tidal current, can be determined analytically (Gill 1982). Unfortunately, most of the seafloor bathymetry does not agree with such a simple approximation but rather has many features which, cumulatively, are better described by a continuous spectrum of wavenumbers. For any topography, a key factor is the “steepness” parameter ϵ , which is the ratio of the topographic slope s to the slope of a radiated beam

of tidal energy α (St. Laurent and Garrett 2002), where

$$\alpha = \frac{k}{m} = \left(\frac{\omega^2 - f^2}{N^2 - \omega^2} \right)^{1/2} \quad (1.8)$$

and k and m are the horizontal and vertical wavenumber of the radiated internal tide (it should be noted that ϵ here is a completely different parameter from the TKE dissipation rate, also denoted as ϵ in a previous section). The parameter ϵ can delineate two distinct groups of topography: a “subcritical” regime where $\epsilon < 1$, and a “supercritical” regime where $\epsilon > 1$. Describing the energy flux of waves generated by general “weak” topography ($\epsilon \ll 1$) in an infinite ocean is possible using a linear model developed by Bell (1975). This model uses the weak topography limit to justify the use of a linearized bottom boundary condition $w(z = 0) = \mathbf{U} \cdot \nabla h$, where U is the amplitude of the barotropic tidal current and $h(\mathbf{x})$ represents the topography. Since the linearization ignores the baroclinic tidal velocity and is evaluated at $z = 0$ rather than at $z = h(\mathbf{x})$, Bell was able to compute the energy flux by integrating the Fourier transform of the bottom topography in wavenumber space and summing over the relevant harmonics of the fundamental tidal-frequency ω (i.e. over all harmonics n_o where n_o is the largest integer less than N/ω). This model was extended to include finite depth effects (Llewellyn Smith and Young 2002) and topographies ranging from weak through to critical ($\epsilon = 1$) (Balmforth et al. 2002). However, these models are not applicable to supercritical topography. One simple example of supercritical topography is a step, since the topographic slope of a step is infinite.

The study of internal tide generation at step topography was first undertaken by Rattray (1960) using a two-layer model, which allowed a mode 1 internal tide to propagate along the density interface. Rattray et al. (1969) extended this model to allow for a continuously stratified ocean. Prinsenber (1971) added a sloping continental shelf, Wilmot (1972) added friction to the original flat shelf configuration, and Prinsenber et al. (1974) combined those effects. Prinsenber and Rattray (1975) introduced a depth-decreasing buoyancy frequency to a finite-slope continental shelf model. More recently Craig (1987) studied the generation problem for supercritical slopes up to $\epsilon \leq 2$. Results from these shelf studies have been verified in field observations (Torgrimson and Hickey 1979, New 1988) and numerical simulations (Lu et al. 2001).

Sjöberg and Stigebrandt (1992), henceforth SS92, proposed a model for computing the barotropic to baroclinic tidal-energy flux in the ocean for any discretized bottom bathymetry based on a step model by Stigebrandt (1980), henceforth S80. S80 developed a model for the generation of internal tides in a linearly stratified fjord where a single step represented

the topography. In this model, internal waves were generated at the step and propagated into the deep ocean but not onto the shelf region. No reason is given for this, though the assumption may be that, for a very shallow shelf, the shelf waves will have negligible energy flux compared to the deep-ocean waves. While the S80 model may be applicable to fjords, where shallow shelves are common features, the application of the model in SS92 is implausible since most discretized bathymetric features in the deep ocean will consist of a series of deep, rather than shallow, steps. Clearly, as the step depth approaches the total water depth the asymmetry is reduced, and the waves on either side should at least be comparable in magnitude. Hence the neglect of shelf-side internal-tides seems invalid for the problem addressed by SS92. Section 3.1 of this thesis examines an unapproximated S80 step model which has been modified to include shelf-side internal-tides and compares the original S80 estimates of wave amplitude and energy flux to those of the waves on both sides of the new model. Section 3.2 analyses the internal tides generated from another supercritical feature, the delta function. The “knife-edge” ridge was first examined by Larsen (1968) and Robinson (1968), although both studies were concerned with the scattering effects of the ridge on propagating internal waves. The energy flux from this simple topography is compared to that as calculated at the Hawaiian Ridge using regional tidal models.

Chapter 2

ADCPs

2.1 Janus

A common beam configuration of acoustic Doppler current profilers (ADCPs) is to place four beams with equal azimuthal spacing pointing at a fixed angle away from the vertical axis of the instrument. This arrangement produces two orthogonal planes each containing two beams, and is sometimes called the Janus configuration. It is pictured in Figure A.1. The three axes of rotation are clearly marked, with the angles of rotation around the z , x , and y axes denoted as ϕ_1 , ϕ_2 , and ϕ_3 , respectively. The heading, ϕ_1 , is positive for a rotation of the positive x axis toward the positive y axis around the z axis. The pitch, ϕ_2 , is positive for a rotation of the positive y axis toward the negative z axis around the x axis. Finally, the roll, ϕ_3 , is positive for a rotation of the positive x axis toward the positive z axis around the y axis. An ADCP reports radial velocities in the direction of each of the four beams. Using the three rotation angles and the known angle between each beam and the vertical axis of the ADCP, denoted as θ , each beam velocity can be resolved into absolute horizontal (u and v) and vertical (w) Cartesian velocities. While the three spatial components of velocity have been the standard output of ADCPs since their inception, solutions for co-products such as the Reynolds stress have been sought using the raw beam velocities rather than their Cartesian velocity by-products. Such expressions have been documented (Lu and Lueck, 1999) and are reviewed here for completeness.

2.1.1 Janus: zero pitch and roll

When the pitch (ϕ_2) and roll (ϕ_3) angles are zero, the central axis of the instrument is aligned with the Cartesian z axis and the representations of the beam velocities in terms of Cartesian components are simplified greatly. In all of the work presented, the heading angle is nominally set to zero. If the horizontal Cartesian velocities u and v are meant to be interpreted as ‘east’ and ‘north’, respectively, then a rotation of ϕ_1 about the z axis will be required.

First, the beam velocities are represented in terms of their constituent Cartesian velocities,

$$b_1 = -u_1 \sin \theta - w_1 \cos \theta \quad (2.1)$$

$$b_2 = u_2 \sin \theta - w_2 \cos \theta \quad (2.2)$$

$$b_3 = -v_3 \sin \theta - w_3 \cos \theta \quad (2.3)$$

$$b_4 = v_4 \sin \theta - w_4 \cos \theta. \quad (2.4)$$

Squaring the beam velocities gives the beam variances. In a turbulent environment, it is inappropriate to assume that the velocity field is spatially homogeneous (i.e. $u_1 = u_2 = u$). Rather, it is often assumed that the field is statistically homogeneous to second order, i.e. $\overline{u_1'^2} = \overline{u_2'^2} = \overline{u'^2}$ (and similarly in v and w). Homogeneity of the second moments is required to calculate second order quantities such as the Reynolds stress. Here, and in the following discussion, “homogeneous” is used to mean spatial uniformity. Isotropy, another term frequently used to describe certain turbulent conditions, implies directional uniformity. The beam variances are written as

$$\overline{b_1'^2} = \overline{u'^2} \sin^2 \theta + \overline{w'^2} \cos^2 \theta + 2\overline{u'w'} \sin \theta \cos \theta \quad (2.5)$$

$$\overline{b_2'^2} = \overline{u'^2} \sin^2 \theta + \overline{w'^2} \cos^2 \theta - 2\overline{u'w'} \sin \theta \cos \theta \quad (2.6)$$

$$\overline{b_3'^2} = \overline{v'^2} \sin^2 \theta + \overline{w'^2} \cos^2 \theta + 2\overline{v'w'} \sin \theta \cos \theta \quad (2.7)$$

$$\overline{b_4'^2} = \overline{v'^2} \sin^2 \theta + \overline{w'^2} \cos^2 \theta - 2\overline{v'w'} \sin \theta \cos \theta. \quad (2.8)$$

The Reynolds stress in each orthogonal plane of the instrument is then proportional to the difference of the variances of the two beams in that plane, or

$$-\overline{u'w'} = \frac{1}{2 \sin 2\theta} \left(\overline{b_2'^2} - \overline{b_1'^2} \right) \quad (2.9)$$

$$-\overline{v'w'} = \frac{1}{2 \sin 2\theta} \left(\overline{b_4'^2} - \overline{b_3'^2} \right). \quad (2.10)$$

Equations (2.9) and (2.10) are exact expressions as the variances of the beam velocities are known.

The Reynolds stresses are found to be a scaled difference of the beam equations. They are dynamically important, as they represent the vertical flux of horizontal momentum.

The beam velocities could also be added to extract further information, yielding

$$\overline{b_1'^2} + \overline{b_2'^2} = 2\overline{u'^2} \sin^2 \theta + 2\overline{w'^2} \cos^2 \theta \quad (2.11)$$

$$\overline{b_3'^2} + \overline{b_4'^2} = 2\overline{v'^2} \sin^2 \theta + 2\overline{w'^2} \cos^2 \theta. \quad (2.12)$$

The quantities derived from equations (2.11) and (2.12) are not particularly useful in a general sense, but with certain approximations they can yield new information. For example, under stratified oceanic conditions where $\overline{w'^2} \ll \overline{u'^2}, \overline{v'^2}$, they can be rearranged to solve for $\overline{u'^2}$ and $\overline{v'^2}$, respectively, and then added to find that the horizontal kinetic energy (HKE) is

$$\overline{u'^2} + \overline{v'^2} = \frac{1}{2 \sin^2 \theta} \left(\overline{b_1'^2} + \overline{b_2'^2} + \overline{b_3'^2} + \overline{b_4'^2} \right). \quad (2.13)$$

Thus from the four beams of the Janus configuration the quantities $-\overline{u'w'}$ and $-\overline{v'w'}$ can be extracted, as can $\overline{u'^2}$ and $\overline{v'^2}$ (and hence the HKE) under specific environmental conditions. In addition to the four beam variances, there are also six other cross-correlation terms which can be formed by averaging the turbulent fluctuations of adjacent or opposite beams (eg. $\overline{b_1'b_2'}$). With these six cross-correlation terms, it is possible to uniquely resolve all six stress tensor components. However, this requires the assumption of spatial homogeneity (necessary to convert $\overline{u'_1 u'_2}$ to the required $\overline{u'^2}$), and as such these terms are not very useful. Next we ask how these results will be affected in the presence of non-zero tilt (pitch and roll).

2.1.2 Janus: full pitch and roll

A similar approach is taken when the instrument experiences non-zero pitch and roll angles. However, in this case the beam velocities are not perfectly aligned with the Cartesian planes, and small cross component terms must be included. The beam velocities in a tilted environment have been derived in Appendix A. The tilted beam velocities are given by

$$b_1 = -u_1 \sin(\theta + \phi_3) + v_1 \sin \phi_2 \cos(\theta + \phi_3) - w_1 \cos \phi_2 \cos(\theta + \phi_3) \quad (2.14)$$

$$b_2 = u_2 \sin(\theta - \phi_3) + v_2 \sin \phi_2 \cos(\theta - \phi_3) - w_2 \cos \phi_2 \cos(\theta - \phi_3) \quad (2.15)$$

$$b_3 = -u_3 \sin \phi_3 \cos \theta - v_3 (\cos \phi_2 \sin \theta - \sin \phi_2 \cos \phi_3 \cos \theta) - w_3 (\cos \phi_2 \cos \phi_3 \cos \theta + \sin \phi_2 \sin \theta) \quad (2.16)$$

$$b_4 = -u_4 \sin \phi_3 \cos \theta + v_4 (\cos \phi_2 \sin \theta + \sin \phi_2 \cos \phi_3 \cos \theta) - w_4 (\cos \phi_2 \cos \phi_3 \cos \theta - \sin \phi_2 \sin \theta). \quad (2.17)$$

The beam velocities are once again squared and then differenced to produce Reynolds stress estimates. When determining the beam variances, statistical homogeneity is again assumed so that the variance of a Cartesian velocity component is considered to be equal in each beam, which gives

$$\begin{aligned}
\overline{b_1'^2} &= \overline{u'^2} \sin^2(\theta + \phi_3) + \overline{v'^2} \sin^2 \phi_2 \cos^2(\theta + \phi_3) + \overline{w'^2} \cos^2 \phi_2 \cos^2(\theta + \phi_3) \\
&\quad + 2\overline{u'w'} \cos \phi_2 \sin(\theta + \phi_3) \cos(\theta + \phi_3) - 2\overline{v'w'} \sin \phi_2 \cos \phi_2 \cos^2(\theta + \phi_3) \\
&\quad - 2\overline{u'v'} \sin \phi_2 \sin(\theta + \phi_3) \cos(\theta + \phi_3)
\end{aligned} \tag{2.18}$$

$$\begin{aligned}
\overline{b_2'^2} &= \overline{u'^2} \sin^2(\theta - \phi_3) + \overline{v'^2} \sin^2 \phi_2 \cos^2(\theta - \phi_3) + \overline{w'^2} \cos^2 \phi_2 \cos^2(\theta - \phi_3) \\
&\quad - 2\overline{u'w'} \cos \phi_2 \sin(\theta - \phi_3) \cos(\theta - \phi_3) - 2\overline{v'w'} \sin \phi_2 \cos \phi_2 \cos^2(\theta - \phi_3) \\
&\quad + 2\overline{u'v'} \sin \phi_2 \sin(\theta - \phi_3) \cos(\theta - \phi_3)
\end{aligned} \tag{2.19}$$

$$\begin{aligned}
\overline{b_3'^2} &= \overline{u'^2} \sin^2 \phi_3 \cos^2 \theta \\
&\quad + \overline{v'^2} (\cos^2 \phi_2 \sin^2 \theta - 2 \sin \phi_2 \cos \phi_2 \cos \phi_3 \sin \theta \cos \theta + \sin^2 \phi_2 \cos^2 \phi_3 \cos^2 \theta) \\
&\quad + \overline{w'^2} (\cos^2 \phi_2 \cos^2 \phi_3 \cos^2 \theta + 2 \sin \phi_2 \cos \phi_2 \cos \phi_3 \sin \theta \cos \theta + \sin^2 \phi_2 \sin^2 \theta) \\
&\quad + 2\overline{u'w'} (\cos \phi_2 \sin \phi_3 \sin \theta \cos \theta + \sin \phi_2 \sin \phi_3 \sin \theta \cos \theta) \\
&\quad + 2\overline{v'w'} (\cos^2 \phi_2 \cos \phi_3 \sin \theta \cos \theta + \sin \phi_2 \cos \phi_2 \sin^2 \theta \\
&\quad \quad - \sin \phi_2 \cos \phi_2 \cos^2 \phi_3 \cos^2 \theta - \sin^2 \phi_2 \cos \phi_3 \sin \theta \cos \theta) \\
&\quad + 2\overline{u'v'} (\cos \phi_2 \sin \phi_3 \sin \theta \cos \theta - \sin \phi_2 \sin \phi_3 \cos \phi_3 \cos^2 \theta)
\end{aligned} \tag{2.20}$$

$$\begin{aligned}
\overline{b_4'^2} &= \overline{u'^2} \sin^2 \phi_3 \cos^2 \theta \\
&\quad + \overline{v'^2} (\cos^2 \phi_2 \sin^2 \theta + 2 \sin \phi_2 \cos \phi_2 \cos \phi_3 \sin \theta \cos \theta + \sin^2 \phi_2 \cos^2 \phi_3 \cos^2 \theta) \\
&\quad + \overline{w'^2} (\cos^2 \phi_2 \cos^2 \phi_3 \cos^2 \theta - 2 \sin \phi_2 \cos \phi_2 \cos \phi_3 \sin \theta \cos \theta + \sin^2 \phi_2 \sin^2 \theta) \\
&\quad + 2\overline{u'w'} (\cos \phi_2 \sin \phi_3 \sin \theta \cos \theta - \sin \phi_2 \sin \phi_3 \sin \theta \cos \theta) \\
&\quad + 2\overline{v'w'} (-\cos^2 \phi_2 \cos \phi_3 \sin \theta \cos \theta + \sin \phi_2 \cos \phi_2 \sin^2 \theta \\
&\quad \quad - \sin \phi_2 \cos \phi_2 \cos^2 \phi_3 \cos^2 \theta + \sin^2 \phi_2 \cos \phi_3 \sin \theta \cos \theta) \\
&\quad + 2\overline{u'v'} (-\cos \phi_2 \sin \phi_3 \sin \theta \cos \theta - \sin \phi_2 \sin \phi_3 \cos \phi_3 \cos^2 \theta).
\end{aligned} \tag{2.21}$$

Equations (2.19) and (2.18) and equations (2.21) and (2.20) can be combined to create two equations containing the two desired unknowns, $-\overline{u'w'}$ and $-\overline{v'w'}$. This new system can be inverted to yield the Reynolds stresses in their unapproximated form as

$$\begin{aligned}
-\overline{u'w'} &= \frac{1}{1 - 2 \cos^2 \phi_2 \cos^2 \phi_3} \left\{ \frac{1}{2 \sin 2\theta} \left[2 \sin \phi_2 \sin \phi_3 \left(\overline{b_4'^2} - \overline{b_3'^2} \right) - \frac{\cos 2\phi_3}{\cos \phi_2} \left(\overline{b_2'^2} - \overline{b_1'^2} \right) \right] \right. \\
&\quad + \frac{\sin 2\phi_3}{2 \cos \phi_2} \left(\overline{w'^2} \cos^2 \phi_2 + \overline{v'^2} \sin^2 \phi_2 - \overline{u'^2} \right) \\
&\quad \left. + \tan \phi_2 \left(1 - 2 \sin^2 \phi_2 \cos^2 \phi_3 \right) \overline{u'v'} \right\} \quad (2.22)
\end{aligned}$$

$$\begin{aligned}
-\overline{v'w'} &= -\frac{1}{1 - 2 \cos^2 \phi_2 \cos^2 \phi_3} \left\{ \frac{1}{2 \sin 2\theta} \left[\frac{\cos 2\phi_3}{\cos \phi_3} \left(\overline{b_4'^2} - \overline{b_3'^2} \right) - \tan \phi_2 \tan \phi_3 \left(\overline{b_2'^2} - \overline{b_1'^2} \right) \right] \right. \\
&\quad + \frac{1}{2} \left[\sin 2\phi_2 \cos \phi_3 \overline{w'^2} - \tan \phi_2 \sin 2\phi_3 \tan \phi_3 \overline{u'^2} \right. \\
&\quad \left. + 2 \tan \phi_2 \left(\sin^2 \phi_2 \sin^2 \phi_3 - \cos^2 \phi_2 \cos 2\phi_3 \right) \overline{v'^2} \right] \\
&\quad \left. + \frac{\tan \phi_3 \cos 2\phi_3}{\cos \phi_2} \overline{u'v'} \right\}. \quad (2.23)
\end{aligned}$$

If the pitch (ϕ_2) and roll (ϕ_3) are small, then we can apply the small angle approximations $\sin \phi \approx \phi$ and $\cos \phi \approx 1$ to the tilt angles, and the stresses can be approximated by

$$-\overline{u'w'} \approx \frac{1}{2 \sin 2\theta} \left(\overline{b_2'^2} - \overline{b_1'^2} \right) + \phi_3 \left(\overline{u'^2} - \overline{w'^2} \right) - \phi_2 \overline{u'v'} \quad (2.24)$$

$$-\overline{v'w'} \approx \frac{1}{2 \sin 2\theta} \left(\overline{b_4'^2} - \overline{b_3'^2} \right) - \phi_2 \left(\overline{v'^2} - \overline{w'^2} \right) + \phi_3 \overline{u'v'}, \quad (2.25)$$

as shown in Lu and Lueck (1999b). The largest of the new terms are likely to be $\phi_3 \overline{u'^2}$ and $\phi_2 \overline{v'^2}$. If neglected, they will introduce a bias to the Reynolds stress estimates.

In Section 2.1.1, four independent pieces of information were produced from the four beam equations, aided by the cancellation of certain terms during the process of adding and subtracting specific beam pairs. In the tilted case, each of the six unknown terms have non-zero coefficients when beam pairs are either added or subtracted, so any rearrangement to solve for a specific variable will depend on the remaining unknowns (see equations (2.22) and (2.23)). We can, however, use an independent rearrangement of the beams to solve for a second pair of unknowns which could then be substituted back into equations (2.22) and (2.23) to reduce the number of unknowns in the Reynolds stress expressions from four to two. $\overline{u'^2}$ and $\overline{v'^2}$ are chosen as they were in Section 2.1.1.

First, equations (2.18) and (2.19) are summed, as are equations (2.20) and (2.21), and the resultant sums are written with terms involving $\overline{u'^2}$ and $\overline{v'^2}$ on the left and all other

terms on the right, giving

$$\begin{aligned}
& \left(\sin^2 \theta \cos^2 \phi_3 + \cos^2 \theta \sin^2 \phi_3 \right) \overline{u'^2} + \sin^2 \phi_2 \left(\cos^2 \theta \cos^2 \phi_3 + \sin^2 \theta \sin^2 \phi_3 \right) \overline{v'^2} \\
&= \frac{1}{2} \left(\overline{b_1'^2} + \overline{b_2'^2} \right) - \cos^2 \phi_2 \left(\cos^2 \theta \cos^2 \phi_3 + \sin^2 \theta \sin^2 \phi_3 \right) \overline{w'^2} \\
&\quad - \cos 2\theta \cos \phi_2 \sin 2\phi_3 \overline{u'w'} + \sin 2\phi_2 \left(\cos^2 \theta \cos^2 \phi_3 + \sin^2 \theta \sin^2 \phi_3 \right) \overline{v'w'} \\
&\quad + \cos 2\theta \sin \phi_2 \sin 2\phi_3 \overline{u'v'} \tag{2.26}
\end{aligned}$$

$$\begin{aligned}
& \sin^2 \phi_3 \cos^2 \theta \overline{u'^2} + \left(\cos^2 \phi_2 \sin^2 \theta + \sin^2 \phi_2 \cos^2 \phi_3 \cos^2 \theta \right) \overline{v'^2} \\
&= \frac{1}{2} \left(\overline{b_3'^2} + \overline{b_4'^2} \right) - \left(\cos^2 \phi_2 \cos^2 \phi_3 \cos^2 \theta + \sin^2 \phi_2 \sin^2 \theta \right) \overline{w'^2} - \cos \phi_2 \sin \phi_3 \sin 2\theta \overline{u'w'} \\
&\quad - \sin 2\phi_2 \left(\sin^2 \theta - \cos^2 \phi_3 \cos^2 \theta \right) \overline{v'w'} + \sin \phi_2 \sin 2\phi_3 \cos^2 \theta \overline{u'v'}. \tag{2.27}
\end{aligned}$$

These equations can be rearranged to solve for $\overline{u'^2}$ and $\overline{v'^2}$, so that

$$\begin{aligned}
\overline{u'^2} &= \frac{1}{\sin^2 \theta \left[S \cos^2 \phi_2 + \sin^2 \phi_2 \cos 2\phi_3 \cos^2 \theta \right]} \left\{ \left(\cos^2 \phi_2 \sin^2 \theta + \sin^2 \phi_2 \cos^2 \phi_3 \cos^2 \theta \right) \right. \\
&\quad \left[\frac{1}{2} \left(\overline{b_1'^2} + \overline{b_2'^2} \right) - C \cos^2 \phi_2 \overline{w'^2} - \cos 2\theta \cos \phi_2 \sin 2\phi_3 \overline{u'w'} + C \sin 2\phi_2 \overline{v'w'} \right. \\
&\quad \left. + \cos 2\theta \sin \phi_2 \sin 2\phi_3 \overline{u'v'} \right] - C \sin^2 \phi_2 \left[\frac{1}{2} \left(\overline{b_3'^2} + \overline{b_4'^2} \right) \right. \\
&\quad \left. - \left(\cos^2 \phi_2 \cos^2 \phi_3 \cos^2 \theta + \sin^2 \phi_2 \sin^2 \theta \right) \overline{w'^2} - \cos \phi_2 \sin \phi_3 \sin 2\theta \overline{u'w'} \right. \\
&\quad \left. \left. - \sin 2\phi_2 \left(\sin^2 \theta - \cos^2 \phi_3 \cos^2 \theta \right) \overline{v'w'} + \sin \phi_2 \sin 2\phi_3 \cos^2 \theta \overline{u'v'} \right] \right\} \tag{2.28}
\end{aligned}$$

$$\begin{aligned}
\overline{v'^2} &= \frac{1}{\sin^2 \theta \left[S \cos^2 \phi_2 + \sin^2 \phi_2 \cos 2\phi_3 \cos^2 \theta \right]} \left\{ S \left[\frac{1}{2} \left(\overline{b_3'^2} + \overline{b_4'^2} \right) \right. \right. \\
&\quad \left. - \left(\cos^2 \phi_2 \cos^2 \phi_3 \cos^2 \theta + \sin^2 \phi_2 \sin^2 \theta \right) \overline{w'^2} - \cos \phi_2 \sin \phi_3 \sin 2\theta \overline{u'w'} \right. \\
&\quad \left. \left. - \sin 2\phi_2 \left(\sin^2 \theta - \cos^2 \phi_3 \cos^2 \theta \right) \overline{v'w'} + \sin \phi_2 \sin 2\phi_3 \cos^2 \theta \overline{u'v'} \right] \right. \\
&\quad \left. - \cos^2 \theta \sin^2 \phi_3 \left[\frac{1}{2} \left(\overline{b_1'^2} + \overline{b_2'^2} \right) - C \cos^2 \phi_2 \overline{w'^2} - \cos 2\theta \cos \phi_2 \sin 2\phi_3 \overline{u'w'} \right. \right. \\
&\quad \left. \left. + C \sin 2\phi_2 \overline{v'w'} + \cos 2\theta \sin \phi_2 \sin 2\phi_3 \overline{u'v'} \right] \right\}, \tag{2.29}
\end{aligned}$$

where

$$S = \sin^2 \theta \cos^2 \phi_3 + \cos^2 \theta \sin^2 \phi_3 \quad (2.30)$$

$$C = \cos^2 \theta \cos^2 \phi_3 + \sin^2 \theta \sin^2 \phi_3. \quad (2.31)$$

In addition, the small angle approximations will be applied and the results will be substituted into equations (2.24) and (2.25), the small angle approximations of the fully tilted Reynolds stresses, giving

$$\overline{u'^2} \approx \frac{1}{\sin^2 \theta} \left\{ \frac{1}{2} (\overline{b_2'^2} + \overline{b_1'^2}) - \cos^2 \theta \overline{w'^2} - 2\phi_3 \cos 2\theta \overline{u'w'} + 2\phi_2 \cos^2 \theta \overline{v'w'} \right\} \quad (2.32)$$

$$\overline{v'^2} \approx \frac{1}{\sin^2 \theta} \left\{ \frac{1}{2} (\overline{b_4'^2} + \overline{b_3'^2}) - \cos^2 \theta \overline{w'^2} - \phi_3 \sin 2\theta \overline{u'w'} + 2\phi_2 \cos 2\theta \overline{v'w'} \right\}. \quad (2.33)$$

These approximated expressions are now inserted into equations (2.24) and (2.25), so that

$$-\overline{u'w'} \approx \frac{1}{2 \sin 2\theta} (\overline{b_2'^2} - \overline{b_1'^2}) + \frac{\phi_3}{\sin^2 \theta} \left[\frac{1}{2} (\overline{b_2'^2} + \overline{b_1'^2}) - \overline{w'^2} \right] - \phi_2 \overline{u'v'} \quad (2.34)$$

$$-\overline{v'w'} \approx \frac{1}{2 \sin 2\theta} (\overline{b_4'^2} - \overline{b_3'^2}) - \frac{\phi_2}{\sin^2 \theta} \left[\frac{1}{2} (\overline{b_4'^2} + \overline{b_3'^2}) - \overline{w'^2} \right] + \phi_3 \overline{u'v'}. \quad (2.35)$$

Using a second rearrangement of the beam variance equations to create independent expressions for the unknowns $\overline{u'^2}$ and $\overline{v'^2}$, the largest unknowns have been eliminated from equations (2.24) and (2.25) and new Reynolds stress expressions have emerged with smaller unknown terms containing only $\overline{w'^2}$ and $\overline{u'v'}$, namely equations (2.34) and (2.35). Furthermore, if the turbulence is horizontally isotropic, as may occur away from boundaries, then $\overline{u'v'} = 0$, so certain flow conditions can reduce the impact of these two unknown terms even further. Equations (2.34) and (2.35) can be arrived at more easily if the small angle approximation is applied to the beam velocities directly.

In practice, if the beam variance method is to be used to calculate the Reynolds stresses, one either has to ignore the two unknown correction terms in equations (2.34) and (2.35) by arguing that they are “small”, or they must be calculated from the turbulent fluctuations of the ADCP “earth” velocities. If they are calculated, spatial homogeneity is implicitly employed as that assumption is made by the ADCP in its co-ordinate transformation from beam to Cartesian velocities. The ADCP takes beam velocities at the locations of the

four beams and converts them to Cartesian velocities located along the central (vertical) axis of the instrument. Without spatial homogeneity, there is no reason to believe that the flow at the location of the beams is the same at the central axis of the ADCP. Since the correction terms are assumed to be at the central axis, but the terms as calculated by the instrument are calculated at the beam locations, it would be good to know if the difference between these locations is significant. To do this, the product $(b_2 - b_1)(b_4 - b_3)$ is expanded. If the zero-tilt beam velocities (equations (2.1) through (2.4)) are considered in the context of spatial homogeneity, it can be seen that $b_2 - b_1$ is proportional to u plus another term involving w . Likewise it is obvious that $b_4 - b_3$ is proportional to v plus a similar term involving w . If spatial homogeneity were not used, the beam differences would be proportional to $u_2 + u_1$ and $v_4 + v_3$, respectively. This is also true for the tilted case, although there are more additional terms. Formally expanding $(b_2 - b_1)(b_4 - b_3)$ for the zero-tilt case, it is found that

$$\begin{aligned}
(b_2 - b_1)(b_4 - b_3) &= [(u_2 + u_1) \sin \theta - (w_2 - w_1) \cos \theta][(v_4 + v_3) \sin \theta - (w_4 - w_3) \cos \theta] \\
&= (u_1 v_4 + u_2 v_3 + u_2 v_4 + u_1 v_3) \sin^2 \theta \\
&\quad + (-u_1 w_4 + u_2 w_3 - u_2 w_4 + u_1 w_3) \sin \theta \cos \theta \\
&\quad + (-v_4 w_1 + v_3 w_2 + v_4 w_2 - v_3 w_1) \sin \theta \cos \theta \\
&\quad + (w_2 w_4 - w_2 w_3 - w_1 w_4 + w_1 w_3) \cos^2 \theta.
\end{aligned} \tag{2.36}$$

Rather than assuming full spatial homogeneity, it will be assumed that only the horizontal velocity gradients are uniform across the beam field. If the horizontal distance from the central axis to the beam locations is denoted by L , it can be written that

$$u_1 = u(0) + L \frac{\partial u}{\partial x} \tag{2.37}$$

$$u_2 = u(0) - L \frac{\partial u}{\partial x} \tag{2.38}$$

$$v_3 = v(0) + L \frac{\partial v}{\partial x} \tag{2.39}$$

$$v_4 = v(0) - L \frac{\partial v}{\partial x}, \tag{2.40}$$

where $u(0)$ and $v(0)$ are the horizontal velocities at the central axis. If these expressions are substituted into the first term of equation (2.36), then

$$\begin{aligned}
(b_2 - b_1)(b_4 - b_3) &= 4u(0)v(0)\sin^2\theta \\
&+ (-u_1w_4 + u_2w_3 - u_2w_4 + u_1w_3)\sin\theta\cos\theta \\
&+ (-v_4w_1 + v_3w_2 + v_4w_2 - v_3w_1)\sin\theta\cos\theta \\
&+ (w_2w_4 - w_2w_3 - w_1w_4 + w_1w_3)\cos^2\theta. \tag{2.41}
\end{aligned}$$

Now it can be seen that the left-hand side of equation (2.41) would resemble uv if spatial homogeneity were used, as is done by the ADCP. The right-hand side, then, is uv at the central axis without using full spatial homogeneity (remember that only uniform gradients were assumed) plus correction terms which look like uw , vw , and ww . While the product u_1w_4 , for instance, is not easily used, it can be said that it is likely to be less than $u(0)w(0)$ when both are averaged, since the former involves a spatial separation between beams 1 and 4. In this way, all the correction terms in equation (2.41) are likely smaller than $u(0)w(0)$, $v(0)w(0)$, and $w(0)^2$, respectively. These will serve as upper bounds for the correction terms. Also, since they are likely to be similar in magnitude to each other, but are being subtracted, the following approximations

$$(u_1w_4 - u_2w_3 + u_2w_4 - u_1w_3)\sin\theta\cos\theta = \epsilon_{uw}uw\sin\theta\cos\theta \tag{2.42}$$

$$(v_4w_1 - v_3w_2 - v_4w_2 + v_3w_1)\sin\theta\cos\theta = \epsilon_{vw}vw\sin\theta\cos\theta \tag{2.43}$$

$$(w_2w_4 - w_2w_3 - w_1w_4 + w_1w_3)\cos^2\theta = \epsilon_{ww}ww\cos^2\theta \tag{2.44}$$

can be made, where ϵ_{uw} , ϵ_{vw} , and ϵ_{ww} are all small ($\ll 1$) coefficients. Finally, equation (2.41) can be averaged in the standard fashion to create Reynolds stress expressions to show that

$$\overline{u'v'}_{ADCP} = \overline{u'v'}_{centre} + \epsilon_{uw}\overline{u'w'}\sin\theta\cos\theta + \epsilon_{vw}\overline{v'w'}\sin\theta\cos\theta + \epsilon_{ww}\overline{w'^2}\cos^2\theta. \tag{2.45}$$

The difference between $\overline{u'v'}$ as calculated by the ADCP (using spatial homogeneity) and $\overline{u'v'}$ at the central axis of the instrument (using only uniform gradients of horizontal velocities) is only small terms involving $\overline{u'w'}$ and $\overline{v'w'}$ (the variables being found in equations (2.34) and (2.35)), and $\overline{w'^2}$, the other correction term already in those equations. The new $\overline{w'^2}$ correction term is smaller than the original since $\epsilon\cos^2\theta < 1/\sin^2\theta$. This is encouraging

since it suggests that the correction terms in equations (2.34) and (2.35) can be calculated using the velocity fluctuations of the ADCP without fear that the instrument's assumption of spatial homogeneity is compromising the integrity of the stress expressions. This will be exploited in Section 2.5.3, where the Reynolds stresses will be computed using the beam variance method, but the correction terms will be calculated using the ADCP estimate of the velocity fluctuations.

The previous assumption of uniform horizontal velocity gradients implies a level of coherence between the beams. To further investigate the need for coherence between beams, consider that the terms constituting $\overline{u'v'}_{ADCP}$ are beam covariances such as $\overline{b'_1 b'_3}$ and $\overline{b'_2 b'_4}$. If all the beams have some coherence (as assumed with uniform horizontal velocity gradients), then the beam covariances will not be zero and will have appreciable signal. If so, then even if $\overline{u'v'}_{ADCP}$ turns out to be zero itself it can be said that equation (2.45) is still true, but that the bias terms must be of the same order as $\overline{u'v'}_{centre}$. However, if the beam covariances making up $\overline{u'v'}_{ADCP}$ all equal zero themselves (ie. if all the beams are completely uncorrelated), then there is no way to confirm whether or not equation (2.45) is true as none of the terms will have any signal. It may be the case in that instance that the motions have smaller lengthscales than the beam field, and are hence undetectable. This confirms that beam coherence is necessary to make the assumption that $\overline{u'v'}$ as measured by the ADCP is a suitable approximation to the true $\overline{u'v'}$ at the centre of the beam field.

2.2 Cyclops

The beam variance technique is not limited to a standard Janus configuration. It can also be applied to an ADCP with a vertical beam. While a vertical beam ADCP does not have pairs of beams in orthogonal planes like the Janus ADCP, the expressions of beam variances may still be combined to produce meaningful estimates of Reynolds stresses and other turbulent variables. Under ideal deployment conditions where the tilt angles are small, a vertical beam will be able to produce a vertical velocity estimate which is superior to that which is derived from the difference of two oblique beams due to the errors associated with subtracting large numbers. If a vertical beam ADCP can produce a better estimate of vertical velocity, can it then produce a better estimate of the vertical Reynolds stresses via the beam variance technique? The case where the tilt angles equal zero is first investigated.

2.2.1 Cyclops: zero pitch and roll

The ‘‘Cyclops’’ ADCP beam configuration consists of four beams; a central vertical beam surrounded by three beams with equal azimuthal spacing (120°) and tilt from the vertical axis ($\theta = 20^\circ$). Figure A.2 shows the beam arrangement. Beam velocities in terms of u , v , and w are

$$b_1 = -w_1 \quad (2.46)$$

$$b_2 = v_2 \sin \theta - w_2 \cos \theta \quad (2.47)$$

$$b_3 = u_3 \sin \theta \sin \frac{\pi}{3} - v_3 \sin \theta \cos \frac{\pi}{3} - w_3 \cos \theta \quad (2.48)$$

$$b_4 = -u_4 \sin \theta \sin \frac{\pi}{3} - v_4 \sin \theta \cos \frac{\pi}{3} - w_4 \cos \theta. \quad (2.49)$$

The variance of each beam, maintaining the assumption of statistical homogeneity, is then found as

$$\overline{b_1'^2} = \overline{w'^2} \quad (2.50)$$

$$\overline{b_2'^2} = \sin^2 \theta \overline{v'^2} + \cos^2 \theta \overline{w'^2} - 2 \sin \theta \cos \theta \overline{v'w'} \quad (2.51)$$

$$\begin{aligned} \overline{b_3'^2} = & \sin^2 \theta \sin^2 \frac{\pi}{3} \overline{u'^2} + \sin^2 \theta \cos^2 \frac{\pi}{3} \overline{v'^2} + \cos^2 \theta \overline{w'^2} - 2 \sin^2 \theta \sin \frac{\pi}{3} \cos \frac{\pi}{3} \overline{u'v'} \\ & - 2 \sin \theta \cos \theta \sin \frac{\pi}{3} \overline{u'w'} + 2 \sin \theta \cos \theta \cos \frac{\pi}{3} \overline{v'w'} \end{aligned} \quad (2.52)$$

$$\begin{aligned} \overline{b_4'^2} = & \sin^2 \theta \sin^2 \frac{\pi}{3} \overline{u'^2} + \sin^2 \theta \cos^2 \frac{\pi}{3} \overline{v'^2} + \cos^2 \theta \overline{w'^2} + 2 \sin^2 \theta \sin \frac{\pi}{3} \cos \frac{\pi}{3} \overline{u'v'} \\ & + 2 \sin \theta \cos \theta \sin \frac{\pi}{3} \overline{u'w'} + 2 \sin \theta \cos \theta \cos \frac{\pi}{3} \overline{v'w'}. \end{aligned} \quad (2.53)$$

Equations (2.50) through (2.53) can be rearranged to give estimates of the vertical Reynolds stresses

$$-\overline{u'w'} = -\frac{1}{2 \sin 2\theta \sin \frac{\pi}{3}} \left(\overline{b_4'^2} - \overline{b_3'^2} \right) + \frac{1}{2} \tan \theta \overline{u'v'} \quad (2.54)$$

$$-\overline{v'w'} = \frac{1}{\sin 2\theta} \left(\overline{b_2'^2} - \cos^2 \theta \overline{b_1'^2} \right) - \frac{1}{2} \tan \theta \overline{v'^2} \quad (2.55)$$

$$0 = \left(\overline{b_4'^2} + \overline{b_3'^2} \right) + \left(\overline{b_2'^2} - 3 \cos^2 \theta \overline{b_1'^2} \right) - \frac{3}{2} \sin^2 \theta \left(\overline{u'^2} + \overline{v'^2} \right). \quad (2.56)$$

Even in the case of zero pitch ($\phi_2 = 0$) and zero roll ($\phi_3 = 0$), the stress estimates are not

exact. That is, they each contain an undetermined term; $\overline{u'v'}$ in the $\overline{u'w'}$ expression, and $\overline{v'^2}$ in the $\overline{v'w'}$ expression, respectively. This is due to the fact that the three azimuthal beams cannot resolve independent velocity components from orthogonal planes as the Janus does. Neglecting these terms will introduce a large bias since they are not multiplied by the small tilt angles. Equation (2.56) reveals the relationship between the undetermined terms, confirming that the expressions of Reynolds stress are not unique. If the turbulence is isotropic, then $\overline{u'v'} = 0$ and $\overline{u'^2} = \overline{v'^2}$, in which case exact stress expressions can be found from rearranging equations (2.54) through (2.56) to find

$$-\overline{u'w'} = -\frac{1}{2 \sin 2\theta \sin \frac{\pi}{3}} \left(\overline{b_4'^2} - \overline{b_3'^2} \right) \quad (2.57)$$

$$-\overline{v'w'} = -\frac{1}{3 \sin 2\theta} \left(\overline{b_4'^2} + \overline{b_3'^2} - 2\overline{b_2'^2} \right). \quad (2.58)$$

So while the Cyclops configuration cannot resolve the Reynolds stress exactly in all turbulent conditions, it is able to find them in horizontally isotropic turbulence, which is likely only at the smallest velocity scales.

Equation (2.56) also gives an expression for the horizontal kinetic energy density and, as such, when combined with equation (2.50), yields exact expressions for the anisotropy ratio, α , and the total turbulent kinetic energy density, $\frac{q^2}{2}$. These two variables cannot be directly measured without a vertical beam (Lu and Lueck, 1999), and are given by

$$\alpha = \frac{\overline{w'^2}}{\overline{u'^2} + \overline{v'^2}} = \frac{3 \sin^2 \theta \overline{b_1'^2}}{2 \left(\overline{b_4'^2} + \overline{b_3'^2} + \overline{b_2'^2} - 3 \cos^2 \theta \overline{b_1'^2} \right)} \quad (2.59)$$

$$\frac{q^2}{2} = \frac{\overline{u'^2} + \overline{v'^2} + \overline{w'^2}}{2} = \frac{\overline{b_4'^2} + \overline{b_3'^2} + \overline{b_2'^2} + 3 \left(\frac{1}{2} \sin^2 \theta - \cos^2 \theta \right) \overline{b_1'^2}}{3 \sin^2 \theta}. \quad (2.60)$$

The four beams have been able to extract four independent pieces of information, namely the two vertical Reynolds stresses, the anisotropy ratio and the TKE density. As noted previously, equation (2.56) is not independent because we cannot get estimates of $\overline{u'^2}$ and $\overline{v'^2}$ independently, even for small $\overline{w'^2}$.

2.2.2 Cyclops: full pitch and roll

Finally, the turbulent parameters are estimated from the Cyclops instrument for the case of non-zero pitch and roll angles. The beam velocities in a tilted environment, which are

derived in Appendix A, are

$$b_1 = -u_1 \sin \phi_3 + v_1 \sin \phi_2 \cos \phi_3 - w_1 \cos \phi_2 \cos \phi_3 \quad (2.61)$$

$$b_2 = -u_2 \sin \phi_3 \cos \theta + v_2 (\cos \phi_2 \sin \theta + \sin \phi_2 \cos \phi_3 \cos \theta) - w_2 (\cos \phi_2 \cos \phi_3 \cos \theta - \sin \phi_2 \sin \theta) \quad (2.62)$$

$$b_3 = u_3 \left(\cos \phi_3 \sin \theta \sin \frac{\pi}{3} - \sin \phi_3 \cos \theta \right) - v_3 \left[\left(\cos \phi_2 \cos \frac{\pi}{3} - \sin \phi_2 \sin \phi_3 \sin \frac{\pi}{3} \right) \sin \theta - \sin \phi_2 \cos \phi_3 \cos \theta \right] - w_3 \left[\left(\sin \phi_2 \cos \frac{\pi}{3} + \cos \phi_2 \sin \phi_3 \sin \frac{\pi}{3} \right) \sin \theta + \cos \phi_2 \cos \phi_3 \cos \theta \right] \quad (2.63)$$

$$b_4 = -u_4 \left(\cos \phi_3 \sin \theta \sin \frac{\pi}{3} + \sin \phi_3 \cos \theta \right) - v_4 \left[\left(\cos \phi_2 \cos \frac{\pi}{3} + \sin \phi_2 \sin \phi_3 \sin \frac{\pi}{3} \right) \sin \theta - \sin \phi_2 \cos \phi_3 \cos \theta \right] - w_4 \left[\left(\sin \phi_2 \cos \frac{\pi}{3} - \cos \phi_2 \sin \phi_3 \sin \frac{\pi}{3} \right) \sin \theta + \cos \phi_2 \cos \phi_3 \cos \theta \right]. \quad (2.64)$$

Equations (2.61) through (2.64) are squared to yield the beam variances which are rearranged to give Reynolds stresses. The beam variances are given by

$$\overline{b_1'^2} = \overline{u'^2} \sin^2 \phi_3 + \overline{v'^2} \sin^2 \phi_2 \cos^2 \phi_3 + \overline{w'^2} \cos^2 \phi_2 \cos^2 \phi_3 - 2\overline{u'v'} \sin \phi_2 \sin \phi_3 \cos \phi_3 + 2\overline{u'w'} \cos \phi_2 \sin \phi_3 \cos \phi_3 - 2\overline{v'w'} \sin \phi_2 \cos \phi_2 \cos^2 \phi_3 \quad (2.65)$$

$$\begin{aligned} \overline{b_2'^2} = & \overline{u'^2} \sin^2 \phi_3 \cos^2 \theta \\ & + \overline{v'^2} (\cos^2 \phi_2 \sin^2 \theta + 2 \sin \phi_2 \cos \phi_2 \cos \phi_3 \sin \theta \cos \theta + \sin^2 \phi_2 \cos^2 \phi_3 \cos^2 \theta) \\ & + \overline{w'^2} (\cos^2 \phi_2 \cos^2 \phi_3 \cos^2 \theta - 2 \sin \phi_2 \cos \phi_2 \cos \phi_3 \sin \theta \cos \theta + \sin^2 \phi_2 \sin^2 \theta) \\ & - 2\overline{u'v'} (\cos \phi_2 \sin \phi_3 \sin \theta \cos \theta + \sin \phi_2 \sin \phi_3 \cos \phi_3 \cos^2 \theta) \\ & + 2\overline{u'w'} (\cos \phi_2 \sin \phi_3 \cos \phi_3 \cos^2 \theta - \sin \phi_2 \sin \phi_3 \sin \theta \cos \theta) \\ & - 2\overline{v'w'} (\cos^2 \phi_2 \cos \phi_3 \sin \theta \cos \theta - \sin \phi_2 \cos \phi_2 \sin^2 \theta \\ & \quad + \sin \phi_2 \cos \phi_2 \cos^2 \phi_3 \cos^2 \theta - \sin^2 \phi_2 \cos \phi_3 \sin \theta \cos \theta) \end{aligned} \quad (2.66)$$

$$\begin{aligned}
\overline{b_3^{\prime 2}} &= \overline{u^{\prime 2}} \left(\cos^2 \phi_3 \sin^2 \theta \sin^2 \frac{\pi}{3} - 2 \sin \phi_3 \cos \phi_3 \sin \theta \cos \theta \sin \frac{\pi}{3} + \sin^2 \phi_3 \cos^2 \theta \right) \\
&+ \overline{v^{\prime 2}} \left[\left(\cos \phi_2 \cos \frac{\pi}{3} - \sin \phi_2 \sin \phi_3 \sin \frac{\pi}{3} \right)^2 \sin^2 \theta + \sin^2 \phi_2 \cos^2 \phi_3 \cos^2 \theta \right. \\
&\quad \left. - 2 \sin \phi_2 \cos \phi_3 \sin \theta \cos \theta \left(\cos \phi_2 \cos \frac{\pi}{3} - \sin \phi_2 \sin \phi_3 \sin \frac{\pi}{3} \right) \right] \\
&+ \overline{w^{\prime 2}} \left[\left(\sin \phi_2 \cos \frac{\pi}{3} + \cos \phi_2 \sin \phi_3 \sin \frac{\pi}{3} \right)^2 \sin^2 \theta + \cos^2 \phi_2 \cos^2 \phi_3 \cos^2 \theta \right. \\
&\quad \left. + 2 \cos \phi_2 \cos \phi_3 \sin \theta \cos \theta \left(\sin \phi_2 \cos \frac{\pi}{3} + \cos \phi_2 \sin \phi_3 \sin \frac{\pi}{3} \right) \right] \\
&- 2\overline{u'v'} \left[\left(\cos \phi_2 \cos \frac{\pi}{3} - \sin \phi_2 \sin \phi_3 \sin \frac{\pi}{3} \right) \cos \phi_3 \sin^2 \theta \sin \frac{\pi}{3} \right. \\
&\quad \left. \sin \phi_2 \cos^2 \phi_3 \sin \theta \cos \theta \sin \frac{\pi}{3} + \sin \phi_2 \sin \phi_3 \cos \phi_3 \cos^2 \theta \right. \\
&\quad \left. - \left(\cos \phi_2 \cos \frac{\pi}{3} - \sin \phi_2 \sin \phi_3 \sin \frac{\pi}{3} \right) \sin \phi_3 \sin \theta \cos \theta \right] \\
&- 2\overline{u'w'} \left[\left(\sin \phi_2 \cos \frac{\pi}{3} + \cos \phi_2 \sin \phi_3 \sin \frac{\pi}{3} \right) \cos \phi_3 \sin^2 \theta \sin \frac{\pi}{3} \right. \\
&\quad \left. + \cos \phi_2 \cos^2 \phi_3 \sin \theta \cos \theta \sin \frac{\pi}{3} - \cos \phi_2 \sin \phi_3 \cos \phi_3 \cos^2 \theta \right. \\
&\quad \left. - \left(\sin \phi_2 \cos \frac{\pi}{3} + \cos \phi_2 \sin \phi_3 \sin \frac{\pi}{3} \right) \sin \phi_3 \sin \theta \cos \theta \right] \\
&+ 2\overline{v'w'} \left[\left(\cos^2 \phi_2 \sin \phi_3 \sin \frac{\pi}{3} \cos \frac{\pi}{3} - \sin \phi_2 \cos \phi_2 \sin^2 \phi_3 \sin^2 \frac{\pi}{3} \right. \right. \\
&\quad \left. \left. + \sin \phi_2 \cos \phi_2 \cos^2 \frac{\pi}{3} - \sin^2 \phi_2 \sin \phi_3 \sin \frac{\pi}{3} \cos \frac{\pi}{3} \right) \sin^2 \theta \right. \\
&\quad \left. + \left(\cos \phi_2 \cos \frac{\pi}{3} - \sin \phi_2 \sin \phi_3 \sin \frac{\pi}{3} \right) \cos \phi_2 \cos \phi_3 \sin \theta \cos \theta \right. \\
&\quad \left. - \left(\sin \phi_2 \cos \frac{\pi}{3} + \cos \phi_2 \sin \phi_3 \sin \frac{\pi}{3} \right) \sin \phi_2 \cos \phi_3 \sin \theta \cos \theta \right. \\
&\quad \left. - \sin \phi_2 \cos \phi_2 \cos^2 \phi_3 \cos^2 \theta \right] \tag{2.67}
\end{aligned}$$

$$\begin{aligned}
\overline{b_4'^2} = & \overline{u'^2} \left(\cos^2 \phi_3 \sin^2 \theta \sin^2 \frac{\pi}{3} + 2 \sin \phi_3 \cos \phi_3 \sin \theta \cos \theta \sin \frac{\pi}{3} + \sin^2 \phi_3 \cos^2 \theta \right) \\
& + \overline{v'^2} \left[\left(\cos \phi_2 \cos \frac{\pi}{3} + \sin \phi_2 \sin \phi_3 \sin \frac{\pi}{3} \right)^2 \sin^2 \theta + \sin^2 \phi_2 \cos^2 \phi_3 \cos^2 \theta \right. \\
& \quad \left. - 2 \sin \phi_2 \cos \phi_3 \sin \theta \cos \theta \left(\cos \phi_2 \cos \frac{\pi}{3} + \sin \phi_2 \sin \phi_3 \sin \frac{\pi}{3} \right) \right] \\
& + \overline{w'^2} \left[\left(\sin \phi_2 \cos \frac{\pi}{3} - \cos \phi_2 \sin \phi_3 \sin \frac{\pi}{3} \right)^2 \sin^2 \theta + \cos^2 \phi_2 \cos^2 \phi_3 \cos^2 \theta \right. \\
& \quad \left. + 2 \cos \phi_2 \cos \phi_3 \sin \theta \cos \theta \left(\sin \phi_2 \cos \frac{\pi}{3} - \cos \phi_2 \sin \phi_3 \sin \frac{\pi}{3} \right) \right] \\
& + 2\overline{u'v'} \left[\left(\cos \phi_2 \cos \frac{\pi}{3} + \sin \phi_2 \sin \phi_3 \sin \frac{\pi}{3} \right) \cos \phi_3 \sin^2 \theta \sin \frac{\pi}{3} \right. \\
& \quad \left. - \sin \phi_2 \cos^2 \phi_3 \sin \theta \cos \theta \sin \frac{\pi}{3} - \sin \phi_2 \sin \phi_3 \cos \phi_3 \cos^2 \theta \right. \\
& \quad \left. + \left(\cos \phi_2 \cos \frac{\pi}{3} + \sin \phi_2 \sin \phi_3 \sin \frac{\pi}{3} \right) \sin \phi_3 \sin \theta \cos \theta \right] \\
& + 2\overline{u'w'} \left[\left(\sin \phi_2 \cos \frac{\pi}{3} - \cos \phi_2 \sin \phi_3 \sin \frac{\pi}{3} \right) \cos \phi_3 \sin^2 \theta \sin \frac{\pi}{3} \right. \\
& \quad \left. + \cos \phi_2 \cos^2 \phi_3 \sin \theta \cos \theta \sin \frac{\pi}{3} + \cos \phi_2 \sin \phi_3 \cos \phi_3 \cos^2 \theta \right. \\
& \quad \left. + \left(\sin \phi_2 \cos \frac{\pi}{3} - \cos \phi_2 \sin \phi_3 \sin \frac{\pi}{3} \right) \sin \phi_3 \sin \theta \cos \theta \right] \\
& + 2\overline{v'w'} \left[\left(-\cos^2 \phi_2 \sin \phi_3 \sin \frac{\pi}{3} \cos \frac{\pi}{3} - \sin \phi_2 \cos \phi_2 \sin^2 \phi_3 \sin^2 \frac{\pi}{3} \right. \right. \\
& \quad \left. \left. + \sin \phi_2 \cos \phi_2 \cos^2 \frac{\pi}{3} + \sin^2 \phi_2 \sin \phi_3 \sin \frac{\pi}{3} \cos \frac{\pi}{3} \right) \sin^2 \theta \right. \\
& \quad \left. + \left(\cos \phi_2 \cos \frac{\pi}{3} + \sin \phi_2 \sin \phi_3 \sin \frac{\pi}{3} \right) \cos \phi_2 \cos \phi_3 \sin \theta \cos \theta \right. \\
& \quad \left. - \left(\sin \phi_2 \cos \frac{\pi}{3} - \cos \phi_2 \sin \phi_3 \sin \frac{\pi}{3} \right) \sin \phi_2 \cos \phi_3 \sin \theta \cos \theta \right. \\
& \quad \left. - \sin \phi_2 \cos \phi_2 \cos^2 \phi_3 \cos^2 \theta \right]. \tag{2.68}
\end{aligned}$$

After subtracting pairs of beam variances, the Reynolds stresses can be found in the manner of Section 2.1.2 to be

$$\begin{aligned}
-\overline{u'w'} &= \frac{\sin \phi_3 (2 \sin 2\phi_2 \cos \phi_3 \cos \theta - \cos 2\phi_2 \sin \theta)}{2 \sin \theta [A]} \left\{ (\overline{b_2^2} - \overline{b_1^2}) + \sin^2 \phi_3 \sin^2 \theta \overline{u'^2} \right. \\
&+ \left[\sin^2 \theta (\sin^2 \phi_2 \cos^2 \phi_3 - \cos^2 \phi_2) - 2 \sin \phi_2 \cos \phi_2 \cos \phi_3 \sin \theta \cos \theta \right] \overline{v'^2} \\
&+ \left[\sin^2 \theta (\cos^2 \phi_2 \cos^2 \phi_3 - \sin^2 \phi_2) + 2 \sin \phi_2 \cos \phi_2 \cos \phi_3 \sin \theta \cos \theta \right] \overline{w'^2} \\
&+ 2 \sin \phi_3 \sin \theta (\sin \phi_2 \cos \theta - \cos \phi_2 \cos \phi_3 \sin \theta) \overline{u'v'} \left. \right\} \\
&+ \frac{\cos 2\phi_2 \cos \phi_3 \cos \theta - \sin \phi_2 \cos \phi_2 \sin \theta (1 + \cos^2 \phi_3)}{2 \sin \theta \sin \frac{\pi}{3} [A]} \left\{ (\overline{b_4^2} - \overline{b_3^2}) \right. \\
&- 4 \sin \phi_3 \cos \phi_3 \sin \theta \cos \theta \sin \frac{\pi}{3} \overline{u'^2} \\
&+ 2 \sin \phi_2 \sin \phi_3 \sin \theta \sin \frac{\pi}{3} (2 \sin \phi_2 \cos \phi_3 \cos \theta - \cos \phi_2 \sin \theta) \overline{v'^2} \\
&+ 2 \cos \phi_2 \sin \phi_3 \sin \theta \sin \frac{\pi}{3} (2 \cos \phi_2 \cos \phi_3 \cos \theta + \sin \phi_2 \sin \theta) \overline{w'^2} \\
&+ 2 \sin \theta \sin \frac{\pi}{3} (2 \sin \phi_2 \cos 2\phi_3 \cos \theta - \cos \phi_2 \cos \phi_3 \sin \theta) \overline{u'v'} \left. \right\} \tag{2.69}
\end{aligned}$$

$$\begin{aligned}
-\overline{v'w'} &= \frac{-2 \cos \phi_2 \cos 2\phi_3 \cos \theta - \sin \phi_2 \cos \phi_3 \sin \theta}{2 \sin \theta [A]} \left\{ (\overline{b_2^2} - \overline{b_1^2}) + \sin^2 \phi_3 \sin^2 \theta \overline{u'^2} \right. \\
&+ \left[\sin^2 \theta (\sin^2 \phi_2 \cos^2 \phi_3 - \cos^2 \phi_2) - 2 \sin \phi_2 \cos \phi_2 \cos \phi_3 \sin \theta \cos \theta \right] \overline{v'^2} \\
&+ \left[\sin^2 \theta (\cos^2 \phi_2 \cos^2 \phi_3 - \sin^2 \phi_2) + 2 \sin \phi_2 \cos \phi_2 \cos \phi_3 \sin \theta \cos \theta \right] \overline{w'^2} \\
&+ 2 \sin \phi_3 \sin \theta (\sin \phi_2 \cos \theta - \cos \phi_2 \cos \phi_3 \sin \theta) \overline{u'v'} \left. \right\} \\
&- \frac{\sin \phi_3 (\cos \phi_2 \cos \phi_3 \sin \theta + \sin \phi_2 \cos \theta)}{2 \sin \theta \sin \frac{\pi}{3} [A]} \left\{ (\overline{b_4^2} - \overline{b_3^2}) - 4 \sin \phi_3 \cos \phi_3 \sin \theta \cos \theta \sin \frac{\pi}{3} \overline{u'^2} \right. \\
&+ 2 \sin \phi_2 \sin \phi_3 \sin \theta \sin \frac{\pi}{3} (2 \sin \phi_2 \cos \phi_3 \cos \theta - \cos \phi_2 \sin \theta) \overline{v'^2} \\
&+ 2 \cos \phi_2 \sin \phi_3 \sin \theta \sin \frac{\pi}{3} (2 \cos \phi_2 \cos \phi_3 \cos \theta + \sin \phi_2 \sin \theta) \overline{w'^2} \\
&+ 2 \sin \theta \sin \frac{\pi}{3} (2 \sin \phi_2 \cos 2\phi_3 \cos \theta - \cos \phi_2 \cos \phi_3 \sin \theta) \overline{u'v'} \left. \right\}, \tag{2.70}
\end{aligned}$$

where the purely geometrical parameter $[A]$ is given by

$$\begin{aligned}
[A] &= \sin^2 \phi_3 (2 \sin 2\phi_2 \cos \phi_3 \cos \theta - \cos 2\phi_2 \sin \theta) (\cos \phi_2 \cos \phi_3 \sin \theta + \sin \phi_2 \cos \theta) \\
&\quad + \sin \phi_2 \cos \phi_2 \sin \theta (2 \cos 2\phi_2 \cos 2\phi_3 \cos \theta + \sin \phi_2 \cos \phi_3 \sin \theta) (1 + \cos^2 \phi_3) \\
&\quad - \cos 2\phi_2 \cos \phi_3 \cos \theta (2 \cos \phi_2 \cos 2\phi_3 \cos \theta + \sin \phi_2 \cos \phi_3 \sin \theta). \tag{2.71}
\end{aligned}$$

Small angle approximations, ($\sin \phi \approx \phi$) and ($\cos \phi \approx 1$), yield

$$\begin{aligned}
-\overline{u'w'} &\approx \frac{1}{\sin 2\theta \sin \frac{\pi}{3} (2 \cos \theta - 3\phi_2 \sin \theta)} \left\{ (2\phi_2 \sin \theta - \cos \theta) (\overline{b_4^2} - \overline{b_3^2}) \right. \\
&\quad + \phi_3 \sin \theta \sin \frac{\pi}{3} (\overline{b_2^2} - \overline{b_1^2}) + 4\phi_3 \sin \theta \cos^2 \theta \sin \frac{\pi}{3} (\overline{u'^2} - \overline{w'^2}) \\
&\quad \left. - \phi_3 \sin^3 \theta \sin \frac{\pi}{3} (\overline{v'^2} - \overline{w'^2}) + 2 \sin \theta \sin \frac{\pi}{3} (\sin \theta \cos \theta - 2\phi_2) \overline{u'v'} \right\} \tag{2.72}
\end{aligned}$$

$$\begin{aligned}
-\overline{v'w'} &\approx \frac{1}{\sin 2\theta \sin \frac{\pi}{3} (2 \cos \theta - 3\phi_2 \sin \theta)} \left\{ (2 \cos \theta + \phi_2 \sin \theta) \sin \frac{\pi}{3} (\overline{b_2^2} - \overline{b_1^2}) \right. \\
&\quad + \phi_3 \sin \theta (\overline{b_4^2} - \overline{b_3^2}) - \sin \theta \sin \frac{\pi}{3} \left[\sin 2\theta + \phi_2 (4 \cos^2 \theta + \sin^2 \theta) \right] (\overline{v'^2} - \overline{w'^2}) \\
&\quad \left. - 2\phi_3 \sin^2 \theta \sin \frac{\pi}{3} (2 \cos \theta + \sin \theta) \overline{u'v'} \right\}. \tag{2.73}
\end{aligned}$$

Each stress expression contains multiple undetermined terms. However, as shown earlier, each expression contains at least one undetermined term which is not multiplied by a tilt angle. This means that each stress estimate contains potentially large undetermined terms which may contribute a large bias to the estimate.

Each Reynolds stress equation ((2.69) and (2.70)) has four known quantities, namely the beam variances, and four unknown quantities, those being $\overline{u'^2}$, $\overline{v'^2}$, $\overline{w'^2}$, and $\overline{u'v'}$, on the right hand side. These same unknowns appear in the Janus stress equations ((2.22) and (2.23)). To determine if the bias associated with a particular unknown term is greater in one instrument or the other, the coefficients attached to each term are examined. Figure 2.1 deals only with the $-\overline{u'w'}$ stress, and shows the ratio of Janus coefficient to Cyclops coefficient for each of the four unknown terms. Figure 2.2 does the same for the $-\overline{v'w'}$ stress.

The figures show that for each stress, the majority of coefficients are larger in the Cyclops

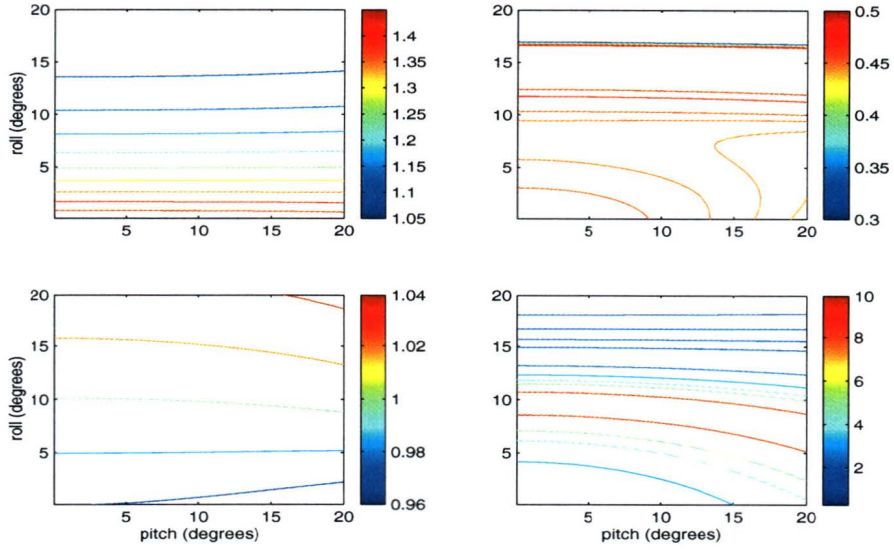


Figure 2.1: Ratio of Janus:Cyclops coefficients for undetermined terms in $\overline{u'w'}$ stress, as a function of the pitch and roll

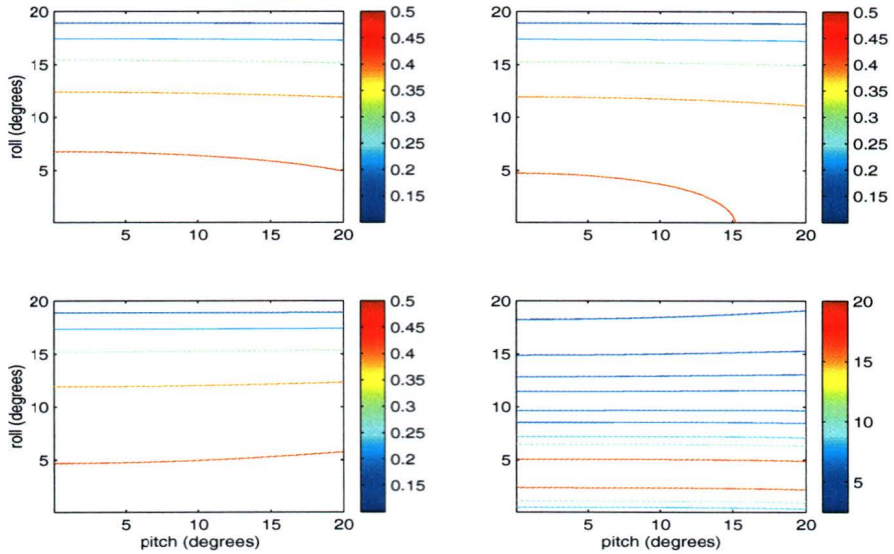


Figure 2.2: Ratio of Janus:Cyclops coefficients for undetermined terms in $\overline{v'w'}$ stress, as a function of the pitch and roll

expressions of Reynolds stress, implying that for the same values of the undetermined terms the Cyclops configuration gives more biased values of the Reynolds stresses. In the $-\overline{u'w'}$ stress, the $\overline{u'^2}$ and $\overline{w'^2}$ terms are each multiplied by ϕ_3 in both instruments and so the order of the ratio of the coefficients is unity. The $\overline{v'^2}$ term is at most a second order in ϕ for the Janus instrument and hence is an order larger in the Cyclops configuration. For the $-\overline{v'w'}$ stress, the $\overline{v'^2}$ and $\overline{w'^2}$ terms are multiplied by ϕ_2 in the Janus configuration and are not in the Cyclops configuration and hence are an order larger in the Cyclops instrument.

Even in specific environmental conditions of horizontal isotropy ($\overline{u'^2} = \overline{v'^2}$ and $\overline{u'v'} = 0$) and where $\overline{w'^2} \ll \overline{u'^2}, \overline{v'^2}$, only one of the undetermined terms not multiplied by a tilt angle is removed, leaving

$$-\overline{u'w'} \approx \frac{1}{\sin 2\theta \sin \frac{\pi}{3} (2 \cos \theta - 3\phi_2 \sin \theta)} \left\{ (2\phi_2 \sin \theta - \cos \theta) (\overline{b_4'^2} - \overline{b_3'^2}) + \phi_3 \sin \theta \sin \frac{\pi}{3} (\overline{b_2'^2} - \overline{b_1'^2}) + \phi_3 \sin \theta \sin \frac{\pi}{3} (4 \cos^2 \theta - \sin^2 \theta) \overline{u'^2} \right\} \quad (2.74)$$

$$-\overline{v'w'} \approx \frac{1}{\sin 2\theta \sin \frac{\pi}{3} (2 \cos \theta - 3\phi_2 \sin \theta)} \left\{ (2 \cos \theta + \phi_2 \sin \theta) \sin \frac{\pi}{3} (\overline{b_2'^2} - \overline{b_1'^2}) + \phi_3 \sin \theta (\overline{b_4'^2} - \overline{b_3'^2}) - \sin \theta \sin \frac{\pi}{3} \left[\sin 2\theta + \phi_2 (4 \cos^2 \theta + \sin^2 \theta) \right] \overline{u'^2} \right\} \quad (2.75)$$

The single undetermined term $\overline{u'^2}$ is multiplied by a tilt angle in equation (2.74), but not in equation (2.75), so even these approximations leave a significant bias term in one of the stress expressions. This is consistent with the Cyclops Reynolds stresses at zero tilt (equations (2.54) and (2.55)), which found that the $\overline{v'w'}$ stress contained a bias which was not multiplied by a tilt angle. Also, this bias cannot be removed as it was for the Janus configuration.

In Section 2.2.1, the turbulent kinetic energy was resolved by assembling a suitable linear combination of beam variances, taking advantage of the fact that the vertical velocity variance was equal to the variance of the central beam. An alternate method for extracting the Cartesian velocity variances is to rewrite the beam variance equations with the velocity variance terms and one or two stress terms (depending on the number of beams in the system) on the left side of the system of equations and the beam variance and remaining stress terms on the right side. For a four beam system, the $\overline{u'v'}$ stress term joins the velocity variances on the left side, while the beam variances and vertical Reynolds stresses are on

the right side. Inverting the four-by-four matrix which has rows consisting of the four sets of coefficients for $\overline{u'^2}$, $\overline{v'^2}$, $\overline{w'^2}$, and $\overline{u'v'}$ yields expressions for each velocity variance in terms of the beam variances and the vertical Reynolds stresses. Re-arranging equations (2.65) through (2.68), and applying the small angle approximation (it can be shown that the same result is obtained whether the approximation is applied before or after the inversion), the matrix equation is written as

$$\begin{bmatrix} A_{\overline{u'^2}}(1) & A_{\overline{v'^2}}(1) & A_{\overline{w'^2}}(1) & A_{\overline{u'v'}}(1) \\ A_{\overline{u'^2}}(2) & A_{\overline{v'^2}}(2) & A_{\overline{w'^2}}(2) & A_{\overline{u'v'}}(2) \\ A_{\overline{u'^2}}(3) & A_{\overline{v'^2}}(3) & A_{\overline{w'^2}}(3) & A_{\overline{u'v'}}(3) \\ A_{\overline{u'^2}}(4) & A_{\overline{v'^2}}(4) & A_{\overline{w'^2}}(4) & A_{\overline{u'v'}}(4) \end{bmatrix} \begin{bmatrix} \overline{u'^2} \\ \overline{v'^2} \\ \overline{w'^2} \\ \overline{u'v'} \end{bmatrix} = \begin{bmatrix} C_{b_1} \\ C_{b_2} \\ C_{b_3} \\ C_{b_4} \end{bmatrix}, \quad (2.76)$$

where

$$\begin{aligned} \begin{bmatrix} A_{\overline{u'^2}}(1) \\ A_{\overline{u'^2}}(2) \\ A_{\overline{u'^2}}(3) \\ A_{\overline{u'^2}}(4) \end{bmatrix} &= \begin{bmatrix} 0 \\ 0 \\ \sin^2 \theta \sin^2 \frac{\pi}{3} - 2 \sin \theta \cos \theta \sin \frac{\pi}{3} \phi_3 \\ \sin^2 \theta \sin^2 \frac{\pi}{3} + 2 \sin \theta \cos \theta \sin \frac{\pi}{3} \phi_3 \end{bmatrix}, \\ \begin{bmatrix} A_{\overline{v'^2}}(1) \\ A_{\overline{v'^2}}(2) \\ A_{\overline{v'^2}}(3) \\ A_{\overline{v'^2}}(4) \end{bmatrix} &= \begin{bmatrix} 0 \\ \sin^2 \theta + 2 \sin \theta \cos \theta \phi_2 \\ \sin^2 \theta \cos^2 \frac{\pi}{3} - 2 \sin \theta \cos \theta \cos \frac{\pi}{3} \phi_2 \\ \sin^2 \theta \cos^2 \frac{\pi}{3} - 2 \sin \theta \cos \theta \cos \frac{\pi}{3} \phi_2 \end{bmatrix}, \\ \begin{bmatrix} A_{\overline{w'^2}}(1) \\ A_{\overline{w'^2}}(2) \\ A_{\overline{w'^2}}(3) \\ A_{\overline{w'^2}}(4) \end{bmatrix} &= \begin{bmatrix} 1 \\ \cos^2 \theta - 2 \sin \theta \cos \theta \phi_2 \\ \cos^2 \theta + \sin \theta \cos \theta (\cos \frac{\pi}{3} \phi_2 + \sin \frac{\pi}{3} \phi_3) \\ \cos^2 \theta + \sin \theta \cos \theta (\cos \frac{\pi}{3} \phi_2 - \sin \frac{\pi}{3} \phi_3) \end{bmatrix}, \\ \begin{bmatrix} A_{\overline{u'v'}}(1) \\ A_{\overline{u'v'}}(2) \\ A_{\overline{u'v'}}(3) \\ A_{\overline{u'v'}}(4) \end{bmatrix} &= \begin{bmatrix} 0 \\ -2 \sin \theta \cos \theta \phi_3 \\ -2(\sin^2 \theta \sin \frac{\pi}{3} \cos \frac{\pi}{3} - \sin \theta \cos \theta \sin \frac{\pi}{3} \phi_3 - \sin \theta \cos \theta \cos \frac{\pi}{3} \phi_3) \\ 2(\sin^2 \theta \sin \frac{\pi}{3} \cos \frac{\pi}{3} - \sin \theta \cos \theta \sin \frac{\pi}{3} \phi_3 - \sin \theta \cos \theta \cos \frac{\pi}{3} \phi_3) \end{bmatrix}, \end{aligned}$$

and

$$\begin{aligned}
C_{b_1} &= \overline{b_1'^2} - 2\phi_3 \overline{u'w'} + 2\phi_2 \overline{v'w'} \\
C_{b_2} &= \overline{b_2'^2} - 2\cos^2\theta \phi_3 \overline{u'w'} + 2(\sin\theta \cos\theta - \sin^2\theta \phi_2 + \cos^2\theta \phi_2) \overline{v'w'} \\
C_{b_3} &= \overline{b_3'^2} + 2[\sin\theta \cos\theta \sin\frac{\pi}{3} - \cos^2\theta \phi_3 + \sin^2\theta \sin\frac{\pi}{3}(\cos\frac{\pi}{3}\phi_2 + \sin\frac{\pi}{3}\phi_3)] \overline{u'w'} \\
&\quad - 2[\sin\theta \cos\theta \cos\frac{\pi}{3} - \cos^2\theta \phi_2 + \sin^2\theta \cos\frac{\pi}{3}(\cos\frac{\pi}{3}\phi_2 + \sin\frac{\pi}{3}\phi_3)] \overline{v'w'} \\
C_{b_4} &= \overline{b_4'^2} - 2[\sin\theta \cos\theta \sin\frac{\pi}{3} + \cos^2\theta \phi_3 + \sin^2\theta \sin\frac{\pi}{3}(\cos\frac{\pi}{3}\phi_2 - \sin\frac{\pi}{3}\phi_3)] \overline{u'w'} \\
&\quad - 2[\sin\theta \cos\theta \cos\frac{\pi}{3} - \cos^2\theta \phi_2 + \sin^2\theta \cos\frac{\pi}{3}(\cos\frac{\pi}{3}\phi_2 - \sin\frac{\pi}{3}\phi_3)] \overline{v'w'}.
\end{aligned}$$

The matrix equation is inverted and terms above first order in pitch and roll are neglected, yielding the following expressions for $\overline{u'^2}$, $\overline{v'^2}$, $\overline{w'^2}$, and $\overline{u'v'}$:

$$\begin{aligned}
\overline{u'^2} &= \frac{1}{\frac{3}{2}\sin^6\theta \sin\frac{\pi}{3}} \left\{ -\frac{1}{2}\sin^4\theta \sin\frac{\pi}{3}(\overline{b_2'^2} + 3\cos^2\theta \overline{b_1'^2}) + \sin^4\theta \sin\frac{\pi}{3}(\overline{b_4'^2} + \overline{b_3'^2}) \right. \\
&\quad + 3\sin^3\theta \cos\theta \sin\frac{\pi}{3}\phi_2(\overline{b_2'^2} - \overline{b_1'^2}) - \frac{3}{2}\sin^3\theta \cos\theta \phi_3(\overline{b_4'^2} - \overline{b_3'^2}) + 3\sin^6\theta \sin\frac{\pi}{3}\overline{u'w'} \\
&\quad \left. + 6\sin^4\theta \cos^2\theta \sin\frac{\pi}{3}(\phi_3 \overline{u'w'} + \phi_2 \overline{v'w'}) - 3\sin^5\theta \cos\theta \sin\frac{\pi}{3}\phi_3 \overline{v'w'} \right\} \quad (2.77)
\end{aligned}$$

$$\begin{aligned}
\overline{v'^2} &= \frac{1}{\frac{3}{2}\sin^6\theta \sin\frac{\pi}{3}} \left\{ \frac{3}{2}\sin^4\theta \sin\frac{\pi}{3}(\overline{b_2'^2} - \cos^2\theta \overline{b_1'^2}) - 3\sin^3\theta \cos\theta \sin\frac{\pi}{3}\phi_2(\overline{b_2'^2} - \overline{b_1'^2}) \right. \\
&\quad + \frac{3}{2}\sin^3\theta \cos\theta \phi_3(\overline{b_4'^2} - \overline{b_3'^2}) - 6\sin^4\theta \cos^2\theta \sin\frac{\pi}{3}(\phi_3 \overline{u'w'} + \phi_2 \overline{v'w'}) \\
&\quad \left. + 3\sin^5\theta \cos\theta \sin\frac{\pi}{3}\overline{v'w'} - 3\sin^6\theta \sin\frac{\pi}{3}\phi_2 \overline{u'w'} \right\} \quad (2.78)
\end{aligned}$$

$$\overline{w'^2} = \frac{1}{\frac{3}{2}\sin^6\theta \sin\frac{\pi}{3}} \left\{ \frac{3}{2}\sin^6\theta \sin\frac{\pi}{3}\overline{b_1'^2} - 3\sin^6\theta \sin\frac{\pi}{3}\phi_3 \overline{u'w'} + 3\sin^6\theta \sin\frac{\pi}{3}\phi_2 \overline{v'w'} \right\} \quad (2.79)$$

$$\begin{aligned}
\overline{u'v'} &= \frac{1}{\frac{3}{2}\sin^6\theta \sin\frac{\pi}{3}} \left\{ 3\sin^3\theta \cos\theta \sin\frac{\pi}{3}\phi_3(3\overline{b_1'^2} + \overline{b_2'^2}) + \frac{3}{4}\sin^3\theta(\sin\theta + 2\cos\theta\phi_2)(\overline{b_4'^2} - \overline{b_3'^2}) \right. \\
&\quad - 2\sin^3\theta \cos\theta \sin\frac{\pi}{3}\phi_3(\overline{b_4'^2} + \overline{b_3'^2}) - 3\sin^5\theta \cos\theta \sin\frac{\pi}{3}\overline{u'w'} \\
&\quad \left. - 3\sin^4\theta \sin\frac{\pi}{3}(2\cos^2\theta + \frac{1}{2}\sin^2\theta)(\phi_2 \overline{u'w'} + \phi_3 \overline{v'w'}) \right\}. \quad (2.80)
\end{aligned}$$

Equation (2.80) reduces to equation (2.54) when the tilt angles are set to zero. With expressions for $\overline{u'^2}$, $\overline{v'^2}$, and $\overline{w'^2}$ in hand, the turbulent kinetic energy and anisotropy ratio are

$$\alpha = \frac{3 \sin^2 \theta \overline{b_1'^2} - 6 \sin^2 \theta (\phi_3 \overline{u'w'} - \phi_2 \overline{v'w'})}{2(\overline{b_4'^2} + \overline{b_3'^2} + \overline{b_2'^2} - 3 \cos^2 \theta \overline{b_1'^2}) + 6 \sin^2 \theta (\phi_3 \overline{u'w'} - \phi_2 \overline{v'w'})} \quad (2.81)$$

$$\frac{q^2}{2} = \frac{1}{3 \sin^2 \theta} \left\{ \overline{b_4'^2} + \overline{b_3'^2} + \overline{b_2'^2} + 3 \left(\frac{1}{2} \sin^2 \theta - \cos^2 \theta \right) \overline{b_1'^2} \right\}. \quad (2.82)$$

The anisotropy ratio reduces to equation (2.59) when the tilt angles are set to zero, but more interesting is the fact that the expression for turbulent kinetic energy for small tilt angles is the same as that with zero tilt; all terms which are first-order in tilt angle exactly cancel each other. This is quite useful since achieving a zero-tilt deployment is difficult, even when the ADCP is mounted in a freely rotating, or gimballed, system. This is a strength of the Cyclops configuration, as energy and anisotropy expressions for Janus configuration have bias terms proportional to ϕ^{-1} which are very large for small tilt.

2.3 Three Beam Doppler

While the four beam (Janus) ADCP gives information beyond the mean current velocities, the use of a three beam Doppler system is being explored as a less expensive alternative to the four beam units. This unit has three slanted beams in the same configuration as those in the Cyclops ADCP. What information has been sacrificed with the reduction to three beams from four?

2.3.1 Three beam: zero pitch and roll

The three beams are arranged the same as the three oblique beams of the Cyclops configuration, and are given in equations (2.47) through (2.49) as

$$b_1 = v_1 \sin \theta - w_1 \cos \theta \quad (2.83)$$

$$b_2 = u_2 \sin \theta \sin \frac{\pi}{3} - v_2 \sin \theta \cos \frac{\pi}{3} - w_2 \cos \theta \quad (2.84)$$

$$b_3 = -u_3 \sin \theta \sin \frac{\pi}{3} - v_3 \sin \theta \cos \frac{\pi}{3} - w_3 \cos \theta. \quad (2.85)$$

This configuration aligns beam b_1 along the y - z plane. The beam variances are computed and then re-arranged to give the Reynolds stresses as

$$-\overline{u'w'} = -\frac{1}{2 \sin 2\theta \sin \frac{\pi}{3}} \left(\overline{b_3'^2} - \overline{b_2'^2} \right) + \frac{1}{2} \tan \theta \overline{u'v'} \quad (2.86)$$

$$-\overline{v'w'} = \frac{1}{\sin 2\theta} \overline{b_1'^2} - \frac{1}{2} \tan \theta \overline{v'^2} - \frac{1}{2} \cot \theta \overline{w'^2}. \quad (2.87)$$

These stress expressions are similar to those for the Cyclops four beam ADCP in that they contain undetermined terms which have coefficients which are large compared to the tilt angles. These terms will provide a significant bias which will contaminate the Reynolds stress estimates. The matrix inversion technique of Section 2.2.2 cannot be employed to determine the kinetic energy because the 3 by 3 coefficient matrix containing the $\overline{u'^2}$, $\overline{v'^2}$, and $\overline{w'^2}$ coefficients is singular and hence cannot be inverted.

2.3.2 Three beam: full pitch and roll

The beam velocities for the three beam system which experiences significant tilting are the same as the three oblique beams of the Cyclops configuration, which are given by equations (2.62) through (2.64) as

$$\begin{aligned} b_1 &= -u_1 \sin \phi_3 \cos \theta + v_1 \left(\cos \phi_2 \sin \theta + \sin \phi_2 \cos \phi_3 \cos \theta \right) \\ &\quad - w_1 \left(\cos \phi_2 \cos \phi_3 \cos \theta - \sin \phi_2 \sin \theta \right) \end{aligned} \quad (2.88)$$

$$\begin{aligned} b_2 &= u_2 \left(\cos \phi_3 \sin \theta \sin \frac{\pi}{3} - \sin \phi_3 \cos \theta \right) \\ &\quad - v_2 \left[\left(\cos \phi_2 \cos \frac{\pi}{3} - \sin \phi_2 \sin \phi_3 \sin \frac{\pi}{3} \right) \sin \theta - \sin \phi_2 \cos \phi_3 \cos \theta \right] \\ &\quad - w_2 \left[\left(\sin \phi_2 \cos \frac{\pi}{3} + \cos \phi_2 \sin \phi_3 \sin \frac{\pi}{3} \right) \sin \theta + \cos \phi_2 \cos \phi_3 \cos \theta \right] \end{aligned} \quad (2.89)$$

$$\begin{aligned} b_3 &= -u_3 \left(\cos \phi_3 \sin \theta \sin \frac{\pi}{3} + \sin \phi_3 \cos \theta \right) \\ &\quad - v_3 \left[\left(\cos \phi_2 \cos \frac{\pi}{3} + \sin \phi_2 \sin \phi_3 \sin \frac{\pi}{3} \right) \sin \theta - \sin \phi_2 \cos \phi_3 \cos \theta \right] \\ &\quad - w_3 \left[\left(\sin \phi_2 \cos \frac{\pi}{3} - \cos \phi_2 \sin \phi_3 \sin \frac{\pi}{3} \right) \sin \theta + \cos \phi_2 \cos \phi_3 \cos \theta \right]. \end{aligned} \quad (2.90)$$

Beam variances are calculated and then Reynolds stresses are extracted from the difference of beams 3 and 2 and from beam 1. This is just one combination of beams that could be used to find the stresses, and it is consistent with the method of section 2.2. The small

angle approximation has been applied for brevity, yielding

$$\begin{aligned}
-\overline{u'w'} &= \frac{1}{[A]} \left\{ \phi_3 \sin^2 \theta \overline{b_1'^2} - \frac{1}{2 \sin \frac{\pi}{3}} (\sin 2\theta + 2\phi_2 \cos 2\theta) (\overline{b_3'^2} - \overline{b_2'^2}) \right. \\
&\quad + \phi_3 \sin^2 2\theta \overline{u'^2} - \phi_3 \sin^4 \theta \overline{v'^2} - \phi_3 (\sin^2 \theta \cos^2 \theta + \sin^2 2\theta) \overline{w'^2} \\
&\quad \left. + \left[\sin^2 \theta \sin 2\theta + \phi_2 (2 \sin^2 \theta \cos 2\theta - \sin^2 2\theta) \right] \overline{u'v'} \right\} \quad (2.91)
\end{aligned}$$

$$\begin{aligned}
-\overline{v'w'} &= \frac{1}{[A]} \left\{ \frac{1}{2} (2\phi_2 \sin^2 \theta - \sin 2\theta) \overline{b_1'^2} - \frac{1}{\sin \frac{\pi}{3}} \phi_3 \cos^2 \theta (\overline{b_3'^2} - \overline{b_2'^2}) \right. \\
&\quad + \frac{1}{2} \left[\sin^2 \theta \sin 2\theta + \phi_2 (\sin^2 2\theta - 2 \sin^4 \theta) \right] \overline{v'^2} \\
&\quad + \frac{1}{2} \left[\sin 2\theta \cos^2 \theta - \phi_2 (2 \sin^2 \theta \cos^2 \theta + \sin^2 2\theta) \right] \overline{w'^2} \\
&\quad \left. + 2\phi_3 \sin^2 \theta \cos^2 \theta \overline{u'v'} \right\}, \quad (2.92)
\end{aligned}$$

where

$$[A] = \sin 2\theta \left[\phi_2 (\sin^2 \theta + 2 \cos 2\theta) + \sin 2\theta \right]. \quad (2.93)$$

While these stress expressions appear to be similar to those for the Cyclops ADCP, given in equations (2.72) and (2.73), they contain additional undetermined terms which are not multiplied by small tilt angles, namely $\overline{u'v'}$ in equation (2.91) and $\overline{v'^2}$ and $\overline{w'^2}$ in equation (2.92). Since there are only three beams, only three independent variables can be solved and hence only one of these terms can be removed, leaving large biases in the stress estimates. Since the three beams can provide three independent variables using the matrix inversion technique of Section 2.2.2, expressions of $\overline{u'^2}$, $\overline{v'^2}$, and $\overline{w'^2}$ can be found and combined to find the kinetic energy in terms of the beam variances and the three stress terms. However, just as in the Janus configuration, the unknown stress terms in the energy expression are of order ϕ^{-1} , meaning that for small tilt angles they create an unacceptably large bias which renders the expression relatively useless.

2.4 Five Beam Doppler

2.4.1 Five beam: zero pitch and roll

Previously a three beam ADCP was studied, which was essentially a Cyclops ADCP without a vertical beam. Now a five beam ADCP will be examined, which is basically a Janus ADCP with an additional vertical beam. The slanted beam velocities for a five beam instrument are the same as those for a Janus instrument, given by equations (2.1) through (2.4), with a vertical beam added as the fifth beam. The beam velocities are

$$b_1 = -u_1 \sin \theta - w_1 \cos \theta \quad (2.94)$$

$$b_2 = u_2 \sin \theta - w_2 \cos \theta \quad (2.95)$$

$$b_3 = -v_3 \sin \theta - w_3 \cos \theta \quad (2.96)$$

$$b_4 = v_4 \sin \theta - w_4 \cos \theta \quad (2.97)$$

$$b_5 = -w_5. \quad (2.98)$$

The first four beams give the same expressions for Reynolds stresses as they do in the Janus configuration,

$$-\overline{u'w'} = \frac{1}{2 \sin 2\theta} (\overline{b_2'^2} - \overline{b_1'^2}) \quad (2.99)$$

$$-\overline{v'w'} = \frac{1}{2 \sin 2\theta} (\overline{b_4'^2} - \overline{b_3'^2}). \quad (2.100)$$

Now the fifth beam allows expressions of the total kinetic energy, $q^2/2$, and the anisotropy ratio, α ,

$$\frac{q^2}{2} = \frac{\overline{u'^2} + \overline{v'^2} + \overline{w'^2}}{2} = \frac{\overline{b_1'^2} + \overline{b_2'^2} + \overline{b_3'^2} + \overline{b_4'^2} - 2(2 \cos^2 \theta - \sin^2 \theta) \overline{b_5'^2}}{4 \sin^2 \theta} \quad (2.101)$$

$$\alpha = \frac{\overline{w'^2}}{\overline{u'^2} + \overline{v'^2}} = \frac{2 \sin^2 \theta \overline{b_5'^2}}{\overline{b_1'^2} + \overline{b_2'^2} + \overline{b_3'^2} + \overline{b_4'^2} - 4 \cos^2 \theta \overline{b_5'^2}}. \quad (2.102)$$

Exact expressions of the Reynolds stresses, TKE, and anisotropy ratio are available because the five beams allow for the solving of five stress components, namely $\overline{u'^2}$, $\overline{v'^2}$, $\overline{w'^2}$, $\overline{u'w'}$, and $\overline{v'w'}$. An independent expression for the sixth component, $\overline{u'v'}$ is unavailable, but

fortunately its effect is exactly cancelled when the TKE and anisotropy ratio are formed.

2.4.2 Five beam: full pitch and roll

The four slanted beam velocities are identical to equations (2.14) through (2.17), while the vertical (fifth) beam is given by equation (2.61), so that

$$b_1 = -u_1 \sin(\theta + \phi_3) + v_1 \sin \phi_2 \cos(\theta + \phi_3) - w_1 \cos \phi_2 \cos(\theta + \phi_3) \quad (2.103)$$

$$b_2 = u_2 \sin(\theta - \phi_3) + v_2 \sin \phi_2 \cos(\theta - \phi_3) - w_2 \cos \phi_2 \cos(\theta - \phi_3) \quad (2.104)$$

$$b_3 = -u_3 \sin \phi_3 \cos \theta - v_3 (\cos \phi_2 \sin \theta - \sin \phi_2 \cos \phi_3 \cos \theta) - w_3 (\cos \phi_2 \cos \phi_3 \cos \theta + \sin \phi_2 \sin \theta) \quad (2.105)$$

$$b_4 = -u_4 \sin \phi_3 \cos \theta + v_4 (\cos \phi_2 \sin \theta + \sin \phi_2 \cos \phi_3 \cos \theta) - w_4 (\cos \phi_2 \cos \phi_3 \cos \theta - \sin \phi_2 \sin \theta) \quad (2.106)$$

$$b_5 = -u_5 \sin \phi_3 + v_5 \sin \phi_2 \cos \phi_3 - w_5 \cos \phi_2 \cos \phi_3. \quad (2.107)$$

The variance technique can yield the same Reynolds stresses found for the Janus configuration, as given by equations (2.22) and (2.23), or

$$\begin{aligned} -\overline{u'w'} = & \frac{1}{1 - 2 \cos^2 \phi_2 \cos^2 \phi_3} \left\{ \frac{1}{2 \sin 2\theta} \left[2 \sin \phi_2 \sin \phi_3 (\overline{b_4'^2} - \overline{b_3'^2}) - \frac{\cos 2\phi_3}{\cos \phi_2} (\overline{b_2'^2} - \overline{b_1'^2}) \right] \right. \\ & + \frac{\sin 2\phi_3}{2 \cos \phi_2} (\overline{w'^2} \cos^2 \phi_2 + \overline{v'^2} \sin^2 \phi_2 - \overline{u'^2}) \\ & \left. + \tan \phi_2 (1 - 2 \sin^2 \phi_2 \cos^2 \phi_3) \overline{u'v'} \right\} \quad (2.108) \end{aligned}$$

$$\begin{aligned} -\overline{v'w'} = & -\frac{1}{1 - 2 \cos^2 \phi_2 \cos^2 \phi_3} \left\{ \frac{1}{2 \sin 2\theta} \left[\frac{\cos 2\phi_3}{\cos \phi_3} (\overline{b_4'^2} - \overline{b_3'^2}) - \tan \phi_2 \tan \phi_3 (\overline{b_2'^2} - \overline{b_1'^2}) \right] \right. \\ & + \frac{1}{2} \left[\sin 2\phi_2 \cos \phi_3 \overline{w'^2} - \tan \phi_2 \sin 2\phi_3 \tan \phi_3 \overline{u'^2} \right. \\ & \left. + 2 \tan \phi_2 (\sin^2 \phi_2 \sin^2 \phi_3 - \cos^2 \phi_2 \cos 2\phi_3) \overline{v'^2} \right] \\ & \left. + \frac{\tan \phi_3 \cos 2\phi_3}{\cos \phi_2} \overline{u'v'} \right\}. \quad (2.109) \end{aligned}$$

These stresses are not unbiased, but the strengths of the biased terms are smaller than in the Cyclops configuration, as shown in Section 2.2.2.

The previous expressions were taken strictly from the four beams in the Janus configuration, but all five beams can be utilized by using the matrix inversion technique to solve for $\overline{u'^2}$, $\overline{v'^2}$, $\overline{w'^2}$, $\overline{u'w'}$, and $\overline{v'w'}$ in terms of the beam variances and $\overline{u'v'}$. After applying the small angle approximation to equations (2.18), (2.19), (2.20), (2.21), and (2.65), the matrix equation can be written as

$$\begin{bmatrix} A_{\overline{u'^2}}(1) & A_{\overline{v'^2}}(1) & A_{\overline{w'^2}}(1) & A_{\overline{u'w'}}(1) & A_{\overline{v'w'}}(1) \\ A_{\overline{u'^2}}(2) & A_{\overline{v'^2}}(2) & A_{\overline{w'^2}}(2) & A_{\overline{u'w'}}(2) & A_{\overline{v'w'}}(2) \\ A_{\overline{u'^2}}(3) & A_{\overline{v'^2}}(3) & A_{\overline{w'^2}}(3) & A_{\overline{u'w'}}(3) & A_{\overline{v'w'}}(3) \\ A_{\overline{u'^2}}(4) & A_{\overline{v'^2}}(4) & A_{\overline{w'^2}}(4) & A_{\overline{u'w'}}(4) & A_{\overline{v'w'}}(4) \\ A_{\overline{u'^2}}(5) & A_{\overline{v'^2}}(5) & A_{\overline{w'^2}}(5) & A_{\overline{u'w'}}(5) & A_{\overline{v'w'}}(5) \end{bmatrix} \begin{bmatrix} \overline{u'^2} \\ \overline{v'^2} \\ \overline{w'^2} \\ \overline{u'w'} \\ \overline{v'w'} \end{bmatrix} = \begin{bmatrix} C_{b_1} \\ C_{b_2} \\ C_{b_3} \\ C_{b_4} \\ C_{b_5} \end{bmatrix}, \quad (2.110)$$

where

$$\begin{aligned} \begin{bmatrix} A_{\overline{u'^2}}(1) \\ A_{\overline{u'^2}}(2) \\ A_{\overline{u'^2}}(3) \\ A_{\overline{u'^2}}(4) \\ A_{\overline{u'^2}}(5) \end{bmatrix} &= \begin{bmatrix} \sin^2 \theta + 2 \sin \theta \cos \theta \phi_3 \\ \sin^2 \theta - 2 \sin \theta \cos \theta \phi_3 \\ 0 \\ 0 \\ 0 \end{bmatrix}, \\ \begin{bmatrix} A_{\overline{v'^2}}(1) \\ A_{\overline{v'^2}}(2) \\ A_{\overline{v'^2}}(3) \\ A_{\overline{v'^2}}(4) \\ A_{\overline{v'^2}}(5) \end{bmatrix} &= \begin{bmatrix} 0 \\ 0 \\ \sin^2 \theta - 2 \sin \theta \cos \theta \phi_3 \\ \sin^2 \theta + 2 \sin \theta \cos \theta \phi_3 \\ 0 \end{bmatrix}, \\ \begin{bmatrix} A_{\overline{w'^2}}(1) \\ A_{\overline{w'^2}}(2) \\ A_{\overline{w'^2}}(3) \\ A_{\overline{w'^2}}(4) \\ A_{\overline{w'^2}}(5) \end{bmatrix} &= \begin{bmatrix} \cos^2 \theta - 2 \sin \theta \cos \theta \phi_3 \\ \cos^2 \theta + 2 \sin \theta \cos \theta \phi_3 \\ \cos^2 \theta + 2 \sin \theta \cos \theta \phi_2 \\ \cos^2 \theta - 2 \sin \theta \cos \theta \phi_2 \\ 1 \end{bmatrix}, \\ \begin{bmatrix} A_{\overline{u'w'}}(1) \\ A_{\overline{u'w'}}(2) \\ A_{\overline{u'w'}}(3) \\ A_{\overline{u'w'}}(4) \\ A_{\overline{u'w'}}(5) \end{bmatrix} &= \begin{bmatrix} 2(\sin \theta \cos \theta + \cos^2 \theta \phi_3 - \sin^2 \theta \phi_3) \\ -2(\sin \theta \cos \theta + \sin^2 \theta \phi_3 - \cos^2 \theta \phi_3) \\ 2 \sin \theta \cos \theta \phi_3 \\ 2 \sin \theta \cos \theta \phi_3 \\ 2 \phi_3 \end{bmatrix} \end{aligned}$$

$$\begin{bmatrix} A_{\overline{v'w'}}(1) \\ A_{\overline{v'w'}}(2) \\ A_{\overline{v'w'}}(3) \\ A_{\overline{v'w'}}(4) \\ A_{\overline{v'w'}}(5) \end{bmatrix} = \begin{bmatrix} -2 \cos^2 \theta \phi_2 \\ -2 \cos^2 \theta \phi_2 \\ 2(\sin \theta \cos \theta + \sin^2 \theta \phi_2 - \cos^2 \theta \phi_2) \\ 2(-\sin \theta \cos \theta + \sin^2 \theta \phi_2 - \cos^2 \theta \phi_2) \\ -2\phi_2 \end{bmatrix},$$

and

$$\begin{aligned} C_{b_1} &= \overline{b_1'^2} + 2 \sin \theta \cos \theta \phi_2 \overline{u'v'} \\ C_{b_2} &= \overline{b_2'^2} - 2 \sin \theta \cos \theta \phi_2 \overline{u'v'} \\ C_{b_3} &= \overline{b_3'^2} - 2 \sin \theta \cos \theta \phi_3 \overline{u'v'} \\ C_{b_4} &= \overline{b_4'^2} + 2 \sin \theta \cos \theta \phi_3 \overline{u'v'} \\ C_{b_5} &= \overline{b_5'^2}. \end{aligned}$$

When equation (2.110) is inverted, the expressions for $\overline{u'^2}$, $\overline{v'^2}$, $\overline{w'^2}$, $\overline{u'w'}$, and $\overline{v'w'}$ are

$$\begin{aligned} \overline{u'^2} &= \frac{-1}{4 \sin^6 \theta \cos^2 \theta} \left\{ -2 \sin^4 \theta \cos^2 \theta (\overline{b_2'^2} + \overline{b_1'^2} - 2 \cos^2 \theta \overline{b_5'^2}) \right. \\ &\quad \left. + 2 \sin^5 \theta \cos \theta \phi_3 (\overline{b_2'^2} - \overline{b_1'^2}) \right\} \end{aligned} \quad (2.111)$$

$$\begin{aligned} \overline{v'^2} &= \frac{-1}{4 \sin^6 \theta \cos^2 \theta} \left\{ -2 \sin^4 \theta \cos^2 \theta (\overline{b_4'^2} + \overline{b_3'^2} - 2 \cos^2 \theta \overline{b_5'^2}) - 2 \sin^4 \theta \cos^2 \theta \phi_3 (\overline{b_2'^2} - \overline{b_1'^2}) \right. \\ &\quad \left. + 2 \sin^3 \theta \cos^3 \theta \phi_3 (\overline{b_2'^2} - \overline{b_1'^2}) - 2 \sin^5 \theta \cos \theta \phi_2 (\overline{b_4'^2} - \overline{b_3'^2}) \right\} \end{aligned} \quad (2.112)$$

$$\begin{aligned} \overline{w'^2} &= \frac{-1}{4 \sin^6 \theta \cos^2 \theta} \left\{ -2 \sin^5 \theta \cos \theta \phi_3 (\overline{b_2'^2} - \overline{b_1'^2}) + 2 \sin^5 \theta \cos \theta \phi_2 (\overline{b_4'^2} - \overline{b_3'^2}) \right. \\ &\quad \left. - 4 \sin^6 \theta \cos^2 \theta \overline{b_5'^2} \right\} \end{aligned} \quad (2.113)$$

$$\begin{aligned} \overline{u'w'} &= \frac{-1}{4 \sin^6 \theta \cos^2 \theta} \left\{ \sin^5 \theta \cos \theta (\overline{b_2'^2} - \overline{b_1'^2}) + 2 \sin^4 \theta \cos^2 \theta \phi_2 (\overline{b_2'^2} + \overline{b_1'^2}) \right. \\ &\quad \left. - 4 \sin^4 \theta \cos^2 \theta \phi_3 \overline{b_5'^2} - 4 \sin^6 \theta \cos^2 \theta \phi_2 \overline{u'v'} \right\} \end{aligned} \quad (2.114)$$

$$\begin{aligned} \overline{v'w'} &= \frac{-1}{4 \sin^6 \theta \cos^2 \theta} \left\{ \sin^5 \theta \cos \theta (\overline{b_4'^2} - \overline{b_3'^2}) - 2 \sin^4 \theta \cos^2 \theta \phi_2 (\overline{b_4'^2} + \overline{b_3'^2}) \right. \\ &\quad \left. + 4 \sin^4 \theta \cos^2 \theta \phi_3 \overline{b_5'^2} + 4 \sin^4 \theta \cos^2 \theta \phi_3 \overline{u'v'} \right\}. \end{aligned} \quad (2.115)$$

Equations (2.111), (2.112), and (2.113) can be combined to give the kinetic energy and

anisotropy ratio

$$\frac{q^2}{2} = \frac{1}{4 \sin^2 \theta} \left\{ (\overline{b_1'^2} + \overline{b_2'^2} + \overline{b_3'^2} + \overline{b_4'^2}) - 2(2 \cos^2 \theta - \sin^2 \theta) \overline{b_5'^2} - (\cot \theta - 1) \phi_3 (\overline{b_2'^2} - \overline{b_1'^2}) \right\} \quad (2.116)$$

$$\alpha = \frac{2 \sin^2 \theta \overline{b_5'^2} + \cot \theta \phi_3 (\overline{b_2'^2} - \overline{b_1'^2}) - \cot \theta \phi_2 (\overline{b_4'^2} - \overline{b_3'^2})}{\overline{b_1'^2} + \overline{b_2'^2} + \overline{b_3'^2} + \overline{b_4'^2} - 4 \cos^2 \theta \overline{b_5'^2} + F(\phi)}, \quad (2.117)$$

where

$$F(\phi) = \cot \theta \phi_2 (\overline{b_4'^2} - \overline{b_3'^2}) + (1 - 2 \csc 2\theta) \phi_3 (\overline{b_2'^2} - \overline{b_1'^2}).$$

Neither expression shows a dependence on the unknown stress $\overline{u'v'}$, hence each can be determined exactly with only small known correction terms due to pitch and roll effects.

Also, equations (2.114) and (2.115), the Reynolds stresses, can be simplified to

$$-\overline{u'w'} = \frac{1}{2 \sin 2\theta} (\overline{b_2'^2} - \overline{b_1'^2}) + \frac{\phi_3}{\sin^2 \theta} \left[\frac{1}{2} (\overline{b_2'^2} + \overline{b_1'^2}) - \overline{b_5'^2} \right] - \phi_2 \overline{u'v'} \quad (2.118)$$

$$-\overline{v'w'} = \frac{1}{2 \sin 2\theta} (\overline{b_4'^2} - \overline{b_3'^2}) - \frac{\phi_2}{\sin^2 \theta} \left[\frac{1}{2} (\overline{b_4'^2} + \overline{b_3'^2}) - \overline{b_5'^2} \right] + \phi_3 \overline{u'v'}. \quad (2.119)$$

These equations are identical to equations (2.34) and (2.35), given that $\overline{\phi w'^2} \approx \phi \overline{b_5'^2}$ when the small angle approximations are applied to equation (2.65) and second order tilt terms are neglected.

On the whole, the five beam system has demonstrated that it is the most versatile of the ADCP configurations considered in this comparison. Not only is it able to resolve the Reynolds stresses without approximation due to the orthogonal beam planes, but the additional vertical beam allows it to calculate the turbulent kinetic energy and anisotropy ratio in both a tilted and non-tilted deployment. These advantages, however, likely come at a direct financial cost of the instrumentation.

2.5 Data Analysis

While it is good to know the theoretical benefits and limitations of each instrument configuration, the greatest test of worth would be a side by side comparison of each instrument

operating within a turbulent flow. The evaluation of the data products from each instrument would ideally allow one to determine which configuration is best suited to record each specific variable. Such a deployment was realized during the summer of 2000, as both a Janus-configured and a Cyclops-configured ADCP were placed in close proximity to each other within a narrow tidal channel.

2.5.1 Sansum Narrows

Sansum Narrows is a twisting channel between the southeastern side of Vancouver Island and the west coast of Saltspring Island, one of the Gulf Islands of British Columbia, and is pictured in Figure 2.3. At the north end it measures nearly 1.5 km wide and 180 m deep. The middle of the Narrows marks its largest dimensions, where it is approximately 1.8 km wide and 250 m deep. The southern section begins at a bottleneck only 500 m wide, and from that point to the southern end the Narrows are quite shallow, measuring only 80 m deep. Tidal currents vary between 1-3 m/s, depending on the lunar phase. It is in this southern region that a Janus-configured and a Cyclops-configured ADCP were deployed for seven days in August 2000 (see Figure 2.3). The deployment details are listed in Table 2.1. Both ADCPs were programmed to generate 10-second ensembles of beam velocities, each containing 16 pings per ensemble.

Configuration	Time of first ping	Time of final ping	number, length of bins
Janus	10:37:29 11/08/2000	18:46:19 18/08/2000	85, 1m
Cyclops	09:08:55 11/08/2000	09:58:05 18/08/2000	80, 1m

Table 2.1: ADCP deployment details for Sansum Narrows cruise, August 2000

While each ADCP recorded velocities for more than seven days, much of the data cannot be used to calculate Reynolds stresses due to unacceptably large fluctuations in tilt angles, despite gimbaled assemblies. Figures 2.4 and 2.5 show the heading, pitch, and roll angles for the Janus and Cyclops ADCPs, respectively, during the complete deployment. After a period of initial adjustment, the pitch and roll angles of both instruments remain relatively stable until August 15th, at which point the Cyclops angles undergo a significant change to an oscillatory state which persists until the end of the deployment. Also, the Janus angles begin a gradual but marked change after the 16th. Thus, data from these periods have

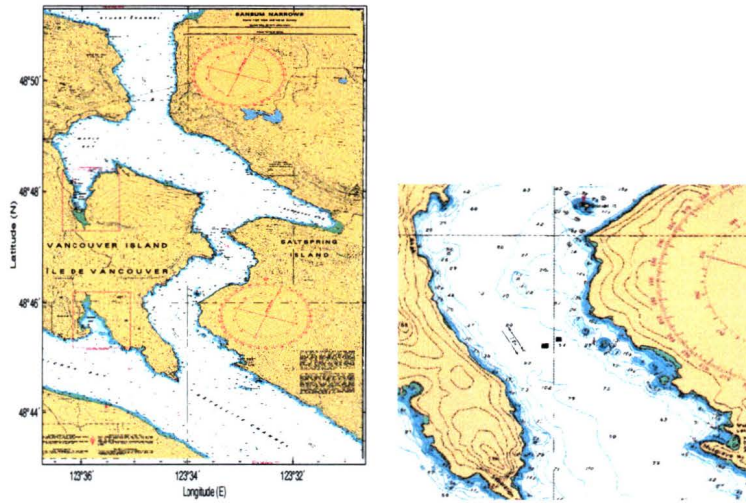


Figure 2.3: Left: Sansum Narrows chart. Right: Southern end of Sansum Narrows. Dots represent ADCP deployment locations, Cyclops (left) and Janus (right).

been discarded for the purpose of calculating Reynolds stresses. The remaining data span a 55-hour window beginning at 10:30:55 on August 12th and ending at 17:47:25 on August 14th, and are indicated in red. The variability of the tilt angles will introduce additional biases to the stress estimates, which will be addressed in Section 2.5.2. The mean values of the relevant sections of pitch and roll are 0.93° and 0.70° , respectively, for the Cyclops ADCP and -7.5° and -3.9° , respectively, for the Janus instrument. While the larger tilts experienced by the Janus instrument are unfortunate, they still fall within the range of the small angle approximation for the purposes of Reynolds stress calculation. Variations in heading were believed to be due to settling and sediment erosion under the trawl-resistant bottom brackets. Before further analysis of the data were made, all velocity estimates were checked for extreme outliers. The velocity records at each depth bin were filtered using an 11-point median filter which eliminated the large majority of the offending data. Those few remaining points which escaped the filter were manually flagged and replaced with interpolated data.

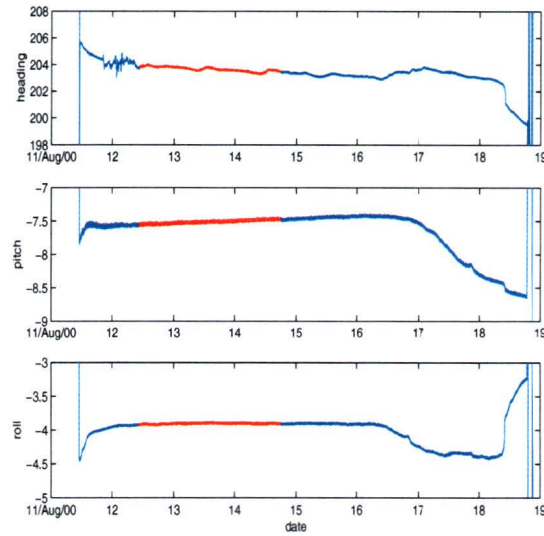


Figure 2.4: Janus tilt angles (in degrees): heading (upper), pitch (middle), roll (lower). Red denotes portion of record used for stress calculation.

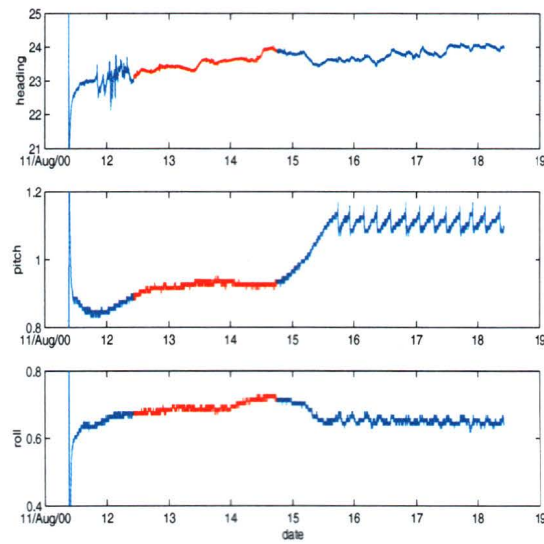


Figure 2.5: Cyclops tilt angles (in degrees): heading (upper), pitch (middle), roll (lower). Red denotes portion of record used for stress calculation.

2.5.2 Velocity comparison

The section of data used for the stress calculations captures two complete daily tidal cycles, and the three Cartesian velocity components (the horizontal components have been rotated as described below) from each instrument along with the associated “error” velocity are pictured in Figures 2.6 (Janus) and 2.7 (Cyclops). The error velocity is the fourth piece of information extracted along with the three Cartesian velocity components, and it is used as an indicator of the quality of the vertical velocity measurement. For a Janus ADCP, vertical velocity estimates higher than $e/3.88$ are considered to be satisfactory (Ott 2000). All of these velocities make the assumption of horizontal homogeneity of the flow over the lengthscale of the beam spread. The tidal flow dominates the horizontal velocities in the upper 50 m of the water column, and is directed south-east to north-west along the axis of the Narrows. Since Sansum Narrows is offset from magnetic north (the reference frame of the Cartesian velocities), principal component analysis was used on the horizontal velocities to determine the angle of maximum variance, and hence the orientation to which the horizontal velocities would be rotated to represent the along-channel and cross-channel flow. It is the along-channel and cross-channel velocities that are pictured in Figures 2.6 and 2.7 rather than the Cartesian u and v . It was determined that 65 degrees west of magnetic north was the optimal angle, which agrees with the orientation of Sansum Narrows (roughly 45 degrees west of true north) with respect to magnetic north (19 degrees east of true north at Sansum Narrows). As the tide floods, the entire water column flows in that direction, but during the ebb tide only the top 40 m of water change direction as the lower column continues to weakly flood. This is a potential indication of flow separation, as the small headland to the northwest of the ADCPs is uphill relative to the southern end of the Narrows and so it blocks the ebbing of deeper waters. As a result, there is significant shear at 40 m depth when the tide turns. When attention is turned to the vertical velocities, the third panel of Figure 2.6 reveals the first problem which results from the significant tilting of the Janus instrument. The vertical velocity, though bin-mapped to correct for the geometric effects of tilt, still appears to contain a daily tidal signature, while the tidal influence is far weaker in the vertical velocity of the Cyclops ADCP. The colour scale of the vertical velocity panels was chosen to best represent the vertical velocities of the Cyclops, and so it may mislead the reader when viewing the tidal signature found in the vertical velocity of the Janus (Figure 2.6). The maximum values of the tidal signature of w do not exceed 0.1 m/s, though that is still much stronger than the anticipated “true” vertical velocity. Recalling Equation (2.61) and using the small angle approximation, the vertical beam of the Cyclops ADCP is given

by

$$b_1 \approx -\phi_3 u_1 + \phi_2 v_1 - w_1. \quad (2.120)$$

Given that the mean tilt angles for the Cyclops are 0.93° and 0.70° for the pitch and roll, respectively, it means that the horizontal velocities must be ≈ 60 times greater (u) and ≈ 80 times greater (v) than the vertical velocity for the tidal currents to overshadow the vertical velocity. The maximum tidal velocities in the channel are on the order of 1 m/s, and the vertical velocities away from the boundaries are on average around 0.02 cm/s, so only at the maximum tidal values is there any evidence of tidal contamination of the vertical velocity.

2.5.3 Stress comparison

Averaged coproducts method

Though velocity records which span the entire height of the water column are available for analysis, only those data at a single depth beneath the main tidal flow, specifically 59.25 m, will be examined. The purpose of this exercise, after all, is not to examine the oceanographic characteristics of the region itself, but it is first and foremost an instrument comparison as they record data in the same *in situ* environment.

To calculate Reynolds stresses from beam velocities, a few issues must first be addressed. The first is the length of time over which the averaging of beam velocities to form beam variances is done. Inherent in the formulation of the Reynolds stress expression is the so-called “Reynolds decomposition” wherein a velocity record is decomposed into a mean flow and the fluctuations around that mean value. The velocities are then squared and averaged over a suitable length of time such that the product of the mean flow with the fluctuations is zero, leaving only the averaged products of the fluctuations, which are the variances and the stresses. There are two timescales involved here; the first being the timescale which separates the ‘mean flow’ from the turbulence fluctuations, and the second being the timescale over which the fluctuation product is averaged to form the Reynolds stress. The velocities were smoothed with a zero-phase, low-pass, fourth-order Butterworth filter (forward and backward) with a cutoff period of 20 minutes. The 20-minute filtered data then represents the mean flow that has retained its tidal signature, as 20 minutes is shorter than the semi-diurnal tidal period, but the turbulent fluctuations have been suppressed as they have a period of shorter than 20 minutes. A similar filter was applied in the analysis of

Lu and Lueck (1999b) and Ott (2000). This mean flow is then subtracted from the velocity record to produce the record of turbulent velocity fluctuations, or the primed velocities. By definition, the mean of the turbulent fluctuations should be zero. This has been verified for the data in question.

Figure 2.8 shows a record of the unfiltered u velocity from the Cyclops ADCP at 59.25 m depth, the 20-minute filtered record, and the resultant turbulent fluctuations. By a similar filtering process, the turbulent fluctuations in v and w can also be obtained. The velocities in question are the “earth” co-ordinate system velocities generated by the ADCP, and hence they assume spatial homogeneity. The coproducts $u'w'$ and $v'w'$ can then be formed from the fluctuation records. To create Reynolds stresses from the coproducts requires a further temporal averaging, so a period of 20 minutes will again be used. This is consistent with Stacey et al. (1999a), Rippeth et al. (2002), and Ott (2000), who all use the same period for both mean flow separation and fluctuation averaging. One might also consider the cospectrum of the turbulent fluctuations when deciding on an averaging timescale. Figure 2.9 shows the cospectral density of $u'w'$, where the Nyquist frequency is 1/20 Hz, which equals one half of the sampling frequency (1 sample per 10 seconds). The period of 20 minutes is marked by a vertical line, and it is clear that to the left of the line, which is to say in the low frequency range, the spectrum is suppressed, and that most of the energy resides at higher frequencies to the right of the 20 minute line. Now this may be expected since the data was essentially high-pass filtered, but one might ask if the filtering alone would cause the entire suppression or was there little energy in that region in the first place, perhaps suggesting a possible “spectral gap”. In an attempt to test this theory, a sequence of random numbers between 0 and 1 which has the same length as the fluctuation record (19900 points) was generated and it was filtered with an identical 4th order high-pass Butterworth filter with a cutoff of 20 minutes. For the sake of comparison, the power spectra of both the original and filtered sequences were taken. It is expected that the spectrum of a string of random numbers (essentially white noise) would be white. Indeed the spectrum of the filtered sequence was white, with the exception of the low-frequency suppression that was expected from the action of the filter. However, the spectrum of the unfiltered sequence was identical to that of the filtered sequence at all frequencies; it too exhibited a low-frequency drop-off in the same frequency range despite the fact that it had not been filtered. Rather than suggest that this is evidence of a spectral gap, it more likely suggests that the low-frequency drop-off in the data is an artifact of the method of calculation used in obtaining the spectrum. A further test of this new hypothesis is to re-calculate the cospectrum of the turbulent fluctuations after increasing the number of

points used in the FFT. The default FFT length used was 256 points, so new spectra were calculated using 512, 1024, and 2048 points. These new spectra along with the original are shown in Figure 2.10. What is found is that as the FFT length increases, the amount of energy at low frequencies appears to increase until it is roughly equal with the energy level at the spectral peak. Returning to the original data, a 256 point section corresponds to a 42 minute period, not much more than the 20 minute period of the filter. This would help to explain why the data appeared to have low-frequency suppression even without filtering. The low-frequency behaviour (which is better seen with a longer FFT) would seem to suggest that choosing 20 minutes as a timescale does not ignore a large amount of energy, as it would if the spectra were increasingly red with increasing FFT length.

Figure 2.11 shows the Reynolds stress $-\overline{u'w'}$ as formed from averaging the Cyclops coproduct over 20 minute periods, while Figure 2.12 displays the $-\overline{v'w'}$ stress formed in the same manner. Not much will be said about these stresses at this time, but they will be used for comparison with the stress estimates as formed from the beam variance method.

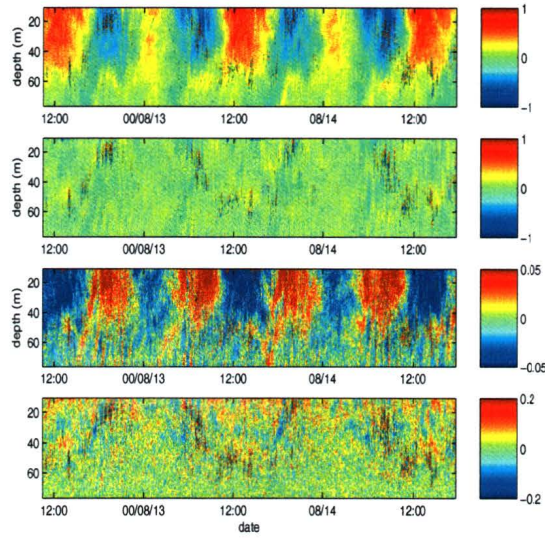


Figure 2.6: Janus “earth” velocities. Along-channel (upper) and cross-channel (upper-middle) horizontal velocities, w (lower-middle), and “ e ” (lower). All velocities are in m/s .

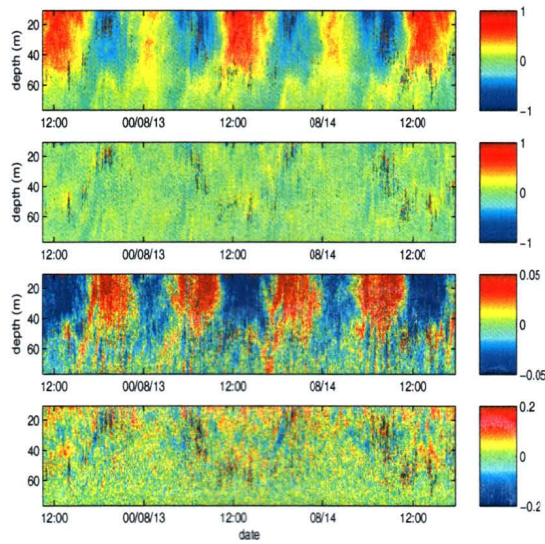


Figure 2.7: Cyclops “earth” velocities. Along-channel (upper) and cross-channel (upper-middle) horizontal velocities, w (lower-middle), and “ e ” (lower). All velocities are in m/s .

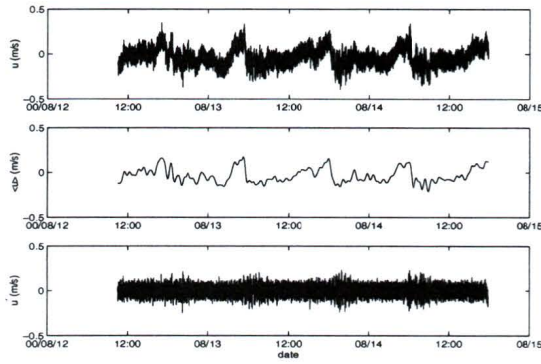


Figure 2.8: u velocity in Reynolds decomposition. u (upper), \bar{u} (middle), u' (lower)

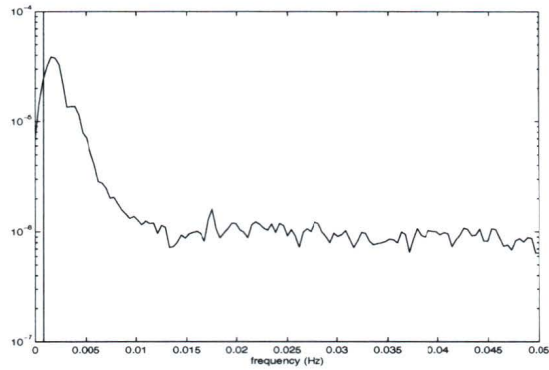


Figure 2.9: Cospectrum of $u'w'$. $f_N = 1/20Hz$

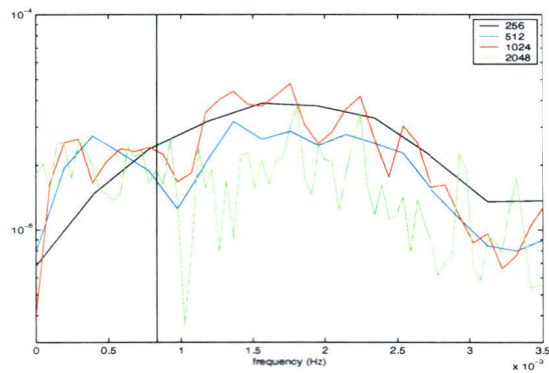


Figure 2.10: Cospectra of $u'w'$ with different FFT lengths. $f_N = 1/20Hz$

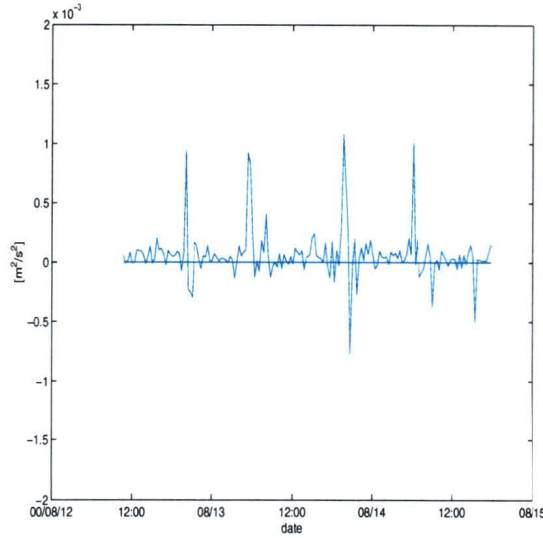


Figure 2.11: $-\overline{u'w'}$ from Cyclops using the averaged coproducts method with 20 minute averaging.

Beam variance method

The formulations of the Reynolds stresses found in Figures 2.11 and 2.12 are the basic averaged coproduct of two turbulent velocity fluctuations, assuming spatial homogeneity when calculating the Cartesian velocity components. For the Cyclops ADCP with nearly zero tilt, as is the case in this deployment, this coproduct formulation of the stress should be reasonably accurate since the vertical beam will resolve w very well on its own without contamination from u and v . Unfortunately, this cannot be said for the Janus deployment with its significant level of tilt. The method of extracting Reynolds stresses which has been examined in earlier sections, however, involves the rearrangement of the variances of the beam velocities to form the stress expressions. Since the beam variance expressions contain “unknown” bias terms involving $\overline{u'^2}$, $\overline{v'^2}$, $\overline{w'^2}$, and $\overline{u'v'}$, it would be helpful to have data for u' , v' , and w' so that the bias terms could be calculated. These velocity fluctuations can be calculated using the method of Section 2.5.3. Spatial homogeneity is required to calculate the fluctuations, but this is more acceptable than using spatial homogeneity to directly calculate $\overline{u'w'}$ and $\overline{v'w'}$ since the bias terms are generally smaller in magnitude with their coefficients involving various degrees of ϕ . In this manner, only statistical homogeneity (recalling that “statistical” homogeneity implies spatial homogeneity only of the turbulent statistics of the flow) is required for the calculation of $\overline{u'w'}$ and $\overline{v'w'}$, while the more rigid

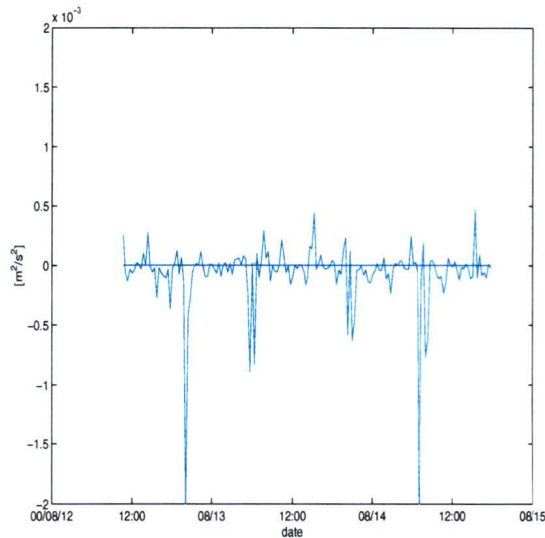


Figure 2.12: $-\overline{v'w'}$ from Cyclops using the averaged coproducts method with 20 minute averaging.

spatial homogeneity (of the flow itself) is only required in the calculation of the bias terms. Since the necessary data products u' , v' , and w' can now be calculated for both the Janus and the Cyclops instruments, the Reynolds stresses as given in equations (2.24) and (2.25) for the Janus and (2.72) and (2.73) for the Cyclops can be evaluated.

In order to determine the Reynolds stress at a desired depth, it must be determined which bin in each beam corresponds to that depth. The beam angle from the vertical for the slanted transducers of both instruments is nominally 20° , but non-zero pitch and roll angles will modify the angle each beam makes with the vertical. The manufacturer-recorded elevations for the Janus ADCP are 20.23° , 20.52° , 20.35° , and 19.92° for beams 1 through 4, respectively, but the difference between the sine and cosine of the largest of these angles and the nominal value is less than 1%. Exact beam elevations are not known for the Cyclops ADCP, so the nominal values must suffice. To determine the appropriate angles for each instrument, the fully rotated beam equations must be recalled. For the Janus ADCP, the beam velocity equations with full pitch and roll are

$$\begin{aligned}
b_1 &= -u_1 \sin(\theta + \phi_3) + v_1 \sin \phi_2 \cos(\theta + \phi_3) - w_1 \cos \phi_2 \cos(\theta + \phi_3) \\
b_2 &= u_2 \sin(\theta - \phi_3) + v_2 \sin \phi_2 \cos(\theta - \phi_3) - w_2 \cos \phi_2 \cos(\theta - \phi_3) \\
b_3 &= -u_3 \sin \phi_3 \cos \theta - v_3 (\cos \phi_2 \sin \theta - \sin \phi_2 \cos \phi_3 \cos \theta) \\
&\quad -w_3 (\cos \phi_2 \cos \phi_3 \cos \theta + \sin \phi_2 \sin \theta) \\
b_4 &= -u_4 \sin \phi_3 \cos \theta + v_4 (\cos \phi_2 \sin \theta + \sin \phi_2 \cos \phi_3 \cos \theta) \\
&\quad -w_4 (\cos \phi_2 \cos \phi_3 \cos \theta - \sin \phi_2 \sin \theta).
\end{aligned}$$

The projection of each of these beams onto the vertical axis is just the coefficient of the vertical velocities w_1 through w_4 , so that the angles θ_{j1} through θ_{j4} between each beam and the vertical are given by

$$\cos \theta_{j1} = \cos \phi_2 \cos(\theta + \phi_3) \quad (2.121)$$

$$\cos \theta_{j2} = \cos \phi_2 \cos(\theta - \phi_3) \quad (2.122)$$

$$\cos \theta_{j3} = \cos \phi_2 \cos \phi_3 \cos \theta + \sin \phi_2 \sin \theta \quad (2.123)$$

$$\cos \theta_{j4} = \cos \phi_2 \cos \phi_3 \cos \theta - \sin \phi_2 \sin \theta. \quad (2.124)$$

Inserting the mean values of $\overline{\phi_2} = -7.5^\circ$ and $\overline{\phi_3} = -3.9$, and the known beam angle $\theta = 20^\circ$, the angles are found to be $\theta_{j1} = 17.7^\circ$, $\theta_{j2} = 25.0^\circ$, $\theta_{j3} = 27.8^\circ$, and $\theta_{j4} = 13.0^\circ$. Now that the angles between the vertical and the beam directions are known, the manner of data storage comes into question. The Janus ADCP collected data in 85 1 m bins, as noted in Table 2.1. The first bin was located 2.75 m above bottom and the corresponding water depth of that bin was 77.25 m. The selected depth of 59.25 m is recorded in bin 19, with a corresponding height above bottom of 20.75 m. So a vertical beam would have recorded the selected depth at bin 19; where then would beams which have experienced both pitch and roll rotations record that depth? Figure A.1 shows the relationship between the vertical axis and a given slanted beam, namely that

$$z_i = \frac{z_v}{\cos \theta_{ji}}, \quad (2.125)$$

where z_i is the length of the i^{th} beam, z_v is the length of the vertical axis, and θ_{ji} is the i^{th} beam angle. Using $z_v = 20.75$ m, the beam lengths are calculated as $z_1 = 21.78$ m, $z_2 = 22.89$ m, $z_3 = 23.45$ m, and $z_4 = 21.30$ m. Each beam velocity is linearly interpolated

to find the values at the length specific to that beam, as using linearly interpolated data can reduce error by an order of magnitude compared to using the “nearest neighbour” bin method of data selection (Ott 2002). The velocity records at those interpolated lengths are used for calculating the Reynolds stresses for a desired height above the bottom from the beam variance method.

Now the beams from the Cyclops must be mapped in a similar fashion. The fully tilted Cyclops beam velocities are given as

$$\begin{aligned}
b_1 &= -u_1 \sin \phi_3 + v_1 \sin \phi_2 \cos \phi_3 - w_1 \cos \phi_2 \cos \phi_3 \\
b_2 &= -u_2 \sin \phi_3 \cos \theta + v_2 (\cos \phi_2 \sin \theta + \sin \phi_2 \cos \phi_3 \cos \theta) \\
&\quad - w_2 (\cos \phi_2 \cos \phi_3 \cos \theta - \sin \phi_2 \sin \theta) \\
b_3 &= u_3 \left(\cos \phi_3 \sin \theta \sin \frac{\pi}{3} - \sin \phi_3 \cos \theta \right) \\
&\quad - v_3 \left[\left(\cos \phi_2 \cos \frac{\pi}{3} - \sin \phi_2 \sin \phi_3 \sin \frac{\pi}{3} \right) \sin \theta - \sin \phi_2 \cos \phi_3 \cos \theta \right] \\
&\quad - w_3 \left[\left(\sin \phi_2 \cos \frac{\pi}{3} + \cos \phi_2 \sin \phi_3 \sin \frac{\pi}{3} \right) \sin \theta + \cos \phi_2 \cos \phi_3 \cos \theta \right] \\
b_4 &= -u_4 \left(\cos \phi_3 \sin \theta \sin \frac{\pi}{3} + \sin \phi_3 \cos \theta \right) \\
&\quad - v_4 \left[\left(\cos \phi_2 \cos \frac{\pi}{3} + \sin \phi_2 \sin \phi_3 \sin \frac{\pi}{3} \right) \sin \theta - \sin \phi_2 \cos \phi_3 \cos \theta \right] \\
&\quad - w_4 \left[\left(\sin \phi_2 \cos \frac{\pi}{3} - \cos \phi_2 \sin \phi_3 \sin \frac{\pi}{3} \right) \sin \theta + \cos \phi_2 \cos \phi_3 \cos \theta \right].
\end{aligned}$$

The projection of these beams onto the vertical axis, then, creates angles θ_{c1} through θ_{c4} given by

$$\cos \theta_{c1} = \cos \phi_2 \cos \phi_3 \quad (2.126)$$

$$\cos \theta_{c2} = \cos \phi_2 \cos \phi_3 \cos \theta - \sin \phi_2 \sin \theta \quad (2.127)$$

$$\cos \theta_{c3} = \left(\sin \phi_2 \cos \frac{\pi}{3} + \cos \phi_2 \sin \phi_3 \sin \frac{\pi}{3} \right) \sin \theta + \cos \phi_2 \cos \phi_3 \cos \theta \quad (2.128)$$

$$\cos \theta_{c4} = \left(\sin \phi_2 \cos \frac{\pi}{3} - \cos \phi_2 \sin \phi_3 \sin \frac{\pi}{3} \right) \sin \theta + \cos \phi_2 \cos \phi_3 \cos \theta. \quad (2.129)$$

The mean pitch and roll angles for the Cyclops are known to be $\overline{\phi_2} = 0.93^\circ$ and $\overline{\phi_3} = 0.70^\circ$, respectively. Applying these angles along with the standard beam angle $\theta = 20^\circ$ to equations (2.126) through (2.129) yields total beam angles of $\theta_{c1} = 1.14^\circ$, $\theta_{c2} = 20.91^\circ$, $\theta_{c3} = 19.04^\circ$, and $\theta_{c4} = 20.29^\circ$. The required depth of 59.25 m is found in bin 20, at a

corresponding height above bottom of 21.75 m. Using this height in equation (2.125), the beam lengths for the Cyclops are found to be $z_1 = 21.75$ m, $z_2 = 23.28$ m, $z_3 = 23.01$ m, and $z_4 = 23.19$ m. In a similar fashion as before, the beam velocities are interpolated to find velocity records at the desired lengths for use in the beam variance method. One point which must be addressed is the use of mean pitch and roll values in both mappings. Variable tilt angles introduce additional biases to Reynolds stress values calculated using the beam variance method (Lu and Lueck, 1999). These biases were not considered in the algebraic investigations, but will be qualitatively examined shortly.

Given that all the mean pitch and roll angles are sufficiently small that the small angle approximations are reasonable (the maximum error is 0.8% found in the cosine approximation of $\overline{\phi_2}$), the small angle forms of the Reynolds stresses, namely equations (2.24) and (2.25), and equations (2.72) and (2.73) for the Janus and Cyclops, respectively, will be used. Substituting all of the relevant data products from the correct bins into equations (2.24) and (2.25), then, give the Reynolds stresses for the Janus ADCP via the beam variance method. Figure 2.13 shows the $-\overline{u'w'}$ Reynolds stress as calculated using a 20 minute averaging period, while Figure 2.14 shows the $-\overline{v'w'}$ stress using the same averaging period. Each figure also displays the values of the undetermined terms in each expression, so that one may clearly see if a particular bias term is dominating the stress or if the bias terms are at an acceptably low level relative to the stress values. For the Janus stresses the undetermined terms containing $\overline{u'^2}$ and $\overline{v'^2}$ appear to be the major component in the stress values, despite the multiplication by the small tilt angles. By comparison, the $\overline{w'^2}$ and $\overline{u'v'}$ terms contribute only a small amount to each stress. In Section 2.1.2, however, these undetermined terms were removed from equations (2.24) and (2.25) and replaced using the sums rather than the differences of the beam variance pairs, yielding equations (2.34) and (2.35) as new Reynolds stress expressions for the Janus. The new stress expressions, and the contributions of their respective bias terms, for $-\overline{u'w'}$ and $-\overline{v'w'}$ are shown in Figures 2.15 and 2.16, respectively. In these cases the bias terms containing $\overline{u'v'}$ are still much smaller than the total stresses and are clearly not the dominant terms. However, the $\overline{w'^2}$ terms are now considerably larger, given that their coefficients have been increased by a factor of $1/\sin^2 20^\circ$, or almost ten-fold. Despite this, the total (contributions from both known beam variance terms and estimated stress tensor terms) stresses (solid blue lines) are much closer to the unbiased (contribution from only known beam variance terms) stresses (dotted blue lines) than they are in Figures 2.13 and 2.14. While there is no standard by which to judge the validity of this Reynolds stress estimate, it is encouraging to see that the effect of the bias terms has now been slightly reduced. Recall also that in Section 2.1.2 it was shown that calculating

the unknown bias terms using the velocity estimates of the ADCP was acceptable despite the assumption of spatial homogeneity by the ADCP. A final adjustment can be made to the Janus Reynolds stress estimates by noting that the lower portion of Sansum Narrows is oriented approximately 45° west of north, and as such the channel dynamics would be more oceanographically relevant in an along-channel and cross-channel coordinate frame. A principal component analysis of the beam velocities showed that the beams were 165° from the orientation of maximum variance, so the stress estimates of equations (2.34) and (2.35) were rotated by that angle and are shown in cross-channel and along-channel form in Figures 2.17 and 2.18. What is now evident is that Reynolds stress is exhibiting significant peaks which correspond to the times of ebb tide when the vertical shear is greatest.

Now the same procedure can be followed with the Reynolds stress expressions for the Cyclops ADCP as given by equations (2.72) and (2.73). Figures 2.19 and 2.20 show $-\overline{u'w'}$ and $-\overline{v'w'}$, respectively, with the contributions from the bias terms. Figure 2.19 shows a small contribution from each of the bias terms to the overall $-\overline{u'w'}$ expression. The dominant bias terms in the Cyclops expression, those containing $\overline{u'^2}$ and $\overline{v'^2}$, are reduced since the roll angle ϕ_3 is very small ($\overline{\phi_3} = 0.012$ rad). The term which is not multiplied by a tilt angle, $\overline{u'v'}$, is naturally much smaller than $\overline{u'^2}$ and $\overline{v'^2}$ because u' and v' are not perfectly correlated. The same does not hold for the $-\overline{v'w'}$ expression, however, as Figure 2.20 shows that the dominant term is the $\overline{v'^2}$ bias term, which is not multiplied by a tilt angle in equation (2.73). This was an anticipated shortcoming of the Cyclops beam configuration. A reasonable comparison can be made between the Cyclops stress estimates of Figures 2.19 and 2.20 using the beam variance method and those of Figures 2.11 and 2.12 to see if the beam variance method is yielding plausible stress estimates. A comparison of the $-\overline{u'w'}$ figures shows some similarities, with four major stress peaks in roughly the same time periods, though the magnitudes vary somewhat. The $-\overline{v'w'}$ figures, however, are not very similar, which is an obvious consequence of the size of the $\overline{v'^2}$ bias term in Figure 2.20. Another comparison which can be made is between the Janus and Cyclops expressions for the along-channel and cross-channel stresses, once the Cyclops stresses are rotated into the appropriate coordinate frame. A principal component analysis similar to that used on the Janus beams showed that the Cyclops beams required a rotation of -165° . The stresses were so rotated, and are shown along with the rotated Janus stresses in Figures 2.21 and 2.22. The along-channel stresses for both instruments show some similarities, while the cross-channel stresses, despite showing consistent peaks, are offset by a significant amount, a likely consequence of the $\overline{v'^2}$ bias in the Cyclops stress expression. It bears remembering at this point, though, that the Janus and Cyclops ADCPs are physically separated by a

distance of approximately 100 m, so the exact details of the stress can hardly be expected to be fully coherent across such a large lengthscale.

As previously mentioned, the variation of tilt angles with time will introduce further bias terms to the stress estimates, though they have been neglected here due to the assumption that they are small. Lu and Lueck (1999) point out that, for a Janus ADCP, a number of tilt-velocity correlation terms will appear in the Reynolds stress estimates if tilt angles are allowed to vary over the averaging interval. The largest such term that they consider is $\overline{u' \phi_3}$ for the case of variable roll and zero pitch. Similar terms would appear if the pitch was variable. They note that the product of a 2° rms tilt-angle fluctuation and a 0.1 m/s rms velocity fluctuation in a mean flow of 1 m/s would give rise to a $4 \times 10^{-4} \text{m}^2/\text{s}^2$ bias in Reynolds stress even if the correlation coefficient between the roll and the velocity were 0.1. This, they say, would be too large for most practical flows. Fortunately, the rms tilt angle fluctuations in these data sets are much lower. The rms values of the tilt fluctuations for the Janus angles are 0.03 for ϕ_2 and 0.001 for ϕ_3 , and for the Cyclops the rms fluctuations in tilt are 0.01 for both ϕ_2 and ϕ_3 . Figure 2.23 shows a histogram of $|u'|$. The median value of the turbulent fluctuations is 0.03 m/s. If the largest tilt fluctuation listed above and the velocity fluctuations were perfectly correlated, that would cause a bias of 2×10^{-5} m/s. However, the fluctuations are not perfectly correlated, so using the same arbitrary correlation coefficient of 0.1 and calculating that the average of the absolute value of the mean flow record is 0.07 m/s reduces the bias to $1 \times 10^{-7} \text{m}^2/\text{s}^2$; an acceptable level. As such, the approximation of rigid tilt angles is justified.

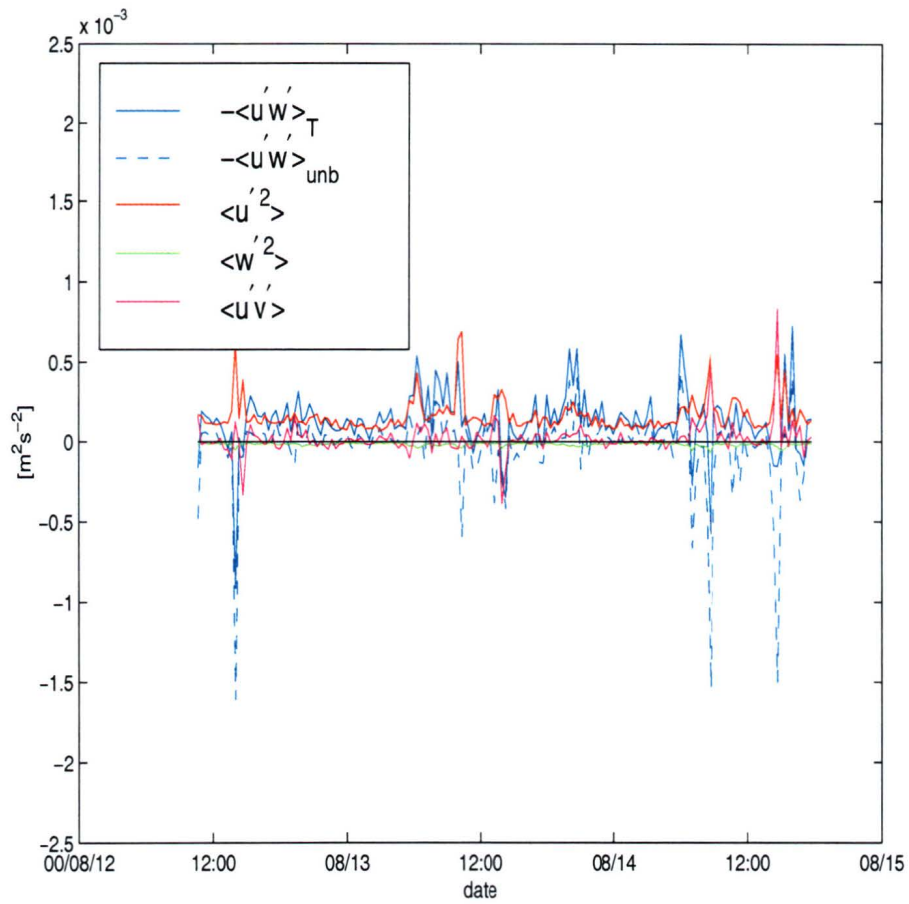


Figure 2.13: $-\overline{u'w'}$ from Janus using equation (2.24). The dotted line is the stress excluding bias terms, while the red, green, and magenta lines are the contributions from the $\overline{u'^2}$, $\overline{w'^2}$, and $\overline{u'v'}$ terms, respectively.

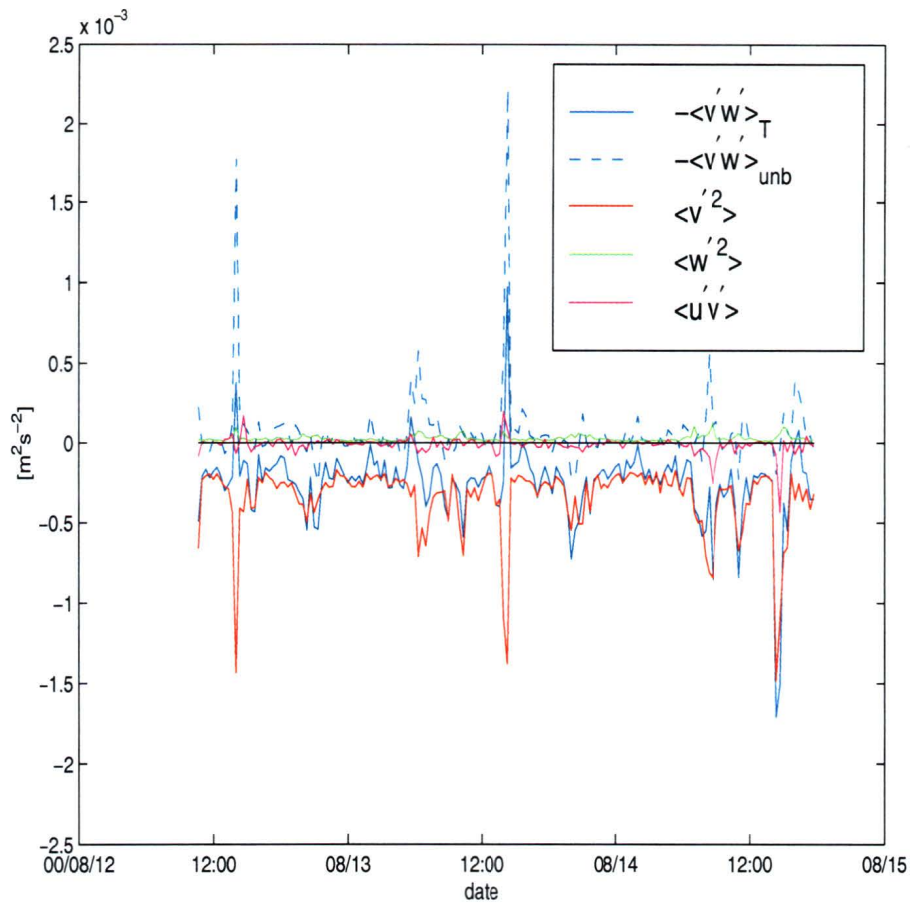


Figure 2.14: $-\overline{v'w'}$ from Janus using equation (2.25). The dotted line is the stress excluding bias terms, while the red, green, and magenta lines are the contributions from the $\overline{v'^2}$, $\overline{w'^2}$, and $\overline{u'v'}$ terms, respectively.

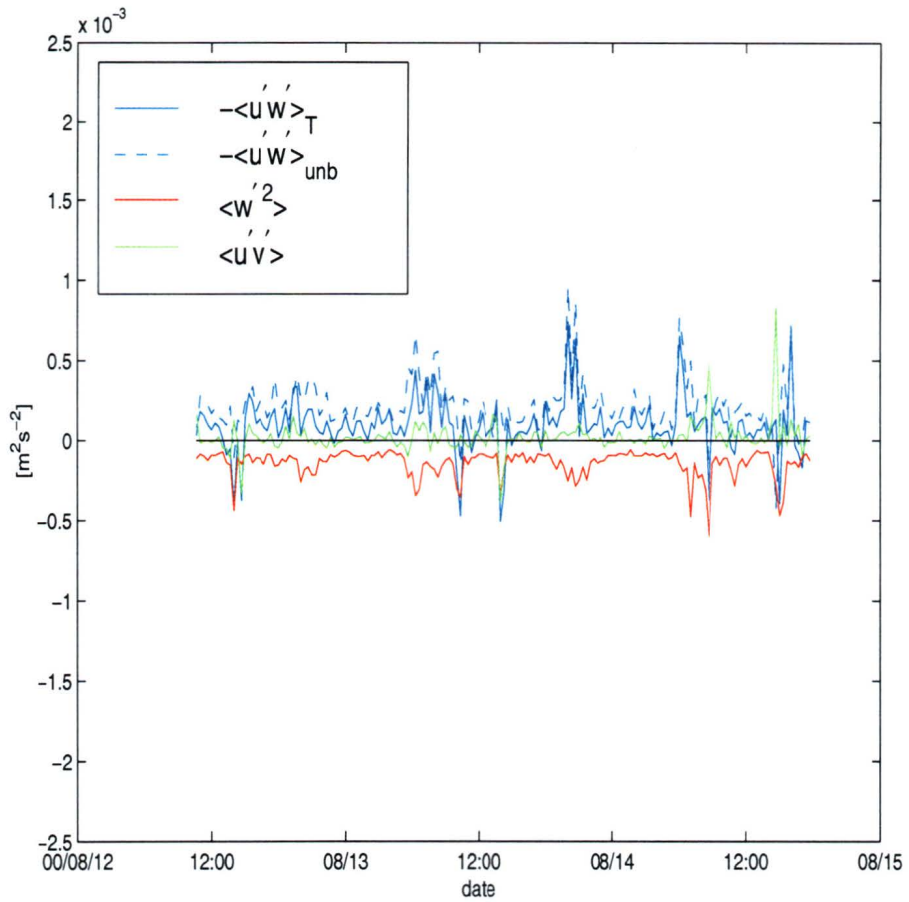


Figure 2.15: $-\overline{u'w'}$ from Janus using equation (2.34). The dotted line is the stress excluding bias terms, while the red and green lines are the contributions from the $\overline{w'^2}$ and $\overline{u'v'}$ terms, respectively.

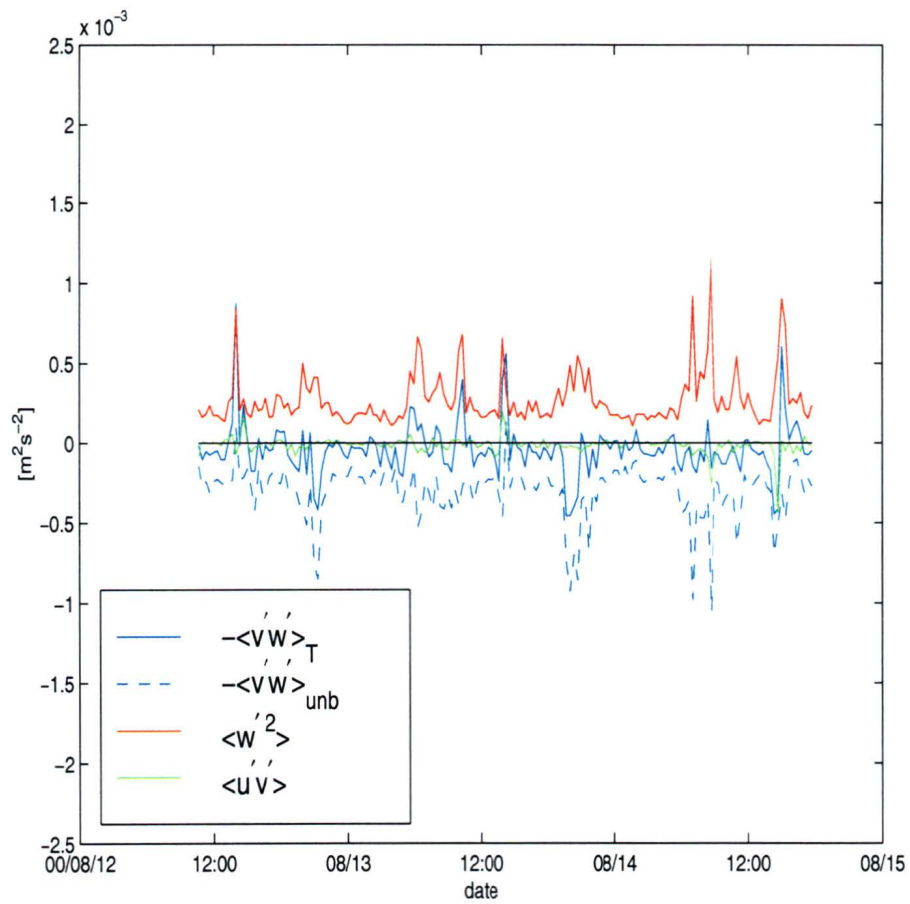


Figure 2.16: $-\overline{v'w'}$ from Janus using equation (2.35). The dotted line is the stress excluding bias terms, while the red and green lines are the contributions from the w'^2 and $u'v'$ terms, respectively.

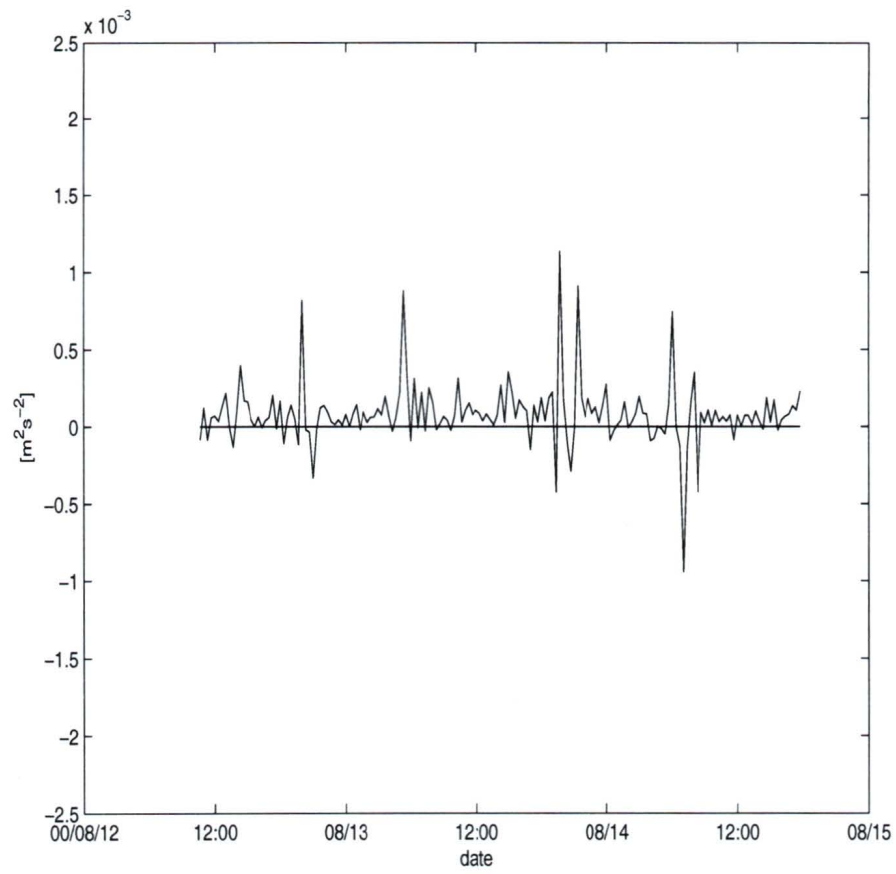


Figure 2.17: Along-channel Reynolds stress from Janus

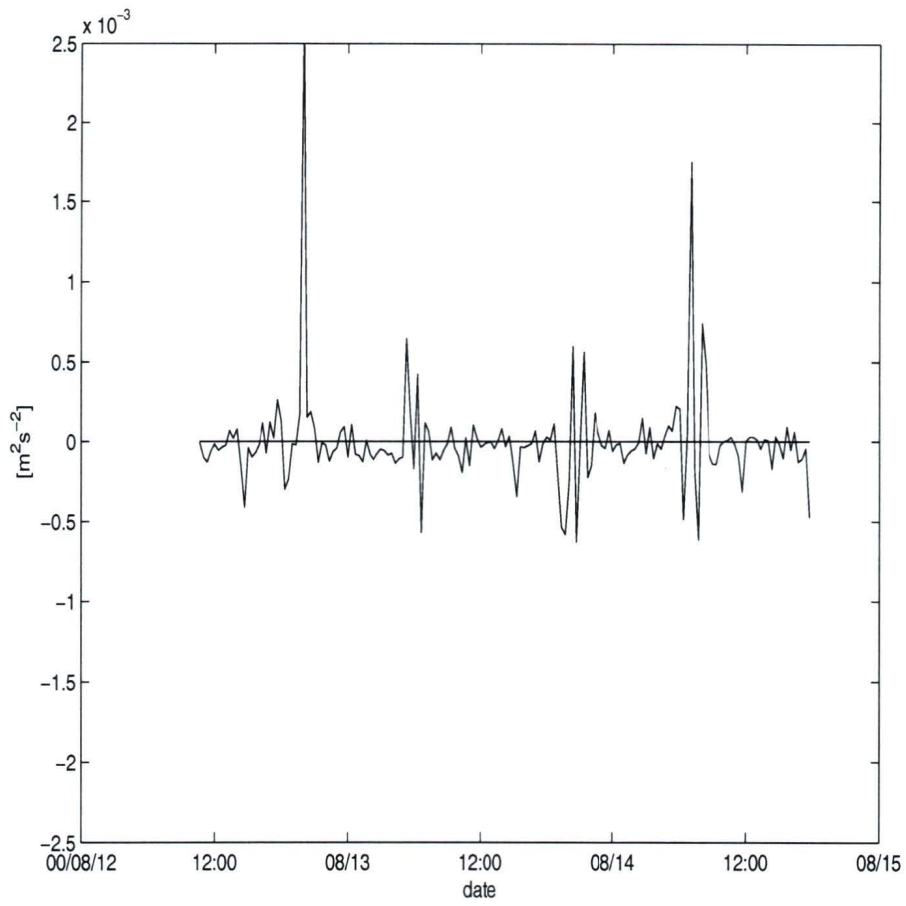


Figure 2.18: Cross-channel Reynolds stress from Janus

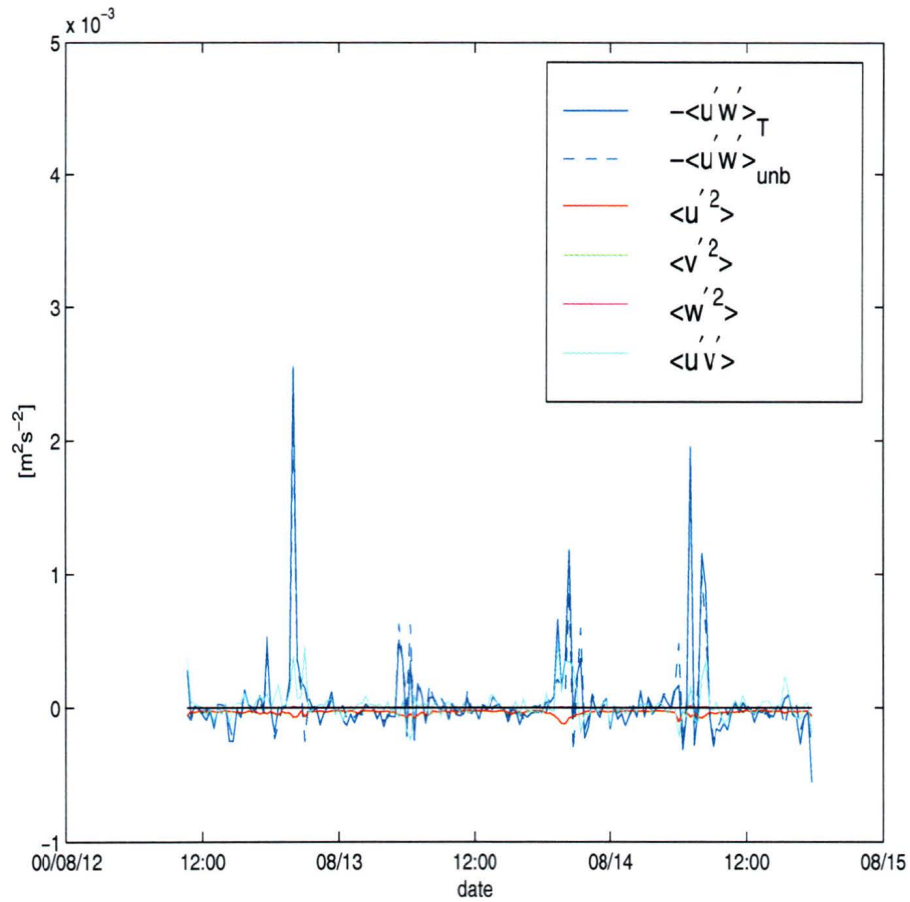


Figure 2.19: $-\overline{u'w'}$ from Cyclops using equation (2.72). The dotted line is the stress excluding bias terms, while the red, green, magenta, and cyan lines are the contributions from the $\overline{u'^2}$, $\overline{v'^2}$, $\overline{w'^2}$, and $\overline{u'v'}$ terms, respectively.

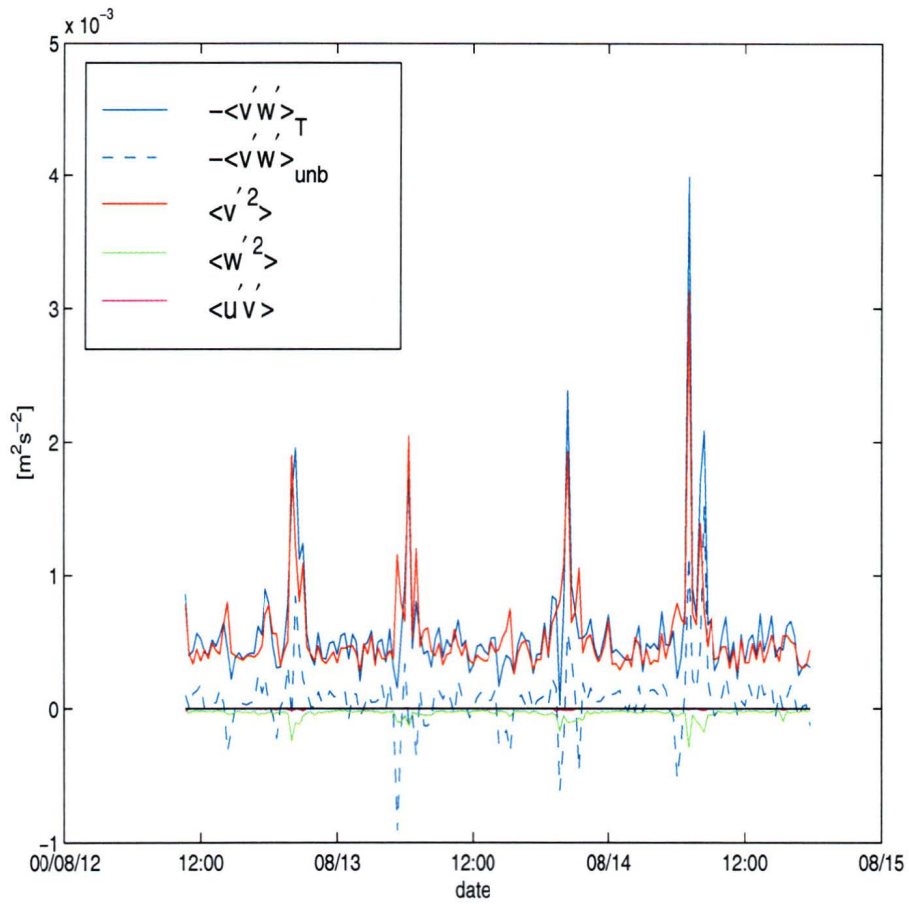


Figure 2.20: $-\overline{v'w'}$ from Cyclops using equation (2.73). The dotted line is the stress excluding bias terms, while the red, green, and magenta lines are the contributions from the $\overline{v'^2}$, $\overline{w'^2}$, and $\overline{u'v'}$ terms, respectively.

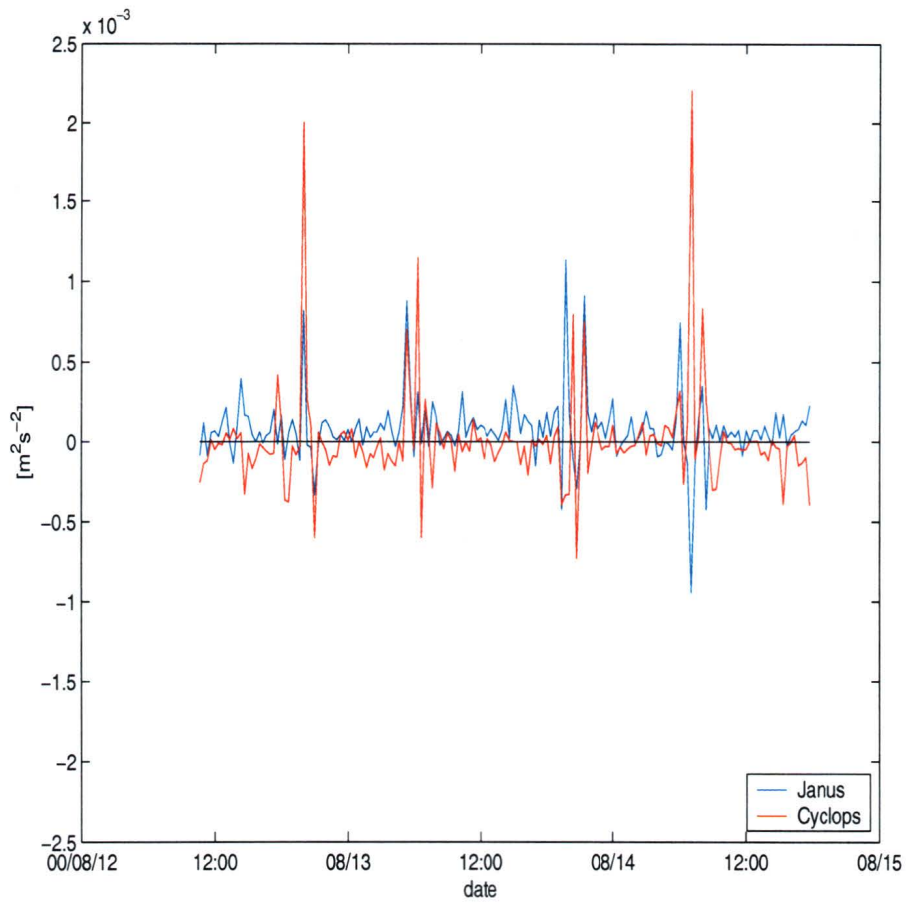


Figure 2.21: Along-channel Reynolds stress from Janus and Cyclops. The blue line is the rotated Janus stress using equation (2.34) while the red line is the Cyclops stress using equation (2.72).

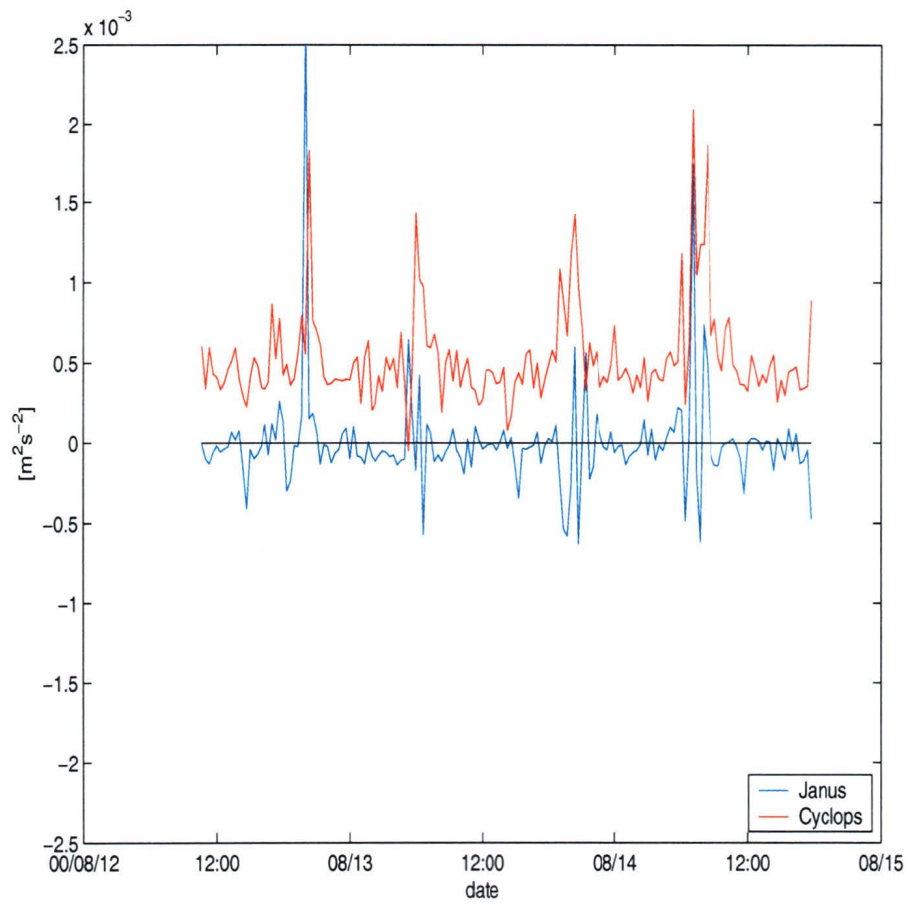


Figure 2.22: Cross-channel Reynolds stress from Janus and Cyclops. The blue line is the rotated Janus stress using equation and (2.35) while the red line is the Cyclops stress using equation (2.73).

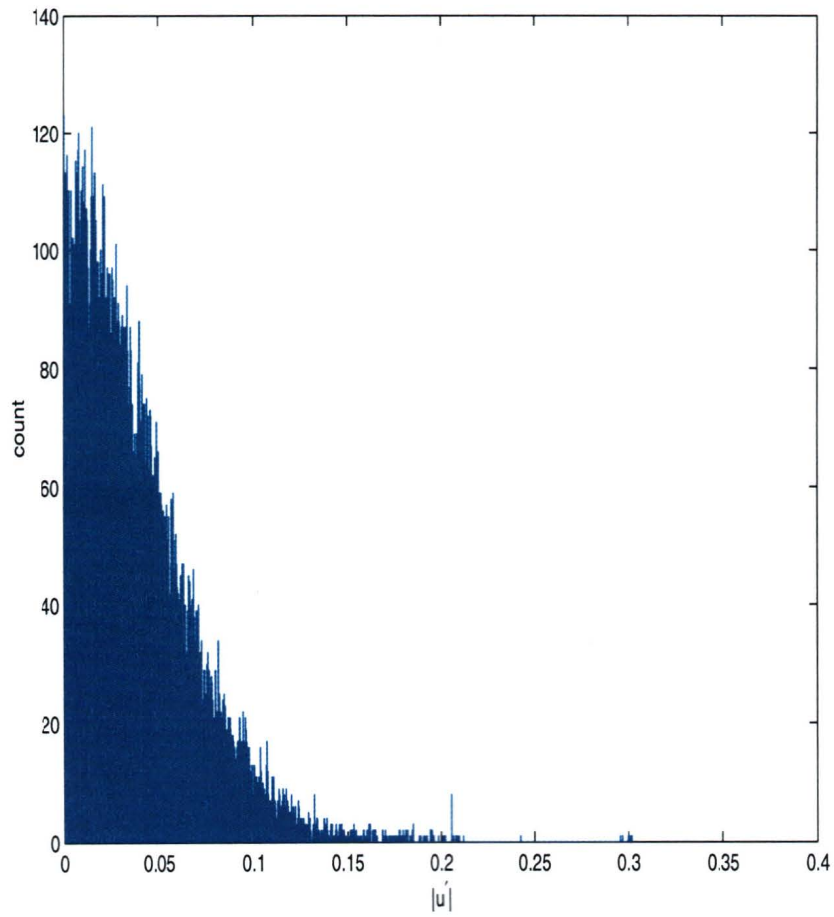


Figure 2.23: Histogram of $|u'|$.

Chapter 3

Internal Tides

As noted earlier, the energy flux generated by supercritical topography such as steps and knife edge ridges cannot be calculated using the linear theory of Bell (1975), so numerical methods must be employed. The first topography to be treated is the step.

3.1 Step Topography

3.1.1 Stigebrandt formulation

In a previous work, Stigebrandt (1980) attempts to define the structure of internal waves on the deep side of a sill in a non-rotating, continuously stratified fjord, shown in figure 3.1. He gives the horizontal velocity of the n th mode as

$$u'_n = a_n \cos \frac{n\pi z}{H} \cos(kx + \omega t) \quad n = 1, 2, 3, \dots, \quad (3.1)$$

where a_n is the current amplitude, H is the water depth, k is the horizontal wave number and ω is the frequency. These waves are propagating away from the step into the deep ocean. The dispersion relation for the waves is

$$\omega = \frac{kNH}{n\pi} \quad n = 1, 2, 3, \dots \quad (3.2)$$

Since the density profile is linear, the buoyancy frequency, N , is constant. Combined with the constant water depth, this implies that the wave number is proportional to the mode number n . Relabelling Stigebrandt's barotropic amplitude from α to u_o , the deep-ocean barotropic current speed is defined as $\overline{u_1} = u_o \cos \omega t$. Noting that the internal waves do not contribute to any net horizontal transport, the barotropic current on the sill is thus

$$\overline{u_2} = u_o \frac{H}{d} \cos \omega t \quad -d < z \leq 0. \quad (3.3)$$

Matching the total barotropic and wave current on both sides of the sill ($x = 0$), and defining the ratio of sill depth to water depth as $\delta_s = d/H$, the horizontal current boundary condition at the sill is

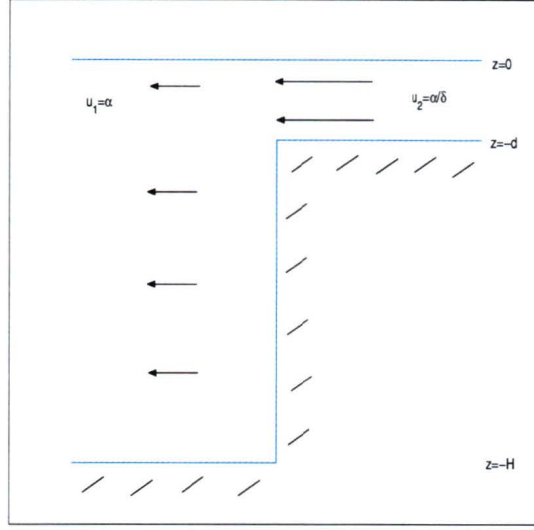


Figure 3.1: The Stigebrandt (1980) shelf problem

$$u_o + \sum_{n=1}^{\infty} a_n \cos \frac{n\pi z}{H} = \frac{u_o}{\delta_s} \quad -d < z \leq 0 \quad (3.4)$$

$$u_o + \sum_{n=1}^{\infty} a_n \cos \frac{n\pi z}{H} = 0 \quad -H \leq z \leq -d. \quad (3.5)$$

Using the orthogonality of the cosine function, the wave amplitude is found to be

$$a_n = \frac{2u_o}{n\pi\delta_s} \sin n\pi\delta_s. \quad (3.6)$$

This approach to the problem does not explicitly include internal waves on the shelf-side of the sill, which clearly should exist. A complete formulation of the problem is required to understand the nature of the solution over the full range of the parameter δ_s without approximation.

3.1.2 Complete formulation

To reset the problem, the governing equations are first outlined, namely the linearised, rotating, frictionless momentum equations for a Boussinesq fluid,

$$\frac{\partial u}{\partial t} - fv = -\frac{1}{\rho_o} \frac{\partial p}{\partial x} \quad (3.7)$$

$$\frac{\partial v}{\partial t} + fu = -\frac{1}{\rho_o} \frac{\partial p}{\partial y} \quad (3.8)$$

$$\frac{\partial w}{\partial t} = -\frac{1}{\rho_o} \frac{\partial p}{\partial z} - \frac{\rho g}{\rho_o}, \quad (3.9)$$

and the continuity equation

$$\frac{\partial u}{\partial x} + \frac{\partial w}{\partial z} = 0. \quad (3.10)$$

The total current can be decomposed into barotropic (depth-independent) and baroclinic (depth-varying) components

$$u_1 = \bar{u}_1 + u'_1 \quad (3.11)$$

$$u_2 = \bar{u}_2 + u'_2. \quad (3.12)$$

The barotropic current in the full water column is denoted as $\bar{u}_1 = u_o \cos \omega t$, and that over the sill, by continuity, as $\bar{u}_2 = \frac{u_o}{\delta_s} \cos \omega t$. The baroclinic motions off and on the shelf, respectively, are given as

$$u'_1 = \sum_{n=1}^{\infty} u'_{1n} \quad (3.13)$$

$$u'_2 = \sum_{n=1}^{\infty} u'_{2n}, \quad (3.14)$$

where

$$u'_{1n} = a_n \cos \frac{n\pi z}{H} \exp(ik_1 x - i\omega t), \quad k_1 = -\frac{n\pi}{H} \left(\frac{\omega^2 - f^2}{N^2 - \omega^2} \right)^{1/2} \quad (3.15)$$

$$u'_{2n} = b_n \cos \frac{n\pi z}{d} \exp(ik_2 x - i\omega t), \quad k_2 = \frac{n\pi}{d} \left(\frac{\omega^2 - f^2}{N^2 - \omega^2} \right)^{1/2} = -\frac{k_1}{\delta_s}. \quad (3.16)$$

The waves u'_1 propagate from the step into the deep ocean, while the waves u'_2 radiate onto

the shelf. Since a_n and b_n each carry units of velocity, they can be non-dimensionalised by dividing each by the barotropic amplitude u_o . The new non-dimensional modal coefficients are now defined as $a_n^* = \frac{a_n}{u_o}$ and $b_n^* = \frac{b_n}{u_o}$. Finally, the stars are dropped for clarity and equations (3.15) and (3.16) become

$$u'_{1n} = a_n u_o \cos \frac{n\pi z}{H} \exp(ik_1 x - i\omega t), \quad k_1 = -\frac{n\pi}{H} \left(\frac{\omega^2 - f^2}{N^2 - \omega^2} \right)^{1/2} \quad (3.17)$$

$$u'_{2n} = b_n u_o \cos \frac{n\pi z}{d} \exp(ik_2 x - i\omega t), \quad k_2 = \frac{n\pi}{d} \left(\frac{\omega^2 - f^2}{N^2 - \omega^2} \right)^{1/2} = -\frac{k_1}{\delta_s} \quad (3.18)$$

so that the total real horizontal current on each side of the sill can be written as

$$u_1 = u_o \cos \omega t + \sum_{n=1}^{\infty} a_n u_o \cos \frac{n\pi z}{H} \cos(k_1 x - \omega t) \quad (3.19)$$

$$u_2 = \frac{u_o}{\delta} \cos \omega t + \sum_{n=1}^{\infty} b_n u_o \cos \frac{n\pi z}{d} \cos(k_2 x - \omega t). \quad (3.20)$$

The total horizontal current on each side of the sill, then, is the sum of the barotropic and baroclinic currents on each side. They must match across the sill ($x = 0$), as they do in Stigebrandt's formulation. To be rigorous, this will be proven via the continuity equation. The only assumption that will be made is that all quantities are finite; specifically that $\partial w / \partial z$ is finite. Equation (3.10) is integrated horizontally across the boundary from $x = -\epsilon$ to $x = \epsilon$ to give

$$\int_{-\epsilon}^{\epsilon} \left(\frac{\partial u}{\partial x} + \frac{\partial w}{\partial z} \right) dx = 0$$

$$u|_{-\epsilon}^{\epsilon} + \left(\frac{\partial w}{\partial z} \right) 2\epsilon = 0. \quad (3.21)$$

As $\epsilon \rightarrow 0$, the second term on the right-hand side goes to zero, and hence

$$u|_{-\epsilon}^{\epsilon} = 0, \quad (3.22)$$

which verifies that the total horizontal current is continuous across $x = 0$. By modifying the S80 horizontal current boundary condition to include the internal waves given in equations

(3.19) and (3.20), and dividing by the barotropic velocity, a new boundary condition for the horizontal velocity is

$$1 + \sum_{n=1}^{\infty} a_n \cos \frac{n\pi z}{H} = \frac{1}{\delta_s} + \sum_{n=1}^{\infty} b_n \cos \frac{n\pi z}{d} \quad -d < z \leq 0 \quad (3.23)$$

$$1 + \sum_{n=1}^{\infty} a_n \cos \frac{n\pi z}{H} = 0 \quad -H \leq z \leq -d. \quad (3.24)$$

Multiplying each side of the equation by $\cos \frac{m\pi z}{H}$, vertically integrating from $z = -H$ to $z = 0$, and appealing to orthogonality gives the coefficients a_m as

$$a_m = \sum_{n=1}^{\infty} \frac{2m\delta_s^2(-1)^n \sin m\pi\delta_s}{\pi(m^2\delta_s^2 - n^2)} b_n + \frac{2 \sin m\pi\delta_s}{m\pi\delta_s}. \quad (3.25)$$

The addition of a second set of unknown coefficients b_n requires a second boundary condition. A convenient matching condition would stipulate that the vertical velocity was continuous across $x = 0$. This shall be verified using the horizontal and vertical momentum equations ((3.7) and (3.9)) and the density equation. First the equation (3.7) is integrated from $x = -\epsilon$ to $x = \epsilon$, giving

$$\int_{-\epsilon}^{\epsilon} \left(\frac{\partial u}{\partial t} - fv + \frac{1}{\rho_o} \frac{\partial p}{\partial x} \right) dx = 0 \quad (3.26)$$

$$\frac{\partial u}{\partial t} 2\epsilon - 2fv\epsilon + \frac{1}{\rho_o} p|_{-\epsilon}^{\epsilon} = 0. \quad (3.27)$$

As before, the assumption of finite acceleration implies that p is continuous across $x = 0$. Also, since the derivative of a continuous function is itself continuous, $\partial p/\partial z$ is now continuous across $x = 0$. Now the vertical momentum equation and the density equation are written as

$$\frac{\partial w}{\partial t} = -\frac{1}{\rho_o} \frac{\partial p}{\partial z} - \frac{\rho g}{\rho_o} \quad (3.28)$$

$$\frac{\partial \rho}{\partial t} = \frac{\rho_o N^2}{g} w. \quad (3.29)$$

Now it is assumed that the vertical velocity w and the density ρ are periodic in time, just as u is, so that

$$-i\omega w = -\frac{1}{\rho_o} \frac{\partial p}{\partial z} - \frac{\rho g}{\rho_o} \quad (3.30)$$

$$-i\omega \rho = \frac{\rho_o N^2}{g} w. \quad (3.31)$$

Since it has been shown that $\partial p/\partial z$ is continuous across $x = 0$, equations (3.30) and (3.31) can be rearranged to show that both w and ρ are continuous across $x = 0$ as well. Hence it is valid to equate the vertical velocity field across the sill for the purposes of creating a second matching condition.

Using the expressions for u' as defined in equations (3.17) and (3.18) and the continuity equation to write the w' field on each side of the sill as

$$\begin{aligned} w'_{1n} &= i \frac{\omega}{N} a_n u_o \sin \frac{n\pi z}{H} \exp(ik_1 x - i\omega t) \\ w'_{2n} &= -i \frac{\omega}{N} b_n u_o \sin \frac{n\pi z}{d} \exp(ik_2 x - i\omega t) \end{aligned}$$

and then summing and equating them at the sill ($x = 0$), a second equation constraining the system is

$$\sum_{l=1}^{\infty} b_l \sin \frac{l\pi z}{d} = - \sum_{l=1}^{\infty} a_l \sin \frac{l\pi z}{H} \quad -d < z \leq 0, \quad (3.32)$$

where a_l and b_l have been non-dimensionalised by the barotropic amplitude u_o . Multiplying (3.32) by $\sin \frac{n\pi z}{d}$, vertically integrating from $z = -d$ to $z = 0$, and using orthogonality gives a solution for the coefficients b_n as

$$b_n = \sum_{l=1}^{\infty} \frac{2n(-1)^n \sin l\pi \delta_s}{\pi(n^2 - l^2 \delta_s^2)} a_l. \quad (3.33)$$

The expressions in (3.25) and (3.33) can be reduced to a single matrix equation by first rewriting using matrix notation and the Einstein summation convention, yielding

$$\begin{aligned} a_m &= A_{mn} b_n + C_m \\ b_n &= B_{nl} a_l, \end{aligned}$$

where

$$A_{mn} = \frac{2m\delta_s^2(-1)^n \sin m\pi\delta_s}{\pi(m^2\delta_s^2 - n^2)} \quad (3.34)$$

$$B_{nl} = \frac{2n(-1)^n \sin l\pi\delta_s}{\pi(n^2 - l^2\delta_s^2)} \quad (3.35)$$

$$C_m = \frac{2 \sin m\pi\delta_s}{m\pi\delta_s}. \quad (3.36)$$

Singularities appear in A_{mn} and B_{nl} where $n = m\delta_s$ and $n = l\delta_s$, respectively, so the matching conditions are re-integrated to solve for the singular indices, yielding $A_{m,m\delta_s} = \delta_s$ and $B_{l\delta_s,l} = -1$.

At this point a new parameter δ will be introduced where $\delta = (H - d)/H = 1 - \delta_s$. This new parameter is now the ratio of obstacle height (sometimes denoted by h_o) to total water depth, and has an equivalent meaning to that in other studies (e.g. St. Laurent et al. 2003), namely that a vanishing δ corresponds to flat topography. The matrices are now rewritten using the new parameter as

$$A_{mn} = \frac{2m(1 - \delta)^2(-1)^n \sin m\pi(1 - \delta)}{\pi(m^2(1 - \delta)^2 - n^2)} \quad (3.37)$$

$$B_{nl} = \frac{2n(-1)^n \sin l\pi(1 - \delta)}{\pi(n^2 - l^2(1 - \delta)^2)} \quad (3.38)$$

$$C_m = \frac{2 \sin m\pi(1 - \delta)}{m\pi(1 - \delta)}, \quad (3.39)$$

where $A_{m,m(1-\delta)} = 1 - \delta$ and $B_{m,m(1-\delta)} = -1$ to avoid singularities. Now the coefficients a_m are solved by combining the two matrix equations, giving

$$(\delta_{ml} - A_{mn}B_{nl})a_l = C_m \quad (3.40)$$

$$a_l = (\delta_{ml} - A_{mn}B_{nl})^{-1}C_m. \quad (3.41)$$

Equations (3.41) and (3.34) are solved numerically by truncating the infinite indices and including only the first 1200 modes. All numbers quoted in the S80 paper were those resulting from the choice of $u_o = -1$ m/s, or 1 m/s toward the deep-ocean off the shelf, although for some purposes the value of the barotropic velocity in this thesis will be moot as the results have been non-dimensionalised. Intuition might dictate that, for a very shallow

shelf, a_n would closely follow the S80 expression for a_n , given by (3.6), with b_n negligibly small or zero. As the shelf deepens, however, a_n should become smaller than the estimate of Stigebrandt while b_n should become larger, eventually growing as large as a_n .

First, the matching conditions at the sill should be verified. Figures 3.2 and 3.3 show the total U and W velocities, respectively, at the sill for both sides of the new model and, for comparison, the S80 model. Figure 3.2 displays a deep-side horizontal velocity which vanishes below the sill depth, matching the boundary condition and agreeing the S80 result, and which matches the shelf-side horizontal velocity above the sill depth, which is required by continuity. The velocity profile is different than that of the S80 model, but appears more realistic. Instead of a constant scaled velocity above the sill depth, there is a strong jet which forms at the sill depth and weakens with height above the sill. This is consistent with water which is most strongly affected by the sudden increase in depth coming off the shelf, an effect which is felt with decreasing intensity farther above from the sill. Figure 3.3 shows the other matched condition at the sill, which is the vertical velocity. The velocities are matched above the sill depth, with the deep-side vertical velocity left unmatched below the sill depth. This also reinforces the sill-depth jet concept: the strongest negative vertical (ie. downward) velocity occurs at sill-depth, where the isopycnals dip down into the deep side of the fjord off the shelf. With the boundary conditions apparently satisfied, the properties of the solution can be further investigated.

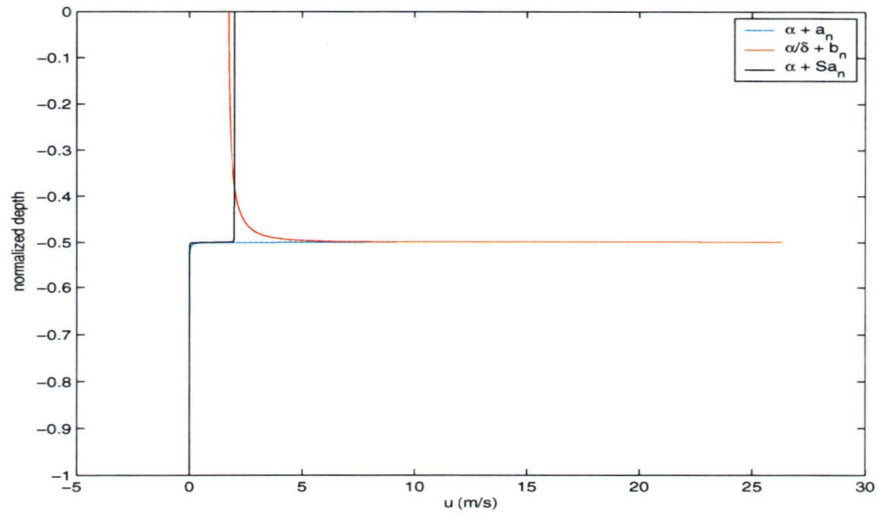


Figure 3.2: u at sill on the deep-side (blue), shelf-side (red) and in S80 (black). $\delta = 0.5$

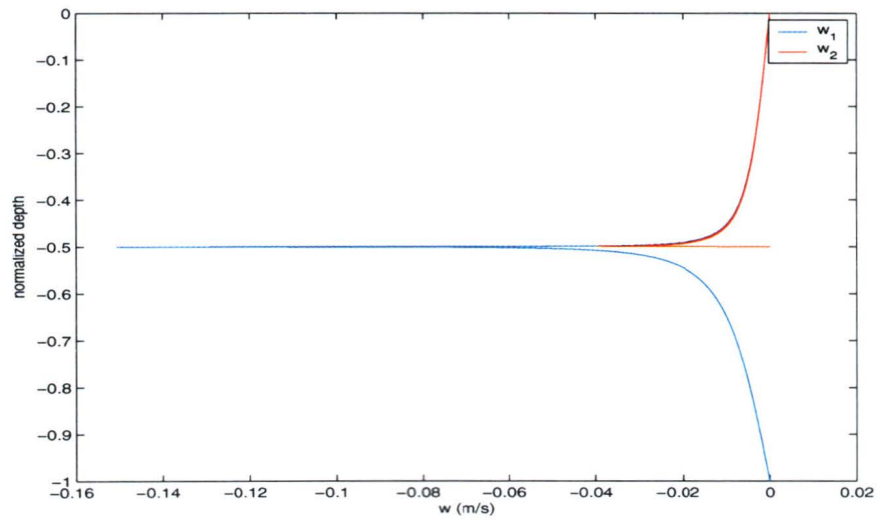


Figure 3.3: w at sill on the deep-side (blue) and the shelf-side (red). $\delta = 0.5$

The wave amplitudes of the first 20 modes for nine incremental values of δ are shown in figure 3.4. Recall that a small value of delta represents a step of small height. Figure 3.4 shows that, for all shelf depths, the new deep-ocean wave-amplitudes are similar in both S80 and the present formulation. However, the shelf-side waves are stronger for a shallow sill than for a deep sill. The shelf waves appear to be larger than the deep waves for a shallow shelf, and they decrease faster than do the deep waves with decreasing δ such that they have comparable amplitudes for shelves at half the water depth and are smaller than the deep waves for very deep shelves. This may not have a direct influence on the application of S80 in SS92, but it would be more useful to check that the energy flux of the neglected waves is small compared to the deep-side waves.

3.1.3 Energy flux

The energy flux of internal waves in a stratified fluid is the averaged product of the perturbation pressure and velocity, or

$$\mathbf{F} = \overline{p' \mathbf{u}'}. \quad (3.42)$$

The alternate form of the energy flux, which is the product of the group velocity and wave energy, yields the same result as equation (3.42). The perturbation pressure is found from equations (3.7) and (3.8), after making the assumption that all variables are periodic in space and time. Substituting exponential forms into each variable, the equations reduce to

$$-i\omega u - fv = -\frac{1}{\rho_o} ikp \quad (3.43)$$

$$-i\omega v + fu = 0, \quad (3.44)$$

where $\partial p / \partial y$ has been set to zero to ensure that waves are only propagating in the x direction. Re-arranging equation (3.44) to solve for v and substituting it into equation (3.43) yields

$$\omega u \left(\frac{\omega^2 - f^2}{\omega^2} \right) = \frac{1}{\rho_o} kp. \quad (3.45)$$

Now an expression for pressure can be found on the left and right sides of the step by substituting equations (3.17) and (3.18), respectively, into equation (3.45). Then, using equation (3.42), the depth-integrated horizontal energy flux on each side of the sill is

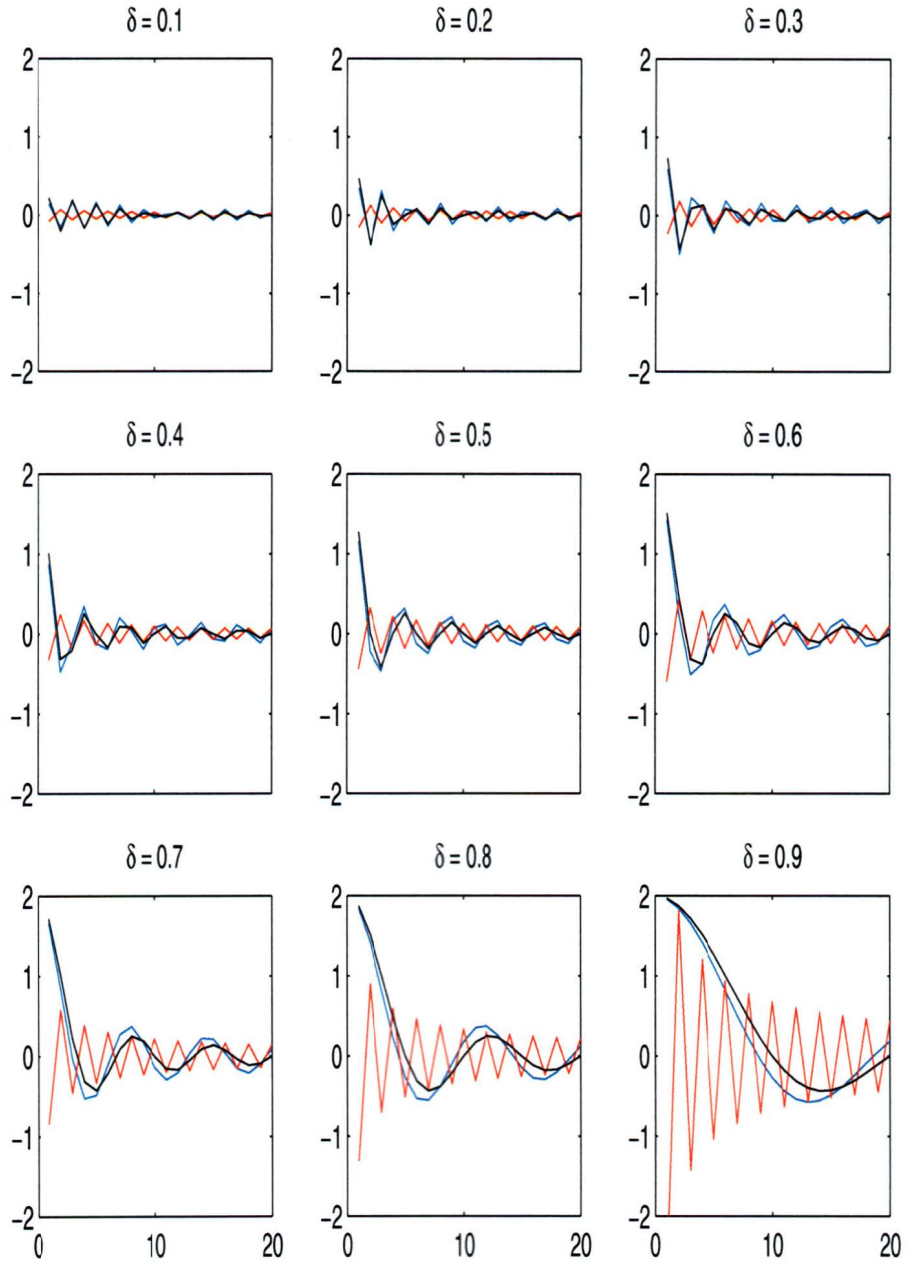


Figure 3.4: Values of a_n (blue), b_n (red) and Stigebrandt's a_n (black).

$$F_1 = \sum_{n=1}^{\infty} \frac{1}{4} \rho_o H \frac{\omega}{k_1} \left(\frac{\omega^2 - f^2}{\omega^2} \right) u_o^2 a_n^2 \quad (3.46)$$

$$F_2 = \sum_{n=1}^{\infty} \frac{1}{4} \rho_o d \frac{\omega}{k_2} \left(\frac{\omega^2 - f^2}{\omega^2} \right) u_o^2 b_n^2 \quad (3.47)$$

since the average of $\cos^2 mz \cos^2(kx - \omega t)$ over a horizontal and vertical wavelength is $1/4$. Taking the constant factors outside each sum, the energy fluxes can be rewritten as

$$F_1 = -\frac{1}{2} F_o \sum_{n=1}^{\infty} \frac{a_n^2}{n} \quad (3.48)$$

$$F_2 = \frac{1}{2} F_o (1 - \delta)^2 \sum_{n=1}^{\infty} \frac{b_n^2}{n}, \quad (3.49)$$

where

$$F_o = \frac{1}{2\pi} \rho \frac{((N^2 - \omega^2)(\omega^2 - f^2))^{1/2}}{\omega} u_o^2 H^2. \quad (3.50)$$

The negative sign of F_1 implies propagation towards the negative x -axis, or towards the open ocean. First it should be confirmed that the energy flux generated on both sides of the step vanishes as the step height goes to zero and also that the energy flux is equal on both sides for an infinitesimally small step, since linear theory suggests that, if small, it should not matter if the step increases or decreases in height. The upper panel of Figure 3.5 shows the non-dimensional energy flux generated on the deep side (blue) and the shallow side (red) of the step as compared with δ , recalling that a value nearing zero represents a very small step. Both energy fluxes do converge to zero with decreasing step height. More importantly, however, is the bottom panel which shows the ratio of the energy flux generated on the shallow side to that generated on the deep side. It confirms that the ratio of the energy fluxes goes to one as the step height approaches zero, showing that the energy flux is equal on both sides of a step of infinitesimal height. The kink that is seen in the middle of the curve (in the area of $\delta \approx 10^{-3}$ is a numerical shortcoming; it is necessary to have at least $O(\delta^{-1})$ modes for any small δ to accurately calculate its energy flux. While increasing the number of modes does delay the onset of the kink slightly, resources did not exist to accurately calculate the fluxes below $\delta < 10^{-4}$. While the numerics were inadequate in this instance, it can be shown that for modes with $N < O(\delta^{-1})$,

$$\lim_{\delta \rightarrow 0} a_n = -\lim_{\delta \rightarrow 0} b_n = -(-1)^n \delta, \quad (3.51)$$

thus analytically confirming that the energy flux ratio is unity for small δ (St. Laurent et al. 2003).

Now the step model can be compared to that of Stigebrandt (1980). The upper panel of Figure 3.6 shows the energy fluxes of the oceanic internal waves (blue), the shelf internal waves (red), and S80 oceanic internal waves (black) for all values of δ , the ratio of step height to seafloor depth. The lower panel shows the oceanic, shelfside, and total energy flux as a fraction of S80 oceanic internal-wave energy-flux. For a shallow shelf of $\delta = 0.9$, the energy flux of the oceanic internal waves is 96.1% of those in the S80 step model while the shelfside energy flux is only 1.4% of S80 oceanic energy flux. Certainly, S80 agrees well with the new model for this very shallow shelf. A slight departure from S80 can be seen if the water depth over the shelf is one half of that in the deep ocean ($\delta = 0.5$). The oceanic energy flux of the step model decreases to 87.5% of S80 energy flux, while the shelfside energy flux increases to 4.6% of S80. For a deep shelf of $\delta = 0.1$, however, the oceanic and shelfside energy fluxes are 66.8% and 12.0% of S80, respectively. An even deeper shelf of $\delta = 0.05$ produces percentages of 60.1% and 14.2%, respectively. Clearly the energy flux of the shelfside internal waves is not negligible for deep shelves, and the oceanic energy fluxes are increasingly overestimated by S80 as the shelf deepens. This illustrates a problem with the usage of the S80 step model in the Sjöberg and Stigebrandt energy flux model, which is that the SS92 model contains steps with very large depth ratios ($\delta \rightarrow 0$). The S80 model both neglects step-side internal waves which carry significant energy flux and overestimates the energy flux radiated in the deep-side internal waves.

3.1.4 Comparison with linear theory

Bell (1975) found the energy flux generated from weak topography analytically using the topographic spectrum, and Llewellyn Smith and Young (2002) extended that theory for a finite ocean. An analytic function which can represent a topographic step is $h(x) = \pi^{-1} h_o \tan^{-1}(x/b)$, where h_o is the obstacle height, or $H - d$. As $b \rightarrow 0$, the arctan slope steepens to a shelf as shown in Figure 3.7. Using the theory of Llewellyn Smith and Young (2002), the energy flux from the arctan slope is

$$F_{\text{slope}} = F_o \delta^2 \sum_{n=1}^{\infty} n^{-1} \exp^{-\frac{4n\delta}{\epsilon(2-\delta)}} = -F_o \delta^2 \ln \left(1 - \exp^{-\frac{4\delta}{\epsilon(2-\delta)}} \right), \quad (3.52)$$

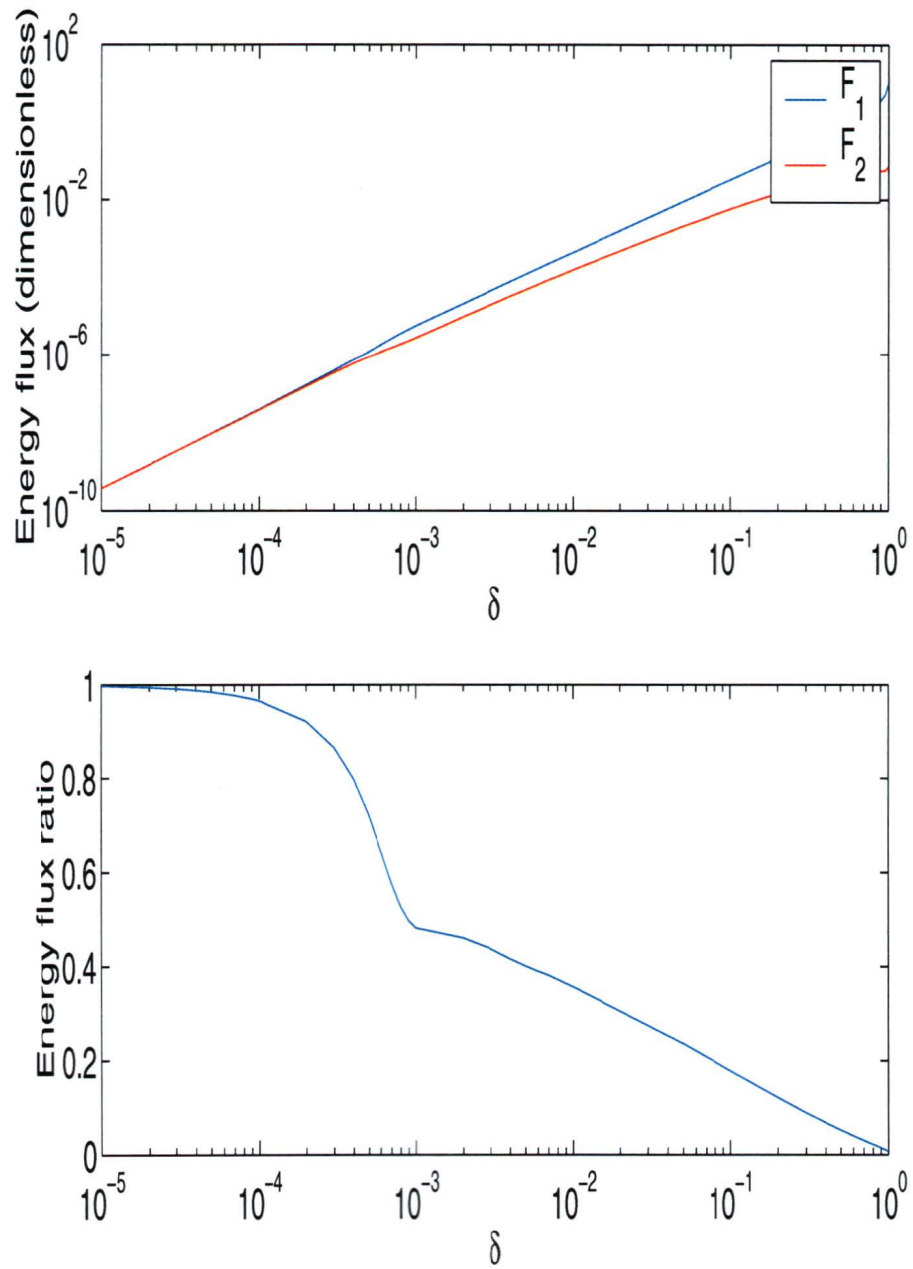


Figure 3.5: Upper: Horizontal energy fluxes F_1 (blue) and F_2 (red). Lower: Energy flux ratio of F_2 to F_1

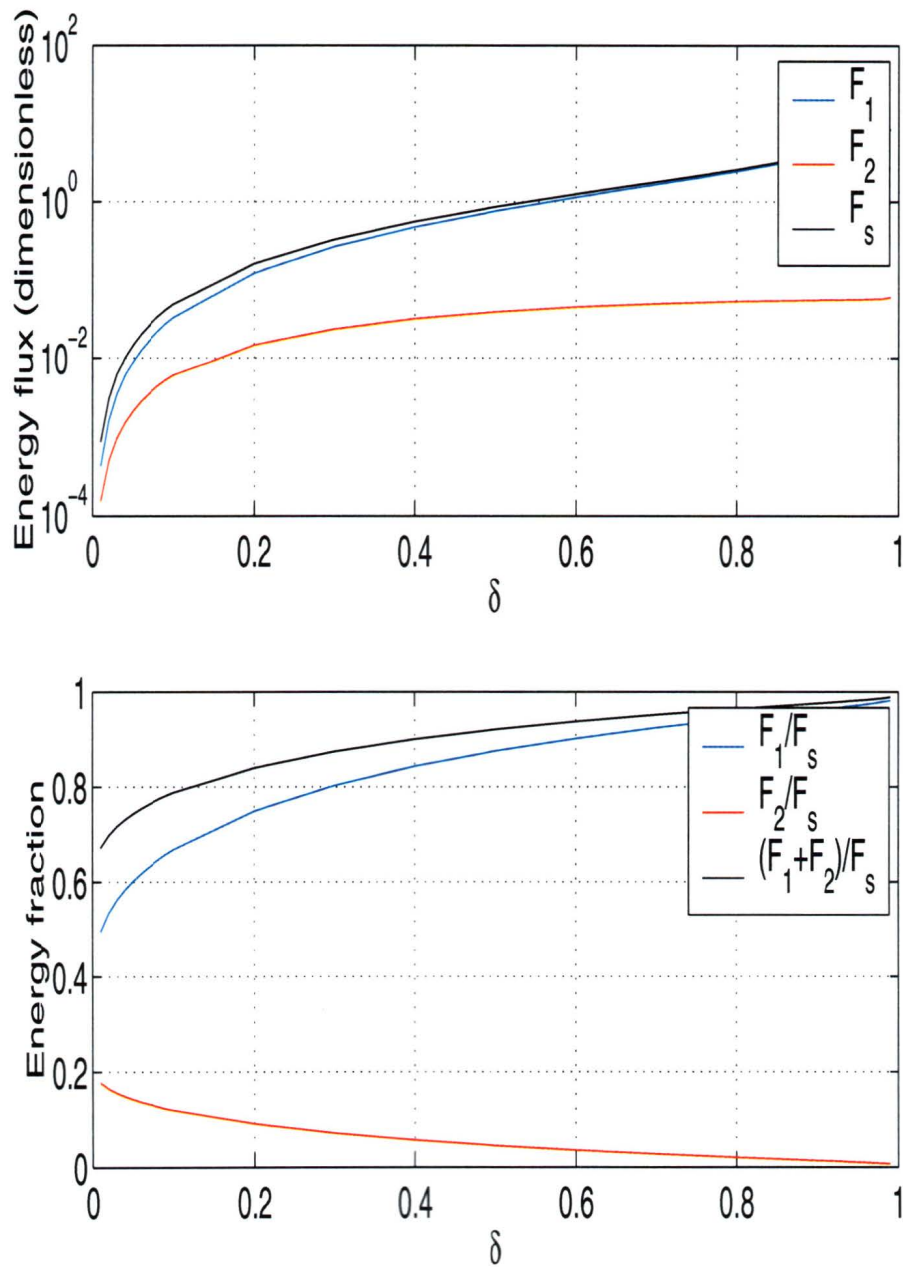


Figure 3.6: Upper: Horizontal energy flux associated with a_n (blue), b_n (red) and Stigebrandt's a_n (black). Lower: energy flux ratios of F_1 to F_{S80} (blue), F_2 to F_{S80} (red), and $F_1 + F_2$ to F_{S80} (black)

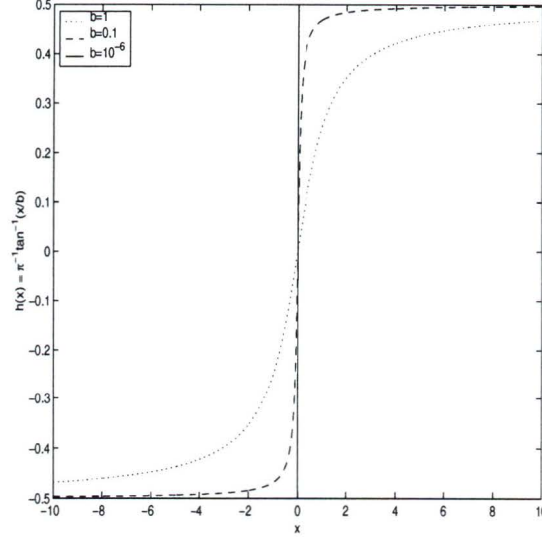


Figure 3.7: $h(x) = \pi^{-1}h_o \tan^{-1}(x/b)$, where $b = 1, 0.1$, and 10^{-6} , respectively

where the steepness parameter ϵ is given by

$$\epsilon = \alpha^{-1} \pi^{-1} \frac{h_o}{b}. \quad (3.53)$$

Again, $b \rightarrow 0$ implies $\epsilon \rightarrow \infty$, which is the steepness of a step. In the limits of $\delta \ll 1$ and $\delta/\epsilon \ll 1$, the energy flux is approximated by

$$F_{\text{slope}} \simeq F_o \delta^2 \ln \left(\frac{1}{2} \epsilon / \delta \right). \quad (3.54)$$

Balmforth et al. (2002) determine the increase in energy flux for certain topography when $\epsilon = 1$ as opposed to the weak topography limit. For instance, they report a 56% increase in the energy flux generated by sinusoidal topography if $\epsilon = 1$ as opposed to $\epsilon \ll 1$. To be consistent, $\epsilon = 1$ will be substituted into equation (3.54) and the total energy flux from the step (equation (3.48) plus equation (3.49)) will be compared to the flux from the arctan slope to determine if there is any additional increase in energy flux when ϵ is further increased from 1 to ∞ . The ratio is shown in Figure 3.8. The ratio of the energy fluxes generated from the step and from the arctan slope goes to one for vanishing δ , indicating that there is no additional increase in energy flux as the steepness is increases from $\epsilon = 1$ to $\epsilon \rightarrow \infty$. This ratio quickly increases for increasing δ , however. At $\delta = 10^{-3}$ the step shows a 30% enhancement in energy flux over the arctan slope, and greater than a 400%

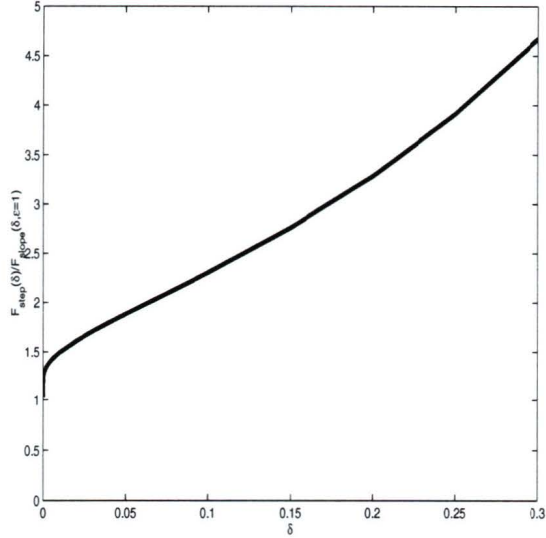


Figure 3.8: Ratio of total energy flux from step to energy flux from arctan slope ($\epsilon = 1$)

enhancement for $\delta > 0.3$.

3.2 Knife Edge Ridge

The step topography is a simple supercritical topography which has oceanographic relevance as it can be related to continental slopes. The delta-function, or “knife-edge”, ridge is another, as it can serve as a first approximation for many mid-ocean ridges such as the Hawaiian Ridge. With many recent numerical (Egbert and Ray 2000, Kang et al. 2000, Merrifield et al. 2001) and observational (Ray and Mitchum 1997) studies devoted to determining the amount of tidal energy dissipation at the Hawaiian Ridge and others, it would be useful to know if the properties of this simple approximation were similar to those of the more complex, realistic topography. Using the techniques of the previous section, the internal tides generated by a delta-function ridge can now be evaluated. Since the water depth is the same on both sides of the ridge, the barotropic current speed is the same on both sides as well, and it will again be denoted it as $u_o \cos(\omega t)$. Using the same non-dimensional coefficients as in the step formulation, the horizontal velocity of the n th mode on left and right side, respectively, is

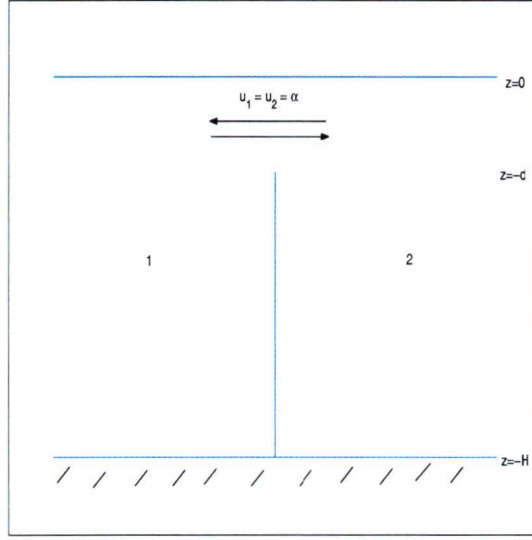


Figure 3.9: The knife-edge topographic ridge

$$u'_{1n} = a_n u_o \cos \frac{n\pi z}{H} \exp(ikx - i\omega t) \quad (3.55)$$

$$u'_{2n} = b_n u_o \cos \frac{n\pi z}{H} \exp(-ikx - i\omega t), \quad (3.56)$$

where the dispersion relation for the waves is

$$\omega = -\frac{kNH}{n\pi}. \quad (3.57)$$

Summing the barotropic and baroclinic currents on each side of the ridge and then matching the total currents at the ridge, or at $x = 0$, yields

$$\begin{aligned} 1 + \sum_{n=1}^{\infty} a_n \cos \frac{n\pi z}{H} &= 1 + \sum_{n=1}^{\infty} b_n \cos \frac{n\pi z}{H} & -d < z \leq 0 \\ &= 0 & -H \leq z \leq -d, \end{aligned}$$

or

$$\sum_{n=1}^{\infty} a_n \cos \frac{n\pi z}{H} = \sum_{n=1}^{\infty} b_n \cos \frac{n\pi z}{H} \quad -d < z \leq 0 \quad (3.58)$$

$$= -1 \quad -H \leq z \leq -d. \quad (3.59)$$

The lower equation specifies no normal flow through the left side of the sill. Of course, the current below the sill must also be zero at $x = 0$ on the right side, so another set of equations is

$$\sum_{n=1}^{\infty} b_n \cos \frac{n\pi z}{H} = \sum_{n=1}^{\infty} a_n \cos \frac{n\pi z}{H} \quad -d < z \leq 0 \quad (3.60)$$

$$= -1 \quad -H \leq z \leq -d. \quad (3.61)$$

These can be combined so that, over the entire domain,

$$\sum_{n=1}^{\infty} a_n \cos \frac{n\pi z}{H} = \sum_{n=1}^{\infty} b_n \cos \frac{n\pi z}{H} \quad -H \leq z \leq 0. \quad (3.62)$$

Multiplying this equation by $\cos \frac{m\pi z}{H}$, integrating z from $-H$ to 0 , and using the orthogonality of cosines, the result $a_m = b_m$ is found. The topographical symmetry might have suggested this as a possible result from the outset.

Since the horizontal velocity is unmatched above the sill, a boundary condition must be set over that region of the domain. In this region the vertical velocity is matched on both sides of the sill. The vertical velocity on each side of the sill, from substituting (3.55) and (3.56) into (3.10), is

$$w'_{1n} = i \frac{\omega}{N} a_n u_o \sin \frac{n\pi z}{H} \exp(ikx - i\omega t) \quad (3.63)$$

$$w'_{2n} = -i \frac{\omega}{N} b_n u_o \sin \frac{n\pi z}{H} \exp(-ikx - i\omega t). \quad (3.64)$$

Equating (3.63) and (3.64) over $-d < z \leq 0$, and recalling that $a_n = b_n$, the boundary condition above the sill is set with the expression

$$\sum_{n=1}^{\infty} a_n \sin \frac{n\pi z}{H} = 0 \quad -d < z \leq 0. \quad (3.65)$$

Now the complete boundary condition can be written at the sill over the entire water column as

$$\sum_{n=1}^{\infty} a_n \sin \frac{n\pi z}{H} = 0 \quad -d < z \leq 0 \quad (3.66)$$

$$\sum_{n=1}^{\infty} a_n \cos \frac{n\pi z}{H} = -1 \quad -H \leq z < -d. \quad (3.67)$$

The coefficients a_n must be extracted by expanding equations (3.66) and (3.67) through multiplication by a set of orthogonal functions. While cosines were chosen for the step problem, it is true that any set of orthogonal functions may be used. Cosines will again be employed to expand the sill problem, though care has been taken to confirm that expanding by sines yields the same answer.

Multiplying the sum of equations (3.66) and (3.67) by $\cos \frac{m\pi z}{H}$ and vertically integrating gives the coefficients a_n as

$$\begin{aligned} & \sum_{n=1}^{\infty} a_n \left(\int_{-H}^{-d} \cos \frac{n\pi z}{H} \cos \frac{m\pi z}{H} dz + \int_{-d}^0 \sin \frac{n\pi z}{H} \cos \frac{m\pi z}{H} dz \right) \\ &= - \int_{-H}^{-d} \cos \frac{m\pi z}{H} dz, \end{aligned} \quad (3.68)$$

which can be written as

$$A_{mn} a_n = C_m, \quad (3.69)$$

where

$$\begin{aligned} A_{mn} &= \frac{n \sin n\pi(1-\delta) \cos m\pi(1-\delta) - m \cos n\pi(1-\delta) \sin m\pi(1-\delta)}{(m^2 - n^2)} \\ &+ \frac{n - n \cos n\pi(1-\delta) \cos m\pi(1-\delta) - m \sin n\pi(1-\delta) \sin m\pi(1-\delta)}{(m^2 - n^2)} \end{aligned} \quad (3.70)$$

and

$$C_m = \frac{\sin m\pi(1-\delta)}{m}. \quad (3.71)$$

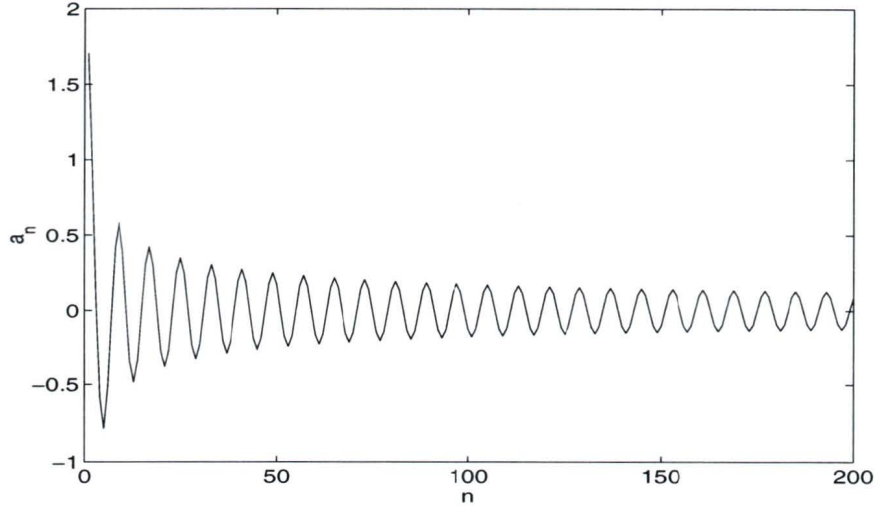


Figure 3.10: Coefficient a_n values for $n = 1$ through 200. $\delta = 0.75$

A_{mn} is singular when $m = n$, so those elements are replaced with those found by re-evaluating the integrals on the left-hand side of equation (3.68) after setting $m = n$, giving

$$A_{nn} = \frac{n\pi\delta - \sin n\pi(1 - \delta) \cos n\pi(1 - \delta) - \sin^2 n\pi(1 - \delta)}{2n}. \quad (3.72)$$

Also, since the index m runs from 0 to ∞ , C_m is singular at $m = 0$. This element is replaced by setting $m = 0$ in the integral on the right-hand side of equation (3.68), yielding

$$C_0 = -\pi\delta. \quad (3.73)$$

Equation (3.69) is inverted to solve for a_n after truncating A_{mn} at 1200 modes. Figure 3.10 confirms that the coefficients a_n fall off with increasing modenummer, while Figures 3.11 and 3.12 show that the prescribed boundary conditions, namely no normal flow through the sill and no vertical flow above the sill, are satisfied.

3.2.1 Energy flux

The energy flux generated at the knife edge ridge can be found from equation 3.42, where the perturbation pressure is calculated by substituting equations 3.55 and 3.56 into equation 3.7. The resulting energy fluxes are then

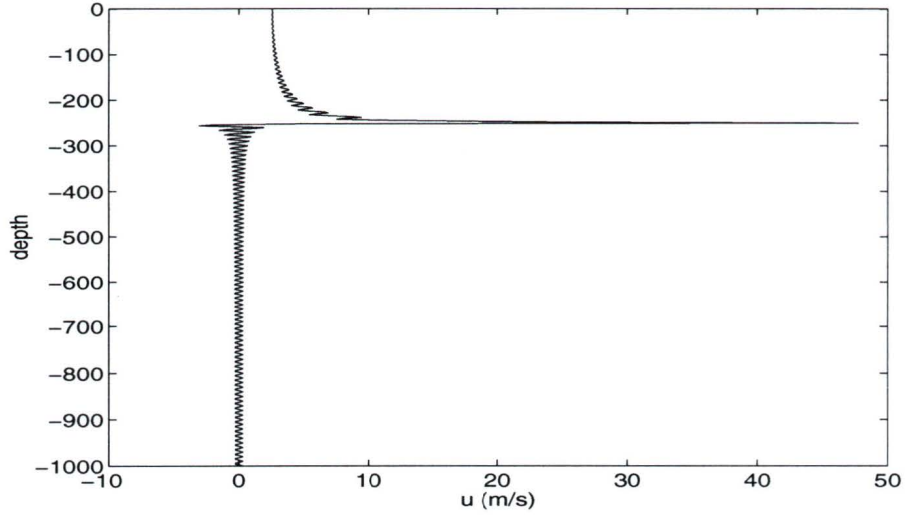


Figure 3.11: Total horizontal flow $u = u_o + \sum_{n=1}^{1200} a_n u_o \cos \frac{n\pi z}{H}$, $u_o = 1 \text{ m/s}$, $\delta = 0.75$

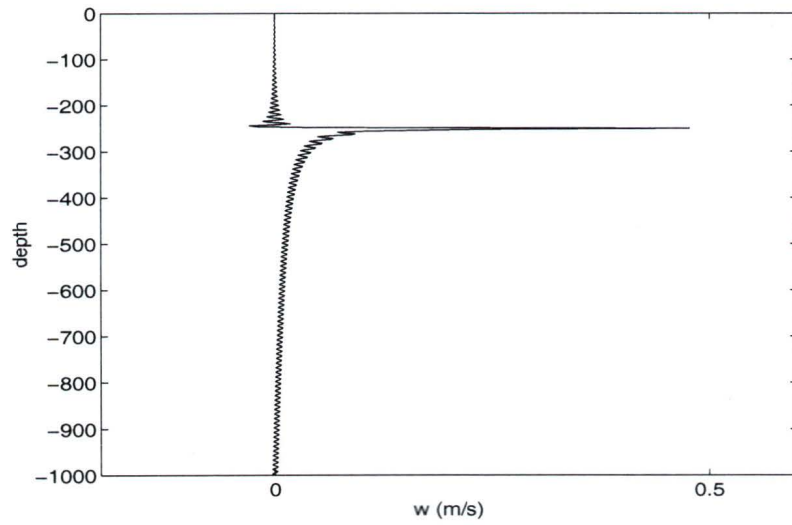


Figure 3.12: Total vertical flow $w = \sum_{n=1}^{1200} a_n u_o \frac{\omega}{N} \sin \frac{n\pi z}{H}$, $u_o = 1 \text{ m/s}$, $\delta = 0.75$

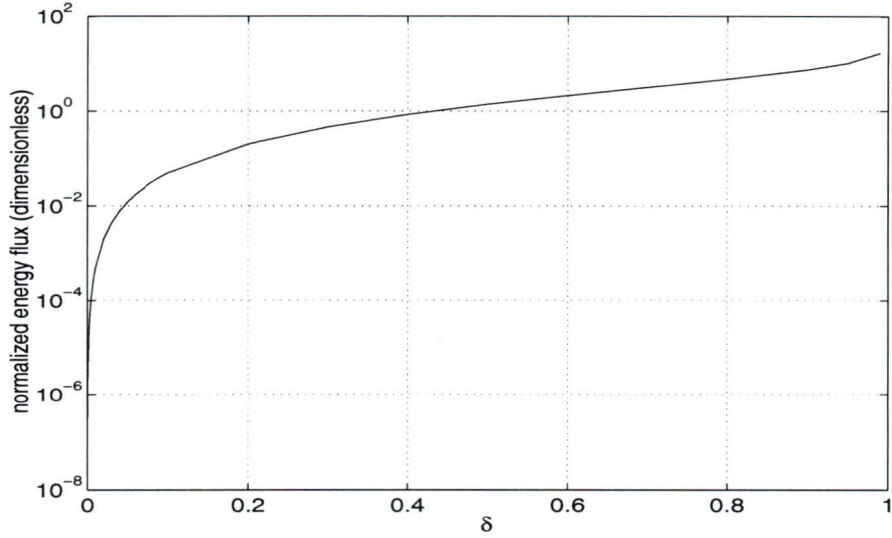


Figure 3.13: Depth-averaged normalized horizontal energy flux.

$$F_1 = -\frac{1}{2}F_o \sum_{n=1}^{\infty} \frac{a_n^2}{n} \quad (3.74)$$

$$F_2 = \frac{1}{2}F_o \sum_{n=1}^{\infty} \frac{a_n^2}{n}, \quad (3.75)$$

where $F_o = \frac{1}{2\pi}\rho \frac{((N^2-\omega^2)(\omega^2-f^2))^{1/2}}{\omega} u_o^2 H^2$. Again, the negative sign in equation 3.74 denotes a flux in the negative x direction. The energy flux generated on each side of the knife edge ridge is equal, so that the total generated energy flux is $F_o \sum_{n=1}^{\infty} \frac{a_n^2}{n}$. The energy flux, normalized by F_o , is plotted against δ in Figure 3.13. The energy flux drops off sharply for small sill heights, or for $\delta \rightarrow 0$.

3.2.2 Comparison with linear theory

In section 3.1.4, the energy flux generated by an arctan slope was calculated using linear theory and then compared to the energy flux generated by a step. Here a topographic feature is sought for comparison with a knife-edge ridge. The ‘‘Witch of Agnesi’’ is a topographic ridge which has been studied by Bell (1975) in an infinite ocean, and again by Llewellyn Smith and Young (2002) in a finite ocean. The witch profile is described by

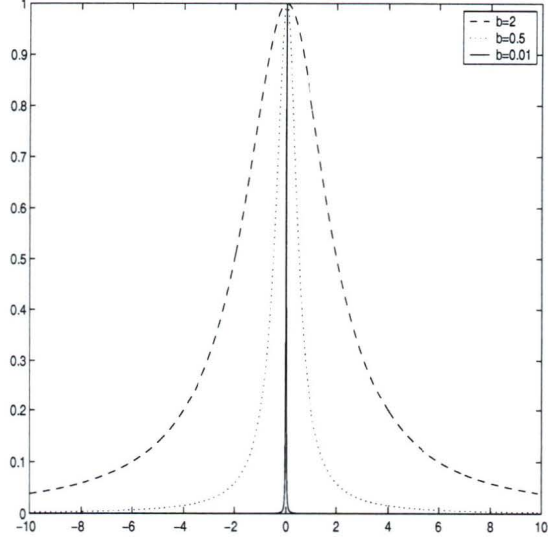


Figure 3.14: The “Witch of Agnesi” profile. $b = 2$, $b = 0.5$, and $b = 0.01$ from the outer to inner curves, respectively.

$h(x) = h_o(1 + (x^2/b^2))^{-1}$, and is pictured in Figure 3.14. Using the finite-ocean theory of Llewellyn Smith and Young (2002), the energy flux generated by the witch is expressed as

$$F_{witch} = F_o \frac{\pi^2}{4} \sum_{n=1}^{\infty} n c^2 e^{-nc} = F_o \frac{\pi^2}{4} \frac{c^2 e^{-c}}{(1 - e^{-c})^2}, \quad (3.76)$$

where $c = (3^{3/2}\pi/4)(\delta/\epsilon)$, and the steepness parameter is given by

$$\epsilon = \left(\frac{N^2 - \omega^2}{\omega^2 - f^2} \right)^{1/2} \left(\frac{3^{3/2}}{8} \right) \frac{h_o}{b}. \quad (3.77)$$

Using equation (3.76) with $\epsilon = 1$, the ratio of the energy flux generated from the knife-edge ridge to that from the witch of critical steepness is calculated as a function of δ and shown in Figure 3.15. In the limit of $\delta \ll 1$, the knife-edge ridge produces exactly twice the energy flux generated by the Witch of Agnesi, and the ratio increases with increasing δ . For $\delta > 0.6$, the energy flux generated by the knife-edge ridge exceeds that from the witch by a factor of 4.

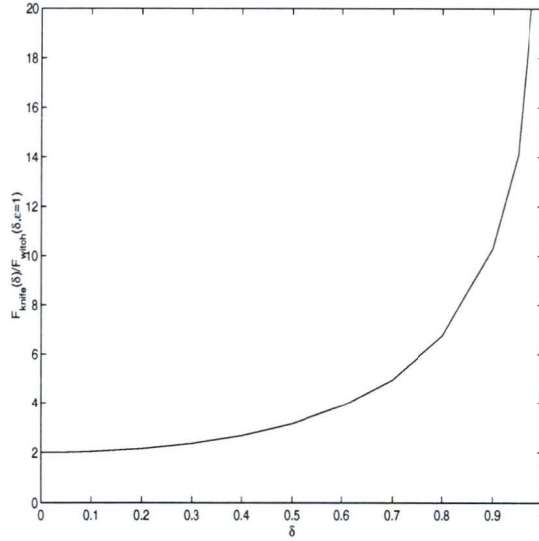


Figure 3.15: Ratio of energy flux from a knife-edge ridge to that from a “Witch of Agnesi” ridge with $\epsilon = 1$.

3.2.3 Comparison with modeled energy fluxes for realistic sills

By choosing the proper values with which to calculate F_o , the knife edge model can now be used to determine the energy flux of the internal tide from a ridge using realistic ocean depths and current speeds. The Hawaiian Ridge, which rises to a depth of 1000m from the mean seafloor depth of 4000m is believed to be a major generation site for internal tides, with a radiated energy flux estimated between 5.4GW (Kang et al. 2000) and 20GW (Egbert and Ray 2000). Merrifield et al. (2001) model the total radiated energy flux away from the ridge and find it to be 9GW using realistic M_2 tidal forcing and bathymetry. Ray and Mitchum (1997) estimate 15GW of radiated energy from TOPEX/Poseidon altimeter data. Equations (3.74) and (3.75) are used to calculate the radiated energy flux away from both sides of the sill. From Figure 3.13, the knife edge model gives a total dimensionless energy flux away from the sill of 3.8 when $\delta = 0.25$. To calculate F_o , a mean density of 1025kg/m^3 , GM upper-ocean stratification ($N = 0.00524\text{ s}^{-1}$), and a mean barotropic current speed of $u_o = 1.4\text{cm/s}$ as calculated from a tidal model of the Hawaiian region are used. The resultant energy flux is multiplied by the approximate length of the ridge (2000km) to give an estimate of the total radiated energy flux of 20 GW. This is in good agreement with the results of Egbert and Ray (2000), even though this estimate uses a constant stratification and models the ridge with a single value of δ . Despite its simplicity, the results are plausible.

Chapter 4

Discussion

Acoustic Doppler current profilers can be used to effectively measure Reynolds stresses, either by the direct multiplication of velocity fluctuations, or by using the beam variance method of Lohrmann et al. (1990). The Reynolds stresses from a Janus and a Cyclops ADCP have been expressed as functions of the beam variances and the four remaining unknown components of the stress tensor. In situations where the instruments are perfectly aligned with the Cartesian vertical axis, the Janus ADCP is able to exactly represent the Reynolds stresses in terms of only the known beam variances, whereas the Cyclops ADCP can resolve the Reynolds stresses without bias only in a region of horizontally isotropic turbulence. The Cyclops ADCP, however, can measure the turbulent kinetic energy and the anisotropy ratio when there is no tilt, due to the fact that the vertical beam gives a direct measure of the vertical velocity. In the presence of tilt, both the Janus and Cyclops give estimates of Reynolds stress which contain unknown terms from the stress tensor. Their effect on the Reynolds stress is reduced when they are multiplied by a tilt angle. All undetermined terms are multiplied by tilt angles in the Janus configuration, but a single term in each stress expression for the Cyclops ADCP ($\overline{u'v'}$ in the $-\overline{u'w'}$ expression and $(\overline{v'^2} - \overline{w'^2})$ in the $-\overline{v'w'}$ expression) was not multiplied by a tilt, and hence could act as a large bias to the stress. For each of the four undetermined terms, the ratio of Cyclops coefficient to Janus coefficient was calculated as a function of both tilt angles. This was done for both stresses. In each stress, there was at least one undetermined term which had a much larger coefficient in the Cyclops configuration than in the Janus configuration. The presence of these larger biases in the Cyclops ADCP is concerning. When the turbulent kinetic energy and anisotropy ratios are calculated, however, the Cyclops yields expressions which are invariant to first-order tilt angles whereas the Janus cannot resolve the kinetic energy even in a zero-tilt environment. The invariant expressions of the Cyclops are most encouraging, given the difficulty in obtaining zero-tilt deployments in most conditions.

Other ADCP beam configurations have been explored. A three-beam system, which has three oblique beams azimuthally spaced at 120° , and a five-beam system, which is essentially a Janus ADCP with a fifth beam which points vertically, have been investigated to determine if they can yield the same data products as the Janus and Cyclops configurations. The three-

beam ADCP has significant bias terms in both stress estimates and they cannot be reduced as was done in the case of the Janus ADCP because only three independent variables can be resolved. Conversely, the five-beam ADCP combines the strengths of both the Janus and Cyclops configurations in that it can resolve the Reynolds stresses using the oblique beams which point in perpendicular planes while at the same time using the vertical beam to measure the vertical velocity and hence calculate the turbulent kinetic energy and the anisotropy ratio. The TKE and anisotropy vary only by a known correction term when tilt is introduced.

In addition to a mathematical treatment of the differences between the Janus and Cyclops configurations, data which were recorded by each instrument at the same location and time were analyzed to show how the different formulations of Reynolds stress for each instrument affect actual stress measurements. Seven days of data were collected from both instruments in Sansum Narrows, BC, in August 2000. Two days in the first half of the record were analyzed because of the relatively constant values of pitch and roll experienced by each ADCP during that time. It was found that the terms which were most important to the stress estimates were the $\overline{u'^2}$ and $\overline{v'^2}$ terms, with the $\overline{w'^2}$ and $\overline{u'v'}$ terms having less significance. This was particularly noticeable in the Janus case, where the stresses had significant biases from $(\overline{u'^2} - \overline{w'^2})$ and $(\overline{v'^2} - \overline{w'^2})$ terms respectively, but after the $\overline{u'^2}$ and $\overline{v'^2}$ terms were removed the biases were much smaller. In future, a rigid deployment of the instruments, as suggested by Lu and Lueck (1999a), would eliminate any bias arising from the small variations in time in the tilt angles experienced by the gimbaled assemblies used in this study.

The generation of internal tides at abrupt topography has also been addressed. The tidal generation from a single step has been solved as a function of δ , the ratio of step height to water depth. This solution is compared against that of Stigebrandt (1980), who made the assumption that shelf-side waves are negligible for shallow shelves (i.e. $\delta \rightarrow 1$). This assumption has been validated; for shallow shelves, the shelf-side waves make a negligible contribution to the total energy flux. However, this balance changes as the shelf height decreases such that as the step vanishes (i.e. $\delta \rightarrow 0$), the energy flux generated at each side of the step is equal. Hence any formulation of a step problem with small step heights cannot use the Stigebrandt (1980) assumption that the shelf waves are negligible compared to the deep waves. While linear theory cannot yield the energy flux for a supercritical feature such as a step, it can do so for an arctan slope of critical steepness. The ratio of the energy flux from that of the step to that of the slope nears unity for a vanishing step, but increases very rapidly to 1.3 at $\delta = 10^{-3}$. For $\delta > 0.3$ the energy flux from the step exceeds that

predicted by the linear theory by more than a factor of four.

A second abrupt topography which has been examined has been a knife-edge ridge. Using the same matrix inversion technique as used for the step, the modal coefficients for the knife-edge ridge were found and used to determine the energy flux generated from the feature. The flux, which is symmetric on both sides of the ridge is compared to the estimate using linear theory of energy flux from a “Witch of Agnesi” ridge, which steepens to a knife-edge ridge in the limit of infinite topographic steepness. In the limit of $\delta \rightarrow 0$, or vanishing topographic height, the energy flux from the knife-edge ridge is twice that from the witch. The amount by which the energy flux from the knife-edge exceeds that from the witch increases with topographic height; for $\delta > 0.6$ the knife-edge flux exceeds the flux from the witch by more than a factor of four. The knife-edge model has also been used to estimate the energy flux from an actual oceanic ridge; the Hawaiian Ridge. Using parameter values specific to the region and the topography, a generated energy flux of 20GW can be estimated from the Hawaiian Ridge. This result agrees well with similar satellite studies of the area by Egbert and Ray (2000), and while it may be seen as fortuitous considering the assumption of constant stratification and the dependence on the choice of δ which varies along the actual ridge, it is nonetheless encouraging that the estimate is of the same order as other, more detailed models and observational studies.

Future work in this area would begin with the extension of the step and knife-edge models to include variable stratification. In addition to providing more realistic ray paths for the generated waves, it would give more accurate energy flux results for ocean ridges such as the Hawaiian Ridge. In such locations, much of the stratification occurs above the height of the ridge and hence to impose a constant stratification in the model has the effect of elongating the upper water column which is highly stratified and compressing the lower, weakly stratified portion of the water column. As a result of this modification of the vertical co-ordinate, a given value of δ in the model with constant stratification will correspond to a higher value of δ if variable stratification is used.

Bibliography

- N.J. Balmforth, G.R. Ierley, and W.R. Young. Tidal conversion by nearly critical topography. *Journal of Physical Oceanography*, 32:2900–2914, 2002.
- T.H. Bell. Lee waves in stratified flows with simple harmonic time dependence. *Journal of Fluid Mechanics*, 67:705–722, 1975.
- P.D. Craig. Solutions for internal tidal generation over coastal topography. *Journal of Marine Research*, 45:83–105, 1987.
- G.D. Egbert and R.D. Ray. Significant dissipation of tidal energy in the deep ocean inferred from satellite altimeter data. *Nature*, 405:775–778, 2000.
- A.E. Gill. *Atmosphere-Ocean Dynamics*. Academic Press, 1982.
- R.L. Gordon. *Acoustic Doppler Current Profilers: Principles of Operation: A Practical Primer*. RD Instruments, 1996.
- S.K. Kang, M.G.G. Foreman, W.R. Crawford, and J.Y. Cherniawsky. Numerical modeling of internal tide generation along the Hawaiian Ridge. *Journal of Physical Oceanography*, 30:1083–1098, 2000.
- P.K. Kundu. *Fluid Mechanics*. Academic Press, 1990.
- L.H. Larsen. Internal waves incident upon a knife edge barrier. *Deep-Sea Research 1*, 16: 411–419, 1968.
- R. Lhermitte. Doppler sonar observation of tidal flow. *Journal of Geophysical Research*, 88: 725–742, 1983.
- R. Lhermitte and R. Serafin. Pulse-to-pulse coherent doppler sonar signal processing techniques. *Journal of Atmospheric and Oceanic Technology*, 1:293–308, 1984.
- S.G. Llewellyn Smith and W.R. Young. Conversion of the barotropic tide. *Journal of Physical Oceanography*, 32:1554–1566, 2002.

- A. Lohrmann, B. Hackett, and L.P. Røed. High resolution measurements of turbulence, velocity and stress using a pulse-to-pulse coherent sonar. *Journal of Atmospheric and Oceanic Technology*, 7:19–37, 1990.
- Y. Lu and R.G. Lueck. Using a broadband ADCP in a tidal channel. part i: Mean flow and shear. *Journal of Atmospheric and Oceanic Technology*, 16:1556–1567, 1999a.
- Y. Lu and R.G. Lueck. Using a broadband ADCP in a tidal channel. part ii: Turbulence. *Journal of Atmospheric and Oceanic Technology*, 16:1568–1579, 1999b.
- Y. Lu, D.G. Wright, and D. Brickman. Internal tide generation over topography: Experiments with a free-surface z-level ocean model. *Journal of Atmospheric and Oceanic Technology*, 18(6):1076–1091, 2001.
- M.A. Merrifield, P.E. Holloway, and T.M.S. Johnston. The generation of internal tides at the Hawaiian Ridge. *Geophysical Review Letters*, 28(4):559–562, 2001.
- A.L. New. Internal tidal mixing in the Bay of Biscay. *Deep-Sea Research 1*, 35:691–709, 1988.
- M. W. Ott. *Mixing and Secondary Circulation in Juan de Fuca Strait*. PhD thesis, University of Victoria, 2000.
- M. W. Ott. An improvement in the calculation of ADCP velocities. *Journal of Atmospheric and Oceanic Technology*, 19:1738–1741, 2002.
- S.J. Prinsenbergh. *Internal wave generation from a step-like constant slope continental shelf*. PhD thesis, University of Washington, 1971.
- S.J. Prinsenbergh and M. Rattray. Effects of continental slope and variable Brunt-Väisälä frequency on the coastal generation of internal tides. *Deep-Sea Research 1*, 22:251–263, 1975.
- S.J. Prinsenbergh, W.L. Wilmot, and M. Rattray. Generation and dissipation of coastal internal tides. *Deep-Sea Research 1*, 21:263–281, 1974.
- M. Rattray. On the coastal generation of internal tides. *Tellus*, 12:54–62, 1960.
- M. Rattray, J.G. Dworski, and P.E. Kovala. Generation of long internal waves at the continental slope. *Deep-Sea Research 1*, 16:179–195, 1969.

- R.D. Ray and G.T. Mitchum. Surface manifestation of internal tides in the deep ocean: observations from altimetry and island gauges. *Progress in Oceanography*, 40:135–162, 1997.
- T.P. Rippeth, E. Williams, and J.H. Simpson. Reynolds stress and turbulent energy production in a tidal channel. *Journal of Physical Oceanography*, 32:1242–1251, 2002.
- R.M. Robinson. The effects of a vertical barrier on internal waves. *Deep-Sea Research 1*, 16:421–429, 1968.
- B. Sjöberg and A. Stigebrandt. Computations of the geographical distribution of the energy flux to mixing processes via internal tides and the associated vertical circulation in the ocean. *Deep-Sea Research 1*, 39(2):269–291, 1992.
- L. St. Laurent and C. Garrett. The role of internal tides in mixing the deep ocean. *Journal of Physical Oceanography*, 32:2882–2899, 2002.
- L. St. Laurent, S. Stringer, C. Garrett, and D. Perreault-Joncas. The generation of internal tides at abrupt topography. *Deep-Sea Research 1*, 50:987–1003, 2003.
- M.T. Stacey, S.G. Monismith, and J.R. Burau. Measurements of Reynolds stress profiles in unstratified tidal flow. *Journal of Geophysical Research*, 104:10933–10949, 1999a.
- M.T. Stacey, S.G. Monismith, and J.R. Burau. Observations of turbulence in a partially stratified estuary. *Journal of Physical Oceanography*, 29:1950–1970, 1999b.
- A. Stigebrandt. Some aspects of tidal interaction with fjord constrictions. *Estuarine and Coastal Marine Science*, 11:151–166, 1980.
- G.M. Torgrimson and B.M. Hickey. Barotropic and baroclinic tides over the continental slope and shelf off Oregon. *Journal of Physical Oceanography*, 9(5):945–961, 1979.
- H. van Haren, N. Oakey, and C. Garrett. Measurements of internal wave band eddy fluxes above a sloping bottom. *Journal of Marine Research*, 52:909–946, 1994.
- W.L. Wilmot. *Generation and dissipation of internal tides*. PhD thesis, University of Washington, 1972.

Appendix A

Coordinate Transformations

Each beam of an ADCP measures the velocity only in the direction in which the beam is pointing; trigonometric transformations must be applied to the beam velocities to derive useful quantities such as Cartesian velocities. When the vertical axis of the instrument is not aligned with the Cartesian vertical axis, further transformations must be made to resolve the components based on the tilt of the instruments. To resolve a set of beam velocities into their Cartesian components, one must start at the simplest configuration of zero tilt and apply the proper rotation matrices. These equations have been outlined in Lohrmann et al. (1990), but will be reviewed here.

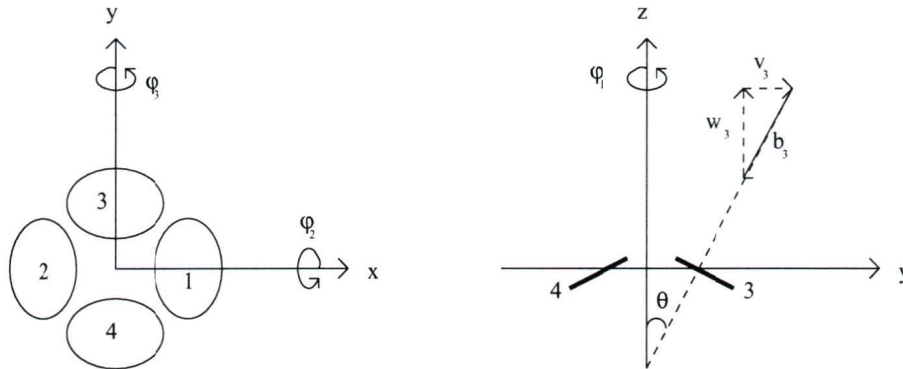


Figure A.1: Janus ADCP configuration (redrawn from Lu and Lueck (1999a))

The base vectors of the four beams of the Janus ADCP are functions of the beam angle θ only and are given as $[-\sin\theta \ 0 \ -\cos\theta]$, $[\sin\theta \ 0 \ -\cos\theta]$, $[0 \ -\sin\theta \ -\cos\theta]$, and $[0 \ \sin\theta \ 0 \ -\cos\theta]$, for beams 1 through 4, respectively, as can be seen by referring to Figure A.1. These vectors can be multiplied by the Cartesian component velocities u , v , and w to yield the basic beam velocities in an untilted reference frame. In the presence of tilt, however, these vectors must be rotated around two different axes in succession. The rotation matrix for a “pitch”, which is defined as a negative rotation around the x -axis and

is denoted by ϕ_2 , is

$$P = \begin{bmatrix} 1 & 0 & 0 \\ 0 & \cos \phi_2 & -\sin \phi_2 \\ 0 & \sin \phi_2 & \cos \phi_2 \end{bmatrix} \quad (\text{A.1})$$

while the rotation matrix for a “roll”, which is defined as a positive rotation around the y -axis and is denoted by ϕ_3 , is

$$R = \begin{bmatrix} \cos \phi_3 & 0 & \sin \phi_3 \\ 0 & 1 & 0 \\ -\sin \phi_3 & 0 & \cos \phi_3 \end{bmatrix} \quad (\text{A.2})$$

For the instruments presented here, the roll rotation is executed first and then the pitch rotation is applied so that the net rotation matrix is

$$T = P * R = \begin{bmatrix} \cos \phi_3 & 0 & \sin \phi_3 \\ \sin \phi_2 & \cos \phi_2 & -\sin \phi_2 \cos \phi_3 \\ -\cos \phi_2 \sin \phi_3 & \sin \phi_2 & \cos \phi_2 \cos \phi_3 \end{bmatrix} \quad (\text{A.3})$$

The net rotation matrix is applied to each of the four base vectors and then multiplied by the Cartesian component velocities to yield the beam velocity equations.

$$\begin{aligned}
b_1 &= \begin{bmatrix} \cos \phi_3 & 0 & \sin \phi_3 \\ \sin \phi_2 \sin \phi_3 & \cos \phi_2 & -\cos \phi_3 \sin \phi_2 \\ -\sin \phi_3 \cos \phi_2 & \sin \phi_2 & \cos \phi_3 \cos \phi_2 \end{bmatrix} \begin{bmatrix} -\sin \theta \\ 0 \\ -\cos \theta \end{bmatrix} \begin{bmatrix} u_1 & v_1 & w_1 \end{bmatrix} \\
&= -u_1 \sin(\theta + \phi_3) + v_1 \sin \phi_2 \cos(\theta + \phi_3) - w_1 \cos \phi_2 \cos(\theta + \phi_3) \tag{A.4}
\end{aligned}$$

$$\begin{aligned}
b_2 &= \begin{bmatrix} \cos \phi_3 & 0 & \sin \phi_3 \\ \sin \phi_2 \sin \phi_3 & \cos \phi_2 & -\cos \phi_3 \sin \phi_2 \\ -\sin \phi_3 \cos \phi_2 & \sin \phi_2 & \cos \phi_3 \cos \phi_2 \end{bmatrix} \begin{bmatrix} \sin \theta \\ 0 \\ -\cos \theta \end{bmatrix} \begin{bmatrix} u_2 & v_2 & w_2 \end{bmatrix} \\
&= u_2 \sin(\theta - \phi_3) + v_2 \sin \phi_2 \cos(\theta - \phi_3) - w_2 \cos \phi_2 \cos(\theta - \phi_3) \tag{A.5}
\end{aligned}$$

$$\begin{aligned}
b_3 &= \begin{bmatrix} \cos \phi_3 & 0 & \sin \phi_3 \\ \sin \phi_2 \sin \phi_3 & \cos \phi_2 & -\cos \phi_3 \sin \phi_2 \\ -\sin \phi_3 \cos \phi_2 & \sin \phi_2 & \cos \phi_3 \cos \phi_2 \end{bmatrix} \begin{bmatrix} 0 \\ -\sin \theta \\ -\cos \theta \end{bmatrix} \begin{bmatrix} u_3 & v_3 & w_3 \end{bmatrix} \\
&= -u_3 \sin \phi_3 \cos \theta - v_3 (\cos \phi_2 \sin \theta - \sin \phi_2 \cos \phi_3 \cos \theta) \\
&\quad -w_3 (\cos \phi_2 \cos \phi_3 \cos \theta + \sin \phi_2 \sin \theta) \tag{A.6}
\end{aligned}$$

$$\begin{aligned}
b_4 &= \begin{bmatrix} \cos \phi_3 & 0 & \sin \phi_3 \\ \sin \phi_2 \sin \phi_3 & \cos \phi_2 & -\cos \phi_3 \sin \phi_2 \\ -\sin \phi_3 \cos \phi_2 & \sin \phi_2 & \cos \phi_3 \cos \phi_2 \end{bmatrix} \begin{bmatrix} 0 \\ \sin \theta \\ -\cos \theta \end{bmatrix} \begin{bmatrix} u_4 & v_4 & w_4 \end{bmatrix} \\
&= -u_4 \sin \phi_3 \cos \theta + v_4 (\cos \phi_2 \sin \theta + \sin \phi_2 \cos \phi_3 \cos \theta) \\
&\quad -w_4 (\cos \phi_2 \cos \phi_3 \cos \theta - \sin \phi_2 \sin \theta) \tag{A.7}
\end{aligned}$$

The same transformation is applied to the four beam Cyclops ADCP. The base vectors for the Cyclops are $\begin{bmatrix} 0 & 0 & -1 \end{bmatrix}$, $\begin{bmatrix} 0 & \sin \theta & -\cos \theta \end{bmatrix}$, $\begin{bmatrix} \sin \theta \sin \frac{\pi}{3} & -\sin \theta \cos \frac{\pi}{3} & -\cos \theta \end{bmatrix}$, and $\begin{bmatrix} -\sin \theta \sin \frac{\pi}{3} & -\sin \theta \cos \frac{\pi}{3} & -\cos \theta \end{bmatrix}$ for beams 1 through 4, respectively, as can be seen by referring to Figure A.2.

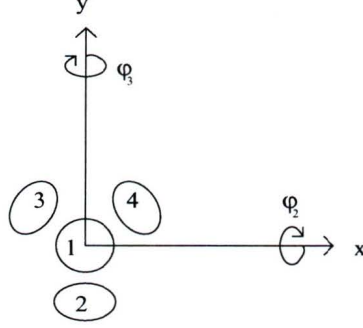


Figure A.2: Cyclops ADCP configuration

$$\begin{aligned}
 b_1 &= \begin{bmatrix} \cos \phi_3 & 0 & \sin \phi_3 \\ \sin \phi_2 \sin \phi_3 & \cos \phi_2 & -\cos \phi_3 \sin \phi_2 \\ -\sin \phi_3 \cos \phi_2 & \sin \phi_2 & \cos \phi_3 \cos \phi_2 \end{bmatrix} \begin{bmatrix} 0 \\ 0 \\ -1 \end{bmatrix} \begin{bmatrix} u_1 & v_1 & w_1 \end{bmatrix} \\
 &= -u_1 \sin \phi_3 + v_1 \sin \phi_2 \cos \phi_3 - w_1 \cos \phi_2 \cos \phi_3
 \end{aligned} \tag{A.8}$$

$$\begin{aligned}
 b_2 &= \begin{bmatrix} \cos \phi_3 & 0 & \sin \phi_3 \\ \sin \phi_2 \sin \phi_3 & \cos \phi_2 & -\cos \phi_3 \sin \phi_2 \\ -\sin \phi_3 \cos \phi_2 & \sin \phi_2 & \cos \phi_3 \cos \phi_2 \end{bmatrix} \begin{bmatrix} 0 \\ \sin \theta \\ -\cos \theta \end{bmatrix} \begin{bmatrix} u_2 & v_2 & w_2 \end{bmatrix} \\
 &= -u_2 \sin \phi_3 \cos \theta + v_2 (\cos \phi_2 \sin \theta + \sin \phi_2 \cos \phi_3 \cos \theta) \\
 &\quad -w_2 (\cos \phi_2 \cos \phi_3 \cos \theta - \sin \phi_2 \sin \theta)
 \end{aligned} \tag{A.9}$$

$$\begin{aligned}
 b_3 &= \begin{bmatrix} \cos \phi_3 & 0 & \sin \phi_3 \\ \sin \phi_2 \sin \phi_3 & \cos \phi_2 & -\cos \phi_3 \sin \phi_2 \\ -\sin \phi_3 \cos \phi_2 & \sin \phi_2 & \cos \phi_3 \cos \phi_2 \end{bmatrix} \begin{bmatrix} \sin \theta \sin \frac{\pi}{3} \\ -\sin \theta \cos \frac{\pi}{3} \\ -\cos \theta \end{bmatrix} \begin{bmatrix} u_3 & v_3 & w_3 \end{bmatrix} \\
 &= u_3 \left(\cos \phi_3 \sin \theta \sin \frac{\pi}{3} - \sin \phi_3 \cos \theta \right) \\
 &\quad -v_3 \left[\left(\cos \phi_2 \cos \frac{\pi}{3} - \sin \phi_2 \sin \phi_3 \sin \frac{\pi}{3} \right) \sin \theta - \sin \phi_2 \cos \phi_3 \cos \theta \right] \\
 &\quad -w_3 \left[\left(\sin \phi_2 \cos \frac{\pi}{3} + \cos \phi_2 \sin \phi_3 \sin \frac{\pi}{3} \right) \sin \theta + \cos \phi_2 \cos \phi_3 \cos \theta \right]
 \end{aligned} \tag{A.10}$$

$$\begin{aligned}
 b_4 &= \begin{bmatrix} \cos \phi_3 & 0 & \sin \phi_3 \\ \sin \phi_2 \sin \phi_3 & \cos \phi_2 & -\cos \phi_3 \sin \phi_2 \\ -\sin \phi_3 \cos \phi_2 & \sin \phi_2 & \cos \phi_3 \cos \phi_2 \end{bmatrix} \begin{bmatrix} -\sin \theta \sin \frac{\pi}{3} \\ -\sin \theta \cos \frac{\pi}{3} \\ -\cos \theta \end{bmatrix} \begin{bmatrix} u_4 & v_4 & w_4 \end{bmatrix} \\
 &= -u_4 \left(\cos \phi_3 \sin \theta \sin \frac{\pi}{3} + \sin \phi_3 \cos \theta \right) \\
 &\quad -v_4 \left[\left(\cos \phi_2 \cos \frac{\pi}{3} + \sin \phi_2 \sin \phi_3 \sin \frac{\pi}{3} \right) \sin \theta - \sin \phi_2 \cos \phi_3 \cos \theta \right] \\
 &\quad -w_4 \left[\left(\sin \phi_2 \cos \frac{\pi}{3} - \cos \phi_2 \sin \phi_3 \sin \frac{\pi}{3} \right) \sin \theta + \cos \phi_2 \cos \phi_3 \cos \theta \right]
 \end{aligned} \tag{A.11}$$

To extract Cartesian velocities from these beam velocities requires spatial homogeneity of the flow over the beam field (ie. $u_1 = u_2 = u_3 = u_4 = u$ and similarly for v and w). This may be an unrealistic assumption in turbulent environments, so a slightly less restrictive requirement is imposed on the second moments, or the variances. If spatial homogeneity cannot be established, then “statistical” homogeneity requires that the variance of each velocity component is the same across the beam field (ie $\overline{u_1'^2} = \overline{u_2'^2} = \dots = \overline{u'^2}$). The assumption of statistical homogeneity is central to the variance technique.

VITA

Surname: **Stringer**

Given Names: **Steven Ross**

Place of Birth: St. John's, NL, Canada

Educational Institutions Attended:

University of Victoria	1999 to 2003
Memorial University of Newfoundland	1994 to 1999

Degrees Awarded:

B.Sc. (hons)	Memorial University of Newfoundland	1999
--------------	-------------------------------------	------

Honours and Awards:

NSERC PGS-A Award	1999 to 2001
CMOS Weather Research House Scholarship Supplement	1999 to 2001

Publications:

St. Laurent, L., S. Stringer, C. Garrett, and D. Perreault-Joncas,
The Generation of Internal Tides at Abrupt Topography
Deep Sea Research Part 1, Volume 50, pages 987-1003, 2003

University of Victoria

Partial Copyright License

I hereby grant the right to lend my dissertation to users of the University of Victoria Library, and to make single copies only for such users or in response to a request from the Library of any other university, or similar institution, on its behalf or for one of its users. I further agree that permission for extensive copying of this dissertation for scholarly purposes may be granted by me or a member of the University designated by me. It is understood that copying or publication of this dissertation for financial gain shall not be allowed without my written permission.

Title of Dissertation: REYNOLDS STRESSES FROM ADCPs AND MODELLING OF
INTERNAL TIDES.

Author:



Steven Stringer

2003 August 4